

Doctoral Thesis in Physics

Perpendicular magnetic tunnel
junctions based on CoFeB and
MnIr/CoFe with exchange bias

Spintronics

Orestis Manos

Bielefeld University
Department of Physics

Declaration

I wrote this thesis by myself and used none but the indicated resources. Text and figures were partly taken from corresponding publications, which originate directly from this work.

(Orestis Manos)

Reviewers:

Prof. Dr. Günter Reiss

Prof. Dr. Thomas Huser

Copyright ©

BIELEFELD UNIVERSITY, DEPARTMENT OF PHYSICS
CENTER FOR SPINELECTRONIC MATERIALS & DEVICES

Doctoral thesis

May 3, 2019

Printed on permanent paper °° ISO 9706

“It is the mark of an educated mind to entertain a thought without accepting it”

Aristotle (384–322 B.C.)

Contents

1	Introduction	9
2	Fundamentals	13
2.1	Spintronics	13
2.1.1	GMR effect	13
2.1.2	TMR effect	14
2.2	Physical mechanisms of TMR effect	15
2.2.1	Jullière’s Model	15
2.2.2	The Slonczewski model	17
2.2.3	Incoherent and coherent tunneling	18
2.2.4	Coherent tunneling: Prominent features and consequences	19
2.3	Origin of magnetic anisotropy in thin films	20
2.3.1	Surface and volume contributions	21
2.3.2	Direct and indirect contributions on the formation of PMA in underlayer/CoFeB/MgO systems	23
2.4	Exchange bias	24
2.4.1	Macroscopic models	25
2.4.2	Mesosopic models	30
2.4.3	Microscopic models	31
2.5	Perpendicular EB in MnIr/CoFeB/MgO systems	32
2.6	Magnetostatic coupling effects in FM/NM/FM systems	34
2.6.1	IEC: Slonczewski and Bruno models	34
2.6.2	Orange peel coupling in systems with PMA	35

2.6.3	Methodology for the determination of magnetostatic coupling	37
2.7	Magnetic memories and sensors	38
2.7.1	Field-driven MRAM	38
2.7.2	Spin-Transfer Torque Magnetic Random Access Memory (STT-MRAM)	40
2.7.3	Magnetic sensors	42
2.8	p-MTJs vs. i-MTJs for MRAM applications	43
3	Sample preparation	47
3.1	Thin film fabrication	47
3.2	p-MTJ preparation via e-beam lithography	48
3.3	Structural analysis	49
3.3.1	X-ray diffraction	50
3.3.2	X-ray reflectivity	51
3.4	Magnetic analysis	53
3.4.1	Alternating Gradient Magnetometer	53
3.4.2	Magneto-optic Kerr Effect	54
3.5	Chemical analysis	56
4	Experimental	59
4.1	Pinned electrode stacks based on MnIr/CoFe bilayers	60
4.2	Soft electrode stacks based on CoFeB	64
4.2.1	Ta-capped soft electrode	64
4.2.2	Alternative capping layers for the soft electrode	68
4.3	Ta-capped p-MTJs with exchange bias	72
4.3.1	Magnetic properties	72
4.3.2	TMR properties	81
4.4	Zr- and Hf-capped p-MTJs with exchange bias	83
4.4.1	Magnetic properties	83
4.4.2	TMR properties	85
4.5	Auger measurements	88
4.6	Voltage Control Magnetic Anisotropy measurements	90
5	Summary & Outlook	93
6	Publications	113

Introduction

The Information Age brought about many new inventions and innovations. Our environment is increasingly wired, sensor-filled, and digitally connected. It is a wide consensus that the corner stone of information age is the invention of Internet. As a result, enormous amounts of data have been generated in the first decade of 21st century, which may exceed the amount generated in the whole 20th century. The field of data storage technology is confronted with the challenge to manage the continuously growing unbounded volume of data. Towards this approach, volatile and non-volatile memories are valued for their significant contribution in the field.

Volatile memories (e.g. dynamic random access memory (DRAM), static random access memory (SRAM)) require constant power to maintain the stored information. Whereas, the non-volatile ones retain the stored information even after the power is turned off. There are several types of non-volatile memories which can be categorized according to their writing mechanism. A type of non-volatile memory which has attracted considerable scientific interest is the magnetoresistive random access memory (MRAM) [1, 2], which takes an advantage of the tunnel magnetoresistance (TMR) effect [3]. The core element of an MRAM cell is the so called magnetic tunnel junction (MTJ) which is composed of a thin insulating barrier film sandwiched by two ferromagnetic (F) ones. MTJs with a fully epitaxial (001) MgO barrier sandwiched by (001) bcc F electrodes, such as Fe, Co, and CoFe, were first theoretically predicted to show high TMR ratio of several 100 %, as a consequence of the

coherent tunneling of Δ_1 electrons [4–6]. The experimentally discovered large TMR amplitude of in-plane magnetized MTJs with a crystalline MgO barrier rendered a major breakthrough for these materials [7, 8]. It is worth mentioning that the theoretical foundation and route to develop MRAM was established in 1988 by Fert and Grünberg with the groundbreaking discovery of giant magnetoresistance (GMR) effect [9, 10].

Nevertheless, for memory applications, the interest rapidly changed towards out-of-plane (OOP) magnetized systems. MTJs with perpendicular magnetic anisotropy (PMA) have several advantages as compared with their in-plane (IP) counterparts. Firstly, an increasing density of memory cells on a wafer can be realized since no elliptical shape is required to stabilize the anisotropy direction [11]. Furthermore, the PMA energy is usually much larger than the energy related with the shape anisotropy that can be obtained in planar MTJs, allowing long memory retention at small size [12]. Additionally, for a given retention time, the critical current density to write information by spin transfer torque (STT) switching is strongly reduced, provided that the Gilbert damping remains low enough [13].

However, neighboring MTJs in a memory array as well as the reference layer of the STT-switched MTJ will be magnetically disturbed. This is of major importance since even after a large number of STT switching events the magnetic states of the MTJs do not “creep” either to some intermediate state or completely reverse. One distinct advantage of MTJs with exchange bias (EB) layers is the robustness of the reference magnetization against such perturbation [14].

Another widespread commercial use of MTJs is also found in sensor technology. The areas of magnetic field sensor application are virtually unlimited, starting from automotive industry (e.g. CT219 and RR111 proposed by CROCUS technology and RedRock) until biomedical technology [15]. A wide array of magnetic sensors exploit different magnetoresistive effects (e.g. anisotropic magnetoresistance, GMR, and TMR). Nowadays, the most highly-sensitive magnetic sensors are composed of TMR elements in which a considerably large output can be obtained. In the ideal TMR sensor, a hysteresis free electrode (sensing electrode) with linear response to the applied magnetic field is combined with a pinned one which is usually accomplished through the EB effect. To achieve this behaviour, the sensing and pinned electrode magnetizations are set orthogonal to each other and the external magnetic

field is applied perpendicular to the sensing layer but parallel to the reference one [16]. Unlikely, such designs necessitate the use of complicated sensor design, suffer from magnetization fluctuation and magnetic noise when reducing the sensor size [17]. Towards tackling this issue the use of sensing electrodes presenting strong PMA [18, 19] or superparamagnetism [20] could be an alternative solution and pave the way for the development of nano-scale magnetic sensors with simple design, high sensitivity, and low power consumption.

The plethora of spintronic applications based on MTJs underscore their fundamental importance of the investigation. This work offers a valuable insight about the realization of p-MTJs with EB by using a natural antiferromagnet (AFM), i.e., MnIr in the pinned electrode and different capping layers (i.e Ta, Hf, Zr) in the soft one. We investigate the correlation of several magnetic properties with the TMR ratio and we provide information about the adjustment of the TMR ratio via alternating the magnetic properties. Furthermore, we study the impact on the TMR ratio from the placement on the soft electrode of several capping layers with different degree of boron (B) absorption material.

The herein thesis is organized as follows: Chapter 2 contains the fundamentals of spintronics, the underlying effects, and the functional principles of spintronic devices. A number of the physical models which govern the TMR processes in MTJs with crystalline (e.g. MgO) and amorphous (e.g. AlO_x) barriers are presented first. In turn, the origin of magnetic anisotropy in thin films is discussed, along with the physical mechanisms which give rise to the establishment of PMA in trilayer systems where a ferromagnet (FM) is sandwiched by an underlayer material and an MgO barrier. Additionally, the EB models categorized into macroscopic, mesoscopic, and microscopic are analyzed. Simultaneously, the mechanisms which occur in MnIr/CoFeB/MgO systems responsible for the establishment of perpendicular EB are presented. Moreover, the magnetostatic coupling effects which take place in FM/NM/FM systems are in detail discussed (where NM is a non magnetic spacer). We perform a thorough analysis about the models which govern the magnetostatic coupling in FM/NM/FM systems and we present a methodology for its determination. Also, two categories of MRAM are analyzed together with their principle of operation. The advantageous use of the p-MTJs compared

to the MTJs with in-plane orientation for MRAM applications is highlighted in the last section of Chap. 2.

Chapter 3 includes all of the experimental methods and their underlying physics used to fabricate and analyze the thin film samples and devices. Chapter 4 presents the experimental results for the pinned/soft electrodes, as well as, the full p-MTJ stacks. First, we provide a detailed analysis of the magnetic properties of the pinned (e.g., MnIr/CoFe-based stacks) and soft electrodes (MgO/CoFeB/A where A=Ta, Hf, Zr, Mo) which compose the investigated full p-MTJs. In the pinned electrode, we point out the tunable character of several magnetic properties via modifying the thickness of certain layers. Via this procedure, we extract the films with the most suitable characteristics, from the magnetic standpoint, for the fabrication of the pinned part of the full p-MTJs. For the soft electrode, we perform an extended study of a number of parameters which possess a decisive role in the establishment of PMA in a series of trilayer systems. Simultaneously, we elucidate the role of the diffusion mechanisms in the individual systems for the realization of strong PMA. After the examination of the pinned and soft electrodes, we analyze the magnetic properties of the p-MTJ stacks capped with Ta in the soft electrode, and we reveal the correlation of them with the TMR ratio. Furthermore, we examine the influence of the magnetic properties and the TMR ratio of the p-MTJs by changing the capping layer material (e.g. Hf, Zr). The use of a series of capping layers with different degree of B absorption unveils the significant importance of the presence of B in the FM/NM interfaces of such stacks towards the achievement of p-MTJs, acquiring high TMR ratios and desired magnetic characteristics (e.g. strong PMA). In the last two sections, we present the voltage-controlled magnetic anisotropy and the Auger measurements, which were implemented on p-MTJ stacks capped with Ta and Hf.

Most of the presented results here have already been published in peer reviewed journals. The corresponding articles are referenced in the respective chapters.

Fundamentals

2.1 Spintronics

2.1.1 GMR effect

Spintronics is a merger of magnetism and electronics. The groundbreaking discovery of the GMR effect has been a landmark in the history of the spintronics field. In 1988, Albert Fert and Peter Grünberg introduced independently the GMR effect [9, 10], reporting the observation of spin-dependent transport phenomena in superstructures consisting of magnetic and nonmagnetic layers. GMR can be considered as the backbone of spintronics bringing the “spin-dependent transport” which is a new physical approach compared to the magnetoresistance known before. Specifically, the spin valve is the core GMR device consisting of two F layers separated by a NM metal spacer. In this structure, one F layer behaves as a “hard” layer presenting robustness in changing its magnetic state and the other one acts as a “soft” layer, susceptible to change its magnetic state easily. When the magnetization vectors of the two F layers are parallel, the electrons with spins parallel to the magnetizations are less probable to be scattered leading to a low electric resistance state. Conversely, when the magnetization vectors are antiparallel, both spin-types should pass through the layers but considerably scattered, which leads to a high electric resistance state. GMR has been primarily utilized as spin-valve magnetoresistive heads in magnetic hard disk drives between 1998 and 2004,

contributing to the increase in the density of the magnetic storage capacity. In turn, it was replaced by TMR heads which present larger magnetoresistance amplitude. GMR sensors are being used in the automotive industry, robotics, and biotechnological applications. Furthermore, GMR-based memories are being used mainly for space applications because of their radiation hardness [21].

2.1.2 TMR effect

After this undeniable breakthrough in spintronics, Miyazaki *et al.* [22] and Moodera *et al.* [23] discovered the TMR effect at room temperature (RT), providing an opportunity for the evolution of nonvolatile solid-state memory devices, MRAM, and fast programmable logic circuits. The fundamental structure in which the TMR effect takes place is a MTJ and from the magnetic respect is similar to the spin valve with the major difference that the NM spacer consists of a very thin insulating layer, e.g., MgO or Al₂O₃. The tunneling probability of electrons depends on the relative orientation of the magnetization vectors of the two F electrodes. Particularly, when the magnetization vectors are aligned in parallel the tunneling probability is high, whereas, the tunneling probability is low in the antiparallel orientation of the magnetization vectors. Then the TMR ratio is given by the formula, $TMR = \frac{R_{AP} - R_P}{R_P}$, where $R_{AP(P)}$ is the resistance in the antiparallel (parallel) state and quantifies the efficiency of the TMR effect .

Although nowadays the astonishing TMR ratios have been reported in literature, the research for TMR holds already from 1975. That year, Jullière *et al.* [3] reported a TMR ratio equal to 14% at 4.2K in a MTJ consisting of Fe/GeO/Co. Moreover, in 1995 Miyazaki *et al.* [22] and Moodera *et al.* [23] independently reported TMR ratios larger than 10% at RT in Fe/Al₂O₃/Fe and FeCo/Al₂O₃/Co MTJs, respectively. Up to now, TMR ratios of about 600% at RT [24] and 1995% at 4.2K [25] have been reported for IP magnetized MTJs. In addition, TMR ratios ranging from (120-250)% have been realized for p-MTJs consisting of CoFeB/MgO/CoFeB electrodes [26–28].

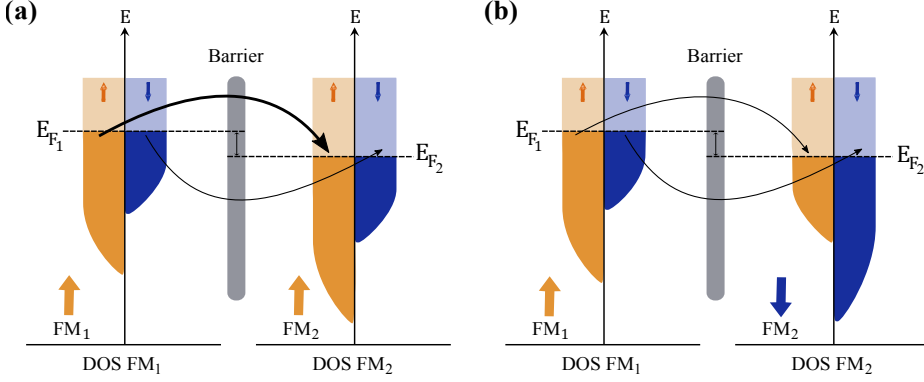


Figure 2.1. Qualitative draw of the spin-dependent tunneling process through an insulating barrier when the magnetizations of F electrodes acquire (a) parallel or (b) antiparallel relative orientation.

2.2 Physical mechanisms of TMR effect

2.2.1 Jullière's Model

The earliest attempt in 1975 for explaining the physical mechanisms which occur in TMR devices was performed by Jullière [3]. According to the proposed model, the origin of the high and low resistance state is a direct outcome of the relative orientation of the spin states of the individual F electrodes.

Assuming the absence of coupling between these two spin states, we can treat them as channels that conduct independently. This approach concerns the “two current” model. In the F transition metals and alloys case, each spin channel can be considered separately within transport theory and the total spin current is the sum of the individual ones. The tunneling current is predominantly carried by the electrons whose states are near the Fermi energy. The transmission probability ($T_{\uparrow(\downarrow)}$) for the majority (\uparrow) and minority (\downarrow) carriers of each channel, is proportional to the product of the density of states (DOS) of the two electrodes ($D_1(E_{F_1})_{\uparrow(\downarrow)}$, $D_2(E_{F_2})_{\uparrow(\downarrow)}$) at their respective Fermi levels following the equation

$$T_{\uparrow(\downarrow)} \propto D_1(E_{F_1})_{\uparrow(\downarrow)} D_2(E_{F_2})_{\uparrow(\downarrow)}. \quad (2.1)$$

In the parallel state (PAR), the majority (spin up) electrons tunnel to the majority (spin up) unoccupied states and the minority (spin down) ones to the corresponding minority (spin down) unoccupied states, as depicted in Fig. 2.1(a). Thus, a large spin polarized tunneling current is present, if a bias voltage is applied to the MTJ. Following the two current model, the tunneling probability can be expressed by

$$T_{\text{PAR}} \propto D_{1\uparrow}D_{2\uparrow} + D_{1\downarrow}D_{2\downarrow}. \quad (2.2)$$

On the contrary, in the antiparallel state (AP) the majority (spin up) electrons tunnel to the minority (spin up) unoccupied states, while the minority (spin down) electrons tunnel to the majority (spin down) unoccupied states, as shown in Fig. 2.1(b). Therefore, a small number of spin up (spin down) electrons can tunnel, which leads to a small tunneling current. In this case, the transmission probability is described by the formula

$$T_{\text{AP}} \propto D_{1\uparrow}D_{2\downarrow} + D_{1\downarrow}D_{2\uparrow}. \quad (2.3)$$

Using the definitions for TMR, spin polarization (P) of a FM, and the general relation which connects the conductance G with the tunneling probability

$$\text{TMR} = \frac{G_{\text{PAR}} - G_{\text{AP}}}{G_{\text{AP}}}, \quad (2.4)$$

$$P_{1(2)} = \frac{D_{1(2)\uparrow} - D_{1(2)\downarrow}}{D_{1(2)\uparrow} + D_{1(2)\downarrow}}, \quad (2.5)$$

$$G \propto e^{-A\phi^{1/2}} T, \quad (2.6)$$

where G_{PAR} (G_{AP}) is the conductance in the PAR (AP) state, we derive the relation

$$\text{TMR} = \frac{2P_1P_2}{1 - P_1P_2} \quad (2.7)$$

which connects the TMR ratio with the relative spin polarizations of the individual F electrodes. It is worth noting that in this model all the band structure effects in the magnetic electrodes and in the barrier are neglected. However, this model predicts successfully the amplitude of TMR in amorphous aluminum-oxide (AlO_x)-based MTJs.

In the case of MTJs based on epitaxial barriers, notably of MgO, the model fails to successfully predict the amplitude of TMR. The erroneous way of the estimation of the actual amplitude of P of a certain F material and the different nature of tunneling compared to the AlO_x -based MTJs, which will be briefly analyzed in the next paragraphs, are two of the basic reasons for this failure.

2.2.2 The Slonczewski model

In 1989, Slonczewski [29] performed analytical calculations of the electron wave functions across the barrier, after matching appropriate boundary conditions at the FM/NM interfaces of a FM/NM/FM trilayer system and extended Jullière's model. In this approach the $T_{\uparrow(\downarrow)}$ is not only determined by the $D_1(E_{F_1})_{\uparrow(\downarrow)}$, $D_2(E_{F_2})_{\uparrow(\downarrow)}$ as previously discussed, but also by their wave vector at the Fermi level k_F . The additional dependence of $T_{\uparrow(\downarrow)}$ on k_F can provide an initial simple basis to understand the large TMR ratio in MgO-based MTJs. In this model the G and TMR ratio are given by the formulas

$$G = G_0[1 + P_1^{\text{eff}}P_2^{\text{eff}}\cos\theta], \quad (2.8)$$

$$\text{TMR} = \frac{2P_1^{\text{eff}}P_2^{\text{eff}}}{1 - P_1^{\text{eff}}P_2^{\text{eff}}}, \quad (2.9)$$

where θ and $P_{1(2)}^{\text{eff}}$ stand for the relative angle between the two magnetization vectors and the effective spin-polarization of the electrodes, respectively. In addition, $P_{1(2)}^{\text{eff}}$ is connected with the decay coefficient (k) inside the barrier and the wave vectors $k_{F,\uparrow}$ and $k_{F,\downarrow}$ for majority and minority electrons at the Fermi level (E_F), through the relation

$$P_{1(2)}^{\text{eff}} = P_{1(2)} \frac{k^2 - k_{F,\uparrow}k_{F,\downarrow}}{k^2 + k_{F,\uparrow}k_{F,\downarrow}}. \quad (2.10)$$

It's worth mentioning that $k_{F,\uparrow} = k_{F,\uparrow}^{1(2)}$ and $k_{F,\downarrow} = k_{F,\downarrow}^{1(2)}$, since the two F electrodes are assumed to be identical [29]. From Eq. (2.10) considering the limit of large barrier thickness which results in large k , $P_{1(2)}^{\text{eff}}$ becomes equal to $P_{1(2)}$, as it was predicted by Jullière model. Consequently, Slonczewski's model through the factor $\frac{k^2 - k_{F,\uparrow}k_{F,\downarrow}}{k^2 + k_{F,\uparrow}k_{F,\downarrow}}$ introduces the role of the band structure

effects in the effective polarization of the electrodes and, thus, the measured TMR.

2.2.3 Incoherent and coherent tunneling

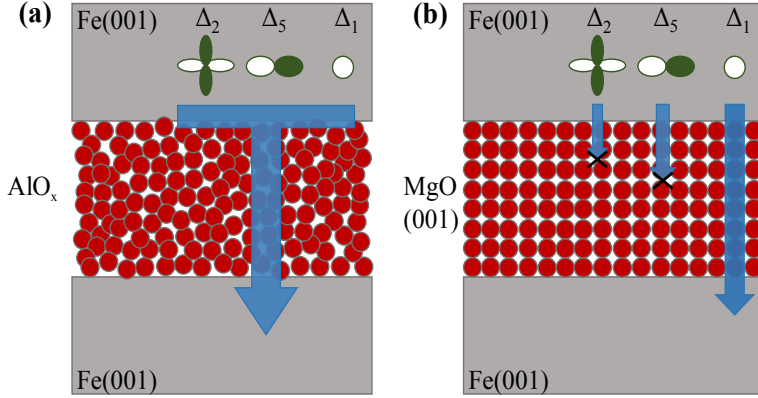


Figure 2.2. Incoherent and coherent tunneling through (a) an amorphous AlO_x barrier and (b) a crystalline MgO barrier.

In crystalline materials the electrons' wave function are described by Bloch states. Assuming for simplicity a perfect and infinite atomic crystal represented by a periodic potential, the Bloch states are wave function solutions of the Schrödinger equation. In particular, in crystalline F materials, e.g., Fe, Co, Ni as well as their corresponding alloys, the Bloch states obey certain symmetries such as Δ_1 , Δ_2 , and Δ_5 .

The Bloch states following the Δ_1 symmetry are spd hybridized states, filled only by majority electrons and usually have a large positive spin polarization at E_F . Whereas, the Bloch states with Δ_2 and Δ_5 symmetries regard d hybridized states, having smaller polarization compared to the Δ_1 states and being filled with majority and minority electrons.

In AlO_x -based MTJs, the electron wave functions of the F electrodes couple to any tunneling or evanescent states in the barrier, independent on their symmetry. The reason which dictates that physical mechanism is the amorphous structure of the barrier. As a result, the initial Bloch states, regardless of their symmetry, will equally decay. This tunneling process can be regarded as an incoherent tunneling as shown in Fig. 2.2(a). According to Jullière's model,

the tunneling probabilities for all Bloch states are equal. The consequence of this assumption is that the momentum and coherency of Bloch states are not conserved during tunneling.

Nevertheless, this statement is not even valid in AlO_x -based MTJs. It suffices to note that although the predicted P for Co and Ni is negative, the experimentally observed P is positive when combined with AlO_x barrier [30, 31]. The discrepancy between theory and the experimental results indicates that the tunneling probability in actual MTJs depends on the symmetry of Bloch states.

The essential difference between the MTJs with crystalline F electrodes based on amorphous, e.g., AlO_x , and crystalline, e.g., MgO, barriers is that in the latter case the symmetries of the tunneling wave functions are conserved. In this case, the tunneling process is defined as coherent as depicted in Fig. 2.2(b). As an outcome, the symmetries can play a role of “selective” spin polarized tunneling channels, promoting a high (low) tunneling probability for the carriers with positive (negative) P , resulting in large TMR ratio.

2.2.4 Coherent tunneling: Prominent features and consequences

In Subsec. 2.2.3 we introduced the two types of incoherent and coherent tunneling and highlighted their basic difference. In this subsection, we will present the prominent features of coherent tunneling, such as the conservation of symmetry and the selective decay of Bloch states inside the MgO barrier, along with the spin-filtering effects leading to high TMR ratios. In turn, we will emphasize on a number of experimental consequences which are directly related to the aforementioned features.

Let us assume a crystalline MTJ composed of $\text{Fe}(001)/\text{MgO}(001)/\text{Fe}(001)$ in which an ideal coherent tunneling occurs. According to theory, there are 4 Bloch states: Δ_1 , Δ_2 , Δ'_2 , Δ_5 arising from the crystalline body-centered-cubic (bcc) (001) symmetry, as a result of the linear combination of the atomic orbitals s, p, d. In the MgO, for $k_{\parallel} = 0$ there are three following evanescent states: Δ_1 , Δ_2 , and Δ_5 . As a corollary of coherent tunneling, the conservation of the symmetry of Bloch states takes place leading to the coupling of the $\text{Fe}-\Delta_{1(2')(5)}$ Bloch with the $\text{MgO}-\Delta_{1(2')(5)}$ evanescent states.

Additionally, a selective decay of the previously mentioned three evanescent states occurs in the MgO barrier [4]. It is demonstrated that among the three

evanescent states in MgO the Δ_1 has the slowest decay. As a result, the MgO barrier acts like a spin-filter on the wave functions which follow certain symmetry, allowing to Δ_1 states to mainly survive after entering the MgO barrier.

In the parallel alignment of the electrodes, the Δ_1 Bloch states correspond to majority electrons, whereas, for the antiparallel alignment there are no minority electrons with Δ_1 symmetry and the conduction is dominated by Δ_5 . Consequently, the tunneling conductance in the parallel state is considerably larger than in the antiparallel one resulting in large TMR ratios.

The experimental consequences of the close relation between the DOS near E_F with the TMR ratio, can be revealed from the estimation of TMR ratio in pure and contaminated with impurities MTJs at the FM/MgO interfaces. In the work of Zhang *et al.* [32], the impacts of the presence of oxygen (O) on the TMR ratio are examined in Fe/FeO/MgO/Fe MTJs.

Employing first-principles calculations of the electronic structure and tunneling magnetoconductance of Fe/FeO/MgO/Fe and Fe/MgO/Fe MTJs, it was found that an atomic layer of iron-oxide at the Fe/MgO interface substantially reduces the TMR ratio. The introduction of the O atom to the top Fe layer strongly reduces the DOS in the interlayer region between Fe and MgO. As a result, the reduction of coupling of Δ_1 state to the MgO reduces the tunneling current of the majority spin channel and inescapably the TMR ratio drops.

In a similar way, Burton *et al.* [33] theoretically predicted that the presence of B at the interfaces of CoFeB/MgO/CoFeB MTJs is detrimental to the TMR ratio. The significant suppression of the majority spin channel of conductance through the states with Δ_1 symmetry is the reason for this considerable decrease. Based on the aforementioned theoretical prediction, one part of this thesis investigates the impacts on the TMR ratio of the introduction of strong B absorber materials as capping layers in CoFeB-based p-MTJs. The results and the drawn conclusions are briefly presented in the experimental part.

2.3 Origin of magnetic anisotropy in thin films

In the following section we will analyze the origin of magnetic anisotropy in magnetic metal/oxide bilayers. The etymology of the word anisotropy

comes from the ancient Greek words *anisos* “unequal” and *tropos* “turn”. Therefore, anisotropy defines preferential (easy), intermediate and hard directions of a physical property. As a result, magnetic anisotropy is defined as the dependence of the ground energy state of a FM on the magnetization’s direction.

In the case of low-dimensional systems, e.g., magnetic thin films or multilayered systems, the presence of symmetry breaking elements such as surfaces and interfaces can have a major impact in the determination of magnetic anisotropy. Specifically, the variation of the thickness and the choice of the appropriate elements give rise to the manipulation of magnetic anisotropy. One of the most important consequences of the aforementioned manipulation is the observation of PMA. In particular, a magnetic thin film presents preferential direction of the magnetic ground energy to the direction perpendicular to the film.

There are two main sources of magnetic anisotropy stemming from the magnetic dipolar and the spin-orbit interaction. Due to the long range of dipolar interaction, a shape-dependent contribution in the magnetic anisotropy is induced leading to IP contributions. However, with the combination of spin-orbit interactions, a small orbital momentum is induced and couples the magnetic moment with the crystal axes. Resultantly, the total magnetic energy is directly connected with the orientation of the magnetization, adopting the crystal symmetry and this is defined as magnetocrystalline contribution. In the case of thin films the lowered symmetry strongly modifies this contribution, resulting in the emergence of the surface anisotropy as pointed out by Néel [34] giving rise to PMA.

2.3.1 Surface and volume contributions

To accurately identify the magnetic anisotropy of a thin film, one should distinguish between surface/interface (K_s) and volume (K_v) contributions, in line with Néel’s framework. The sum of both contributions leads to the determination of the measured effective anisotropy (K_{eff}). Figure 2.3 illustrates a simple representation of a trilayer system underlayer/FM/capping layer, indicating the individual contributions to the measured K_{eff} . K_s is equal to $K_s = K_{s_1} + K_{s_2}$, arising from both interfaces.

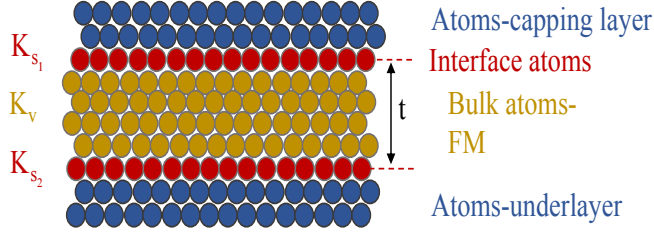


Figure 2.3. Qualitative draw of the contributions to the effective anisotropy in an underlayer/FM/capping layer system. The surface/interface and volume contributions arising from the interface atoms (red-points) and bulk atoms (yellow-points), respectively.

In particular, K_v contains two contributions, the magnetocrystalline (K_b) and shape (K_d) anisotropy. In 3d transition metals, such as Co, Fe, Ni, K_b originates from spin-orbit interactions. In such cases, the orbital magnetic moment has usually small contribution to magnetism and, thus, a low K_b is expected, e.g., $K_b = 4.1 \text{ Merg/ccm}$ for Co [35]. The K_d term equal to $-2\pi M_s^2$ stems from dipole-dipole interactions, creating a favorable energy term for magnetization aligned along the longitudinal axis of a thin film and an unfavorable one for magnetization aligned along the surface normal to the thin film. Therefore, K_{eff} is given by the equation

$$K_{\text{eff}} = K_b - 2\pi M_s^2 + \frac{K_s}{t_{\text{FM}}}, \quad (2.11)$$

where M_s and t_{FM} stand for the saturation magnetization and the F thickness. A plot of $K_{\text{eff}} t_{\text{FM}}$, as presented in Fig. 2.4, is commonly used in experimental studies providing with valuable information for the determination of ($K_b - 2\pi M_s^2$) and K_s considering the slope of the curve and the vertical axis intercept, respectively.

In general, we can distinguish between three cases of K_{eff} :

- a) Positive ($K_{\text{eff}} > 0$): K_s outweighs ($-2\pi M_s^2$) leading to a perpendicularly magnetized system.
- b) Zero ($K_{\text{eff}} = 0$): indicates a critical F thickness ($t_{\text{cr}}^{\text{FM}}$) where the transition of magnetization between IP to OOP occurs.
- c) Negative ($K_{\text{eff}} < 0$): The ($-2\pi M_s^2$) term dominates K_s leading to an IP magnetized system.

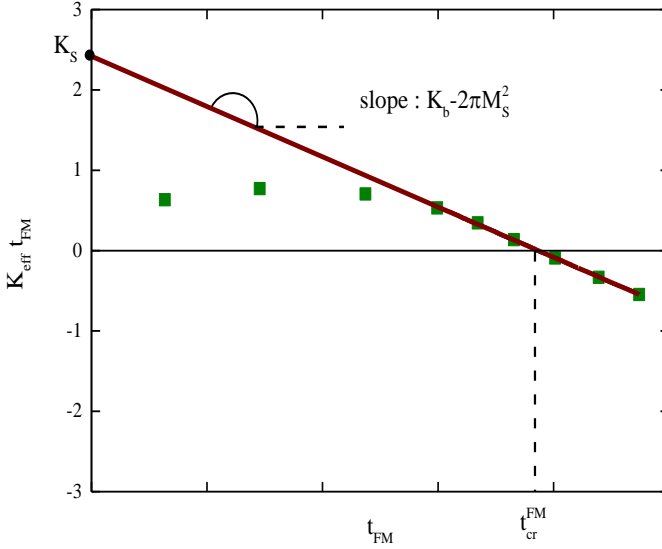


Figure 2.4. The $K_{\text{eff}}t_{\text{FM}}$ as a function of t_{FM} . The slope and the y-axis intercept of the straight line fit determine the K_v and K_s contributions.

Due to the reason that $K_b \ll K_d$, the $K_{\text{eff}}t_{\text{FM}}$ vs t_{FM} plot presents usually negative slopes, as indicated in Fig. 2.4. Additionally, it's worth mentioning that the ability of the system to become perpendicularly magnetized is proportional to the increase of the factor $\frac{K_s}{t_{\text{FM}}}$. In other words, the fabrication of films with PMA necessitates the increase of K_s and/or the decrease of t_{FM} .

2.3.2 Direct and indirect contributions on the formation of PMA in underlayer/CoFeB/MgO systems

In this subsection we will analyze a number of mechanisms which promote the large PMA in a trilayer system such as underlayer/CoFeB/MgO. In order to gain a deeper insight into the underlying physical mechanisms which take place and promote the PMA, we will distinguish between the favorable direct effects occurring in the individual CoFeB/MgO and underlayer/CoFeB interfaces and the indirect ones stemming from their interdependence.

In the CoFeB/MgO interface a large number of first principal calculations [36] and experimental works [37–40] have pointed out the emergence of

PMA from the hybridization of 3d Fe(Co) and 2p O orbitals. Furthermore, the aforementioned hybridization seems to have a universal character in the determination of PMA since it has also been reported in magnetic metal/oxide interfaces [41, 42].

Apart from the emergence of PMA in magnetic metal/oxide interfaces related to the formation of Fe(Co)-O bonds, the interfacial PMA first observed in the Co/HM system, where HM corresponds to a heavy metal, e.g., Pt, Pd [43]. The large PMA in such systems is an outcome of the hybridization of 3d Co orbitals with 5d orbitals of the HM.

In a recent work, Chen *et al.* [44] examined the establishment of PMA in an underlayer/CoFeB/MgO system (underlayer = Ti, V, Cr, Zr, Nb, Mo, Ru, Rh, Pd, Ag, Hf, Ta, W, Re, Os, Ir, Pt, and Au). They concluded that the major factor promoting the formation of PMA in the underlayer/CoFeB interface is the interfacial d-d hybridization of 4d/5d orbitals of the underlayer material with the 3d Fe(Co) electrons.

Apart from the two aforementioned mechanisms which contribute to the establishment of PMA in such trilayer systems, the removal of B atoms from the CoFeB/MgO interface could further contribute to the enhancement of PMA. As demonstrated in subsec. 2.2.4, B is theoretically predicted to be located at the CoFeB/MgO interface. Consequently, if the underlayer is a strong B absorber material, it would potentially remove more B atoms from the interface, enhancing the Fe(Co)-O bonding which is beneficial for the formation of strong PMA.

2.4 Exchange bias

In 1957, Meiklejohn and Bean [45] discovered a new type of unidirectional magnetic anisotropy in a system containing Co nanoparticles coated by a layer of AF CoO. This phenomenon usually referred to as EB. The origin of EB effect focuses on the coupling between the F and AF spins at the interface. Considering a M-H plot, the EB effect is reflected by the displacement of the hysteresis loop along the axis of the magnetic field (H) with respect to H=0. This displacement of the hysteresis loop was initially attributed to the existence of an oxide layer surrounding the Co particles. However, the authors in order to delve deeper into the effect's mechanism, conducted zero-field

cooled (ZFC) and field-cooled (FC) measurements at temperatures below the Néel temperature (T_N), recording the hysteresis loops of the aforementioned system. Remarkably, in the FC measurements they observed a displacement of the hysteresis loop accompanied with its broadening, whereas for the ZFC measurements no displacement was present. Although the EB effect has been extensively studied for more than four decades in a variety of FM/AFM systems, its microscopic origins remain controversial and under investigation. In the next subsections, we will separate the models used to explain the EB effect into three categories according to the length scale of the area with the same magnetic moment: macroscopic, mesoscopic, and microscopic.

2.4.1 Macroscopic models

Exchange bias phenomenology

In macroscopic models the AF and F layers are considered as homogeneous in the x - y plane. In addition, the spins of the AF layer are assumed to be uncompensated and parallel to the interface plane. In some of the models described here, i.e., Néel's [46] and Mauri's [47] models, the detailed spin structure in the z -direction of the FM and/or the AFM is also considered.

Figure 2.5 presents a qualitative draw of the EB in a F/AF bilayer, following the review of Nogués *et al.* [48]. The upper left part of Fig. 2.5 presents the initial state of the system with the AF layer being in the paramagnetic state since $T > T_N$. After the cooling down of the system through T_N and under the application of an applied magnetic field (H_{FC}), there is a transition of the initial paramagnetic state to an AF one. This procedure is called field cooling and due to the interfacial exchange interactions between the AF and F spins, the first monolayer of the AFM aligns parallel to the FM. In turn, the neighbouring monolayers in the AFM follow the interfacial pattern in a way to produce zero bulk magnetization. When reversing the field, the F spins tend to rotate to the opposite direction. However, due to the interfacial interactions between AF and F spins, the latter experience a torque from the former spins forcing them to remain in their initial position. Consequently, a stronger external magnetic field is needed to outweigh this coupling and rotate the F spins, resulting in the increase of the coercive field. When switching from negative to positive fields, the F spins require a smaller force in order to

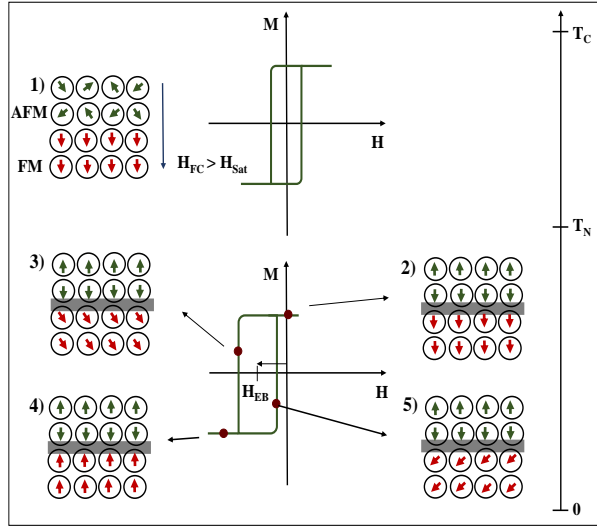


Figure 2.5. Phenomenological model of EB for an AF/F bilayer. Panels 1-5 present the individual spin configurations in the AF and F layers at different stages of the hysteresis loop.

rotate back to their original direction. This is an outcome of the energetically favorable torque which is induced on the F spins from the AF ones. Finally, the magnetization curve is shifted to negative values with respect to $H=0$ and this displacement of the center of the hysteresis loop is called EB field (H_{EB}).

The ideal Meiklejohn-Bean Model

Based on the phenomenology of the previous description, Meiklejohn and Bean (M-B) [45] developed a model under assumptions which treat the FM and the AFM individually as well as their interface, as indicated in Fig. 2.6(a).

- The FM rotates coherently and has uniaxial anisotropy with the easy axis being IP.
- Both the FM and AFM are in a single domain state.
- The AF layer has an IP uniaxial anisotropy and is magnetically rigid.
- The spins of the AF interface are fully uncompensated.

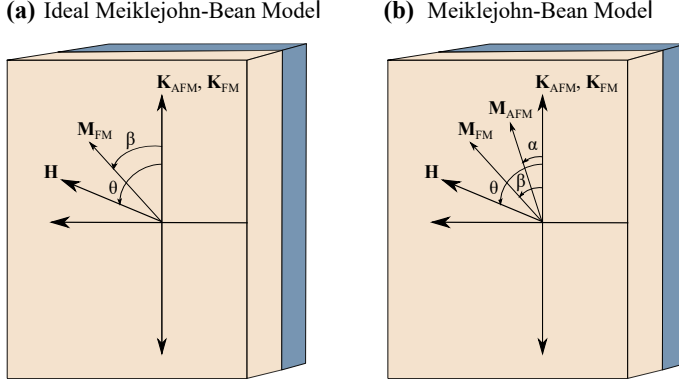


Figure 2.6. Schematic illustration of the angles and vectors used in the (a) ideal and (b) realistic Meiklejohn and Bean model.

- The AF/F interface is atomically smooth.
- The AFM and the FM are coupled at their interface with an exchange interaction. The exchange interaction is parameterized through the interfacial exchange coupling energy per unit area (J_{EB}).

Starting from the Stoner-Wohlfarth model [49, 50] for describing the coherent rotation of the magnetization vector, the energy per unit area (E_A) can be written as

$$E_A = -\mu_0 H M_{FM} t_{FM} \cos(-\beta) + K_{FM} t_{FM} \sin^2 \beta, \quad (2.12)$$

where M_{FM} is the saturation magnetization per unit volume of the FM, K_{FM} is the magnetocrystalline anisotropy constant, and β is the angle between the magnetization and the anisotropy axis of the FM. The first term of Eq. (2.12) describes the Zeeman energy of the system and the second one concerns the uniaxial anisotropy.

Meiklejohn and Wohlfarth in order to quantify the interface exchange coupling between the FM and the AFM inserted in Eq. (2.12) the phenomenological energy term $J_{EB} \cos(\beta)$ such that [51]

$$E_A = -\mu_0 H M_{FM} t_{FM} \cos(-\beta) + K_{FM} t_{FM} \sin^2 \beta + J_{EB} \cos(\beta). \quad (2.13)$$

After attaching stability conditions to the total magnetic energy with respect to the angle β , they resulted in the following formula for the H_{EB}

$$H_{\text{EB}} = \frac{J_{\text{EB}}}{\mu_0 M_{\text{FM}} t_{\text{FM}}}. \quad (2.14)$$

Despite the simplicity of the model's assumptions, the inverse proportionality of H_{EB} and t_{FM} is well established in literature [48], reflecting the interfacial character of the effect. However, the relation is no longer valid in some systems where t_{FM} is relatively thin, probably attributed to the discontinuous development of the F layer.

Moreover, in the previous analysis a positive character of the effect is assumed so as $H_{\text{EB}} < 0$ when $H_{\text{FC}} > 0$. The vast amount of hysteresis loops shown in literature are shifted oppositely to the H_{FC} direction. However, in MnF_2/FM [52] and FeF_2/FM [53, 54] systems there is the observation of a negative character of the effect ($H_{\text{EB}} > 0$ when $H_{\text{FC}} > 0$). For such systems, a more complicated analysis is required, taking into account the dependence of the EB on the magnetic domain sizes which are formed in the F and the AF layers.

A crucial parameter which should be considered in order to establish the EB in the field-cooling procedure is the temperature. For $T < T_{\text{N}}$, there is a critical temperature called blocking temperature (T_{B}) at which the EB is established. T_{B} is influenced by many parameters, e.g, roughness, thickness, grain size as well as the order of the AFM. However, $T_{\text{B}} \approx T_{\text{N}}$ is reported for thick films and single crystals [48].

Furthermore, within the model's framework the H_{EB} is expected to be several orders of magnitude larger compared to the experimentally observed one. The assumption of fully uncompensated AF interface plane is the reason of the anticipated large H_{EB} . A realistic F/AF interface deviates strongly from this assumption since the surface roughness and the complex interface chemistry lead to a complex magnetic structure.

The realistic Meiklejohn-Bean model

In the realistic approach of M-B model [45], as shown in Fig. 2.6(b), a new degree of freedom for the AF layer was introduced to account for the rotational hysteresis observed during the torque measurements. Particularly, the AFM is still rigid satisfying the previously introduced condition, but it can slightly rotate during the magnetization reversal as a whole. Therefore, a new energy

term is introduced in the Eq. (2.13) stemming from the anisotropy of the AF layer. Defining the small rotational angle (α) of the AF layer, the Eq. (2.13) takes the form [51]

$$E_A = -\mu_0 H M_{\text{FM}} t_{\text{FM}} \cos(\theta - \beta) + K_{\text{FM}} t_{\text{FM}} \sin^2(\beta) + K_{\text{AFM}} t_{\text{AFM}} \sin^2(\alpha) - J_{\text{EB}} \cos(\beta - \alpha), \quad (2.15)$$

where t_{AFM} is the AF thickness and K_{AFM} is the magnetocrystalline anisotropy constant. After the numerical analysis of Eq. (2.15) with minimization of E_A with respect to the α and β angles and having assumed that K_{AFM} is infinitely large, the expression of H_{EB} is extracted as follows

$$H_{\text{EB}}^{\infty} = \frac{J_{\text{EB}}}{\mu_0 M_{\text{FM}} t_{\text{FM}}}. \quad (2.16)$$

The parameter R which defines the ratio between the AF anisotropy energy and J_{EB} is given by the formula

$$R = \frac{K_{\text{AFM}} t_{\text{AFM}}}{J_{\text{EB}}}. \quad (2.17)$$

We can distinguish between two cases in a AF/F system:

- $R \geq 1$: The AF anisotropy energy is able to hold the AF order during the magnetization reversal, although there is the degree of freedom for the small rotation of angle α . Therefore, the H_{EB} is anticipated with the simultaneous absence of coercivity H_C .
- $R < 1$: The absence of H_{EB} is expected since the J_{EB} outweighs the AF anisotropy energy leading to the simultaneous rotation of the AF and F spins. The $H_C \neq 0$ suggests a typical hysteresis loop.

The Macroscopic domain wall models

As highlighted previously, one distinct failure of the M-B model regards the size of the EB effect which is expected to be several orders of magnitude higher than the experimentally determined one. In order to reconcile the experimental observations with the theoretical predictions, Néel [46] introduced a model with new assumptions allowing for the loss of the exchange coupling energy.

Later on, Mauri *et al.* [47], Kiwi *et al.* [55], Geshev *et al.* [56], and Kim *et al.* [57] in the spirit of Néel's approach used similar arguments for proposing their EB models.

The loss of the exchange coupling energy is attributed to the development of partial domain walls in the AFM or the FM during the magnetization reversal. According to Néel's model, the coupling between a FM and a low anisotropy AFM gives rise to the formation of either an AF or a F domain wall parallel to the interface. As a result, the planar domain wall will absorb a fraction of the interface exchange coupling energy, lowering the H_{EB} . Néel extracted quantitative results for J_{EB} and K_{AF} through a differential equation providing a magnetization profile in the AFM.

In summary, in the macroscopic domain wall models the formation of domains introduces the corresponding energy terms to the energy expression, influencing substantially the H_{EB} . The minimization of magnetic energy will determine the formation of domain walls in the FM and/or the AFM. In the equilibrium state, a significant weakening of the effective coupling will occur and it will be reflected as a drop of H_{EB} . In the strong interface coupling limit, the H_{EB} becomes

$$H_{\text{EB}} \propto \frac{\sqrt{K_{\text{AFM}}A_{\text{AFM}}}}{\mu_0 M_{\text{FM}} t_{\text{FM}}}, \quad (2.18)$$

or

$$H_{\text{EB}} \propto \frac{\sqrt{K_{\text{FM}}A_{\text{FM}}}}{\mu_0 M_{\text{FM}} t_{\text{FM}}}, \quad (2.19)$$

where $A_{\text{AFM (FM)}}$ is the AFM (FM) stiffness considering the formation of the domain wall in the AF (F) side of the interface.

2.4.2 Mesoscopic models

In contrast to the macroscopic models, the mesoscopic models suggest the existence of different spin configurations in the x - y plane. A representative model of this category concerns the one from Malozemoff [58–60]. The fundamental assumption of the model is a non atomically smooth F/AF interface. The interfacial inhomogeneities produce a random field leading to the breaking up of the AFM into domains with domain walls perpendicular to the

interface. In contrast to Néel's model, the AF domain walls are normal to the interface. The H_{EB} is given by the equation

$$H_{\text{EB}} \approx \frac{2\sqrt{K_{\text{AFM}}A_{\text{AFM}}}}{\pi^2 M_{\text{FM}} t_{\text{FM}}}, \quad (2.20)$$

where $A_{\text{AFM}} = J_{\text{AFM}}/\alpha_{\text{AFM}}$, with J_{AFM} to be the exchange coupling energy and α_{AFM} the lattice constant of the AFM.

Historically, the first mesoscopic model was proposed by Kouvel *et al.* [61] suggesting some lateral spin distributions in the AF domains in CuMn alloys to explain the presence of the EB effect. Further significant contributions were made by Fulcomer *et al.* [62], considering the effects of grain size distribution in EB. Based on this assumption, Stiles and McMichael [63] considered an assembly of AF crystallites of different sizes and anisotropy directions to compose a AF layer. The crystallites with strong AF/F coupling and easy axes close to the H_{FC} axis, have the tendency to switch together with the FM contributing to the H_{C} . In addition, the crystallites with weak AF/F coupling and easy axes deviating from the H_{FC} axis, will contribute mainly to the H_{EB} and less to H_{C} . Apart from the aforementioned models, more sophisticated ones are summarized in the review paper by Nogués *et al.* [64].

2.4.3 Microscopic models

In the microscopic models the detailed spin configuration of each atom (or groups of atoms) in the total examined volume is taken into account. Towards this approach there are models using Monte carlo simulations [65–67], micromagnetic simulations [68, 69] or different types of spin lattice models [70].

A well-known contribution in the category of microscopic models is the one of Koon [68]. In particular, in thin films with compensated F/AF interfaces the minimization of magnetic energy suggests the F and AF spins to get coupled perpendicularly to each other. The aforesated physical picture suggests a “spin-flop”-like state which occurs in AFMs. As a direct outcome, a new term $J_{\text{EB}}(S_{\text{AFM}}S_{\text{FM}}\cos(\alpha - \beta))^2$ is introduced in the energy equation (see Eq. (2.13)), with S_{AFM} (S_{FM}) to be the net magnetic moments of the AFM (FM). Furthermore, for the interpretation of EB Koon suggested that the AF spins are restricted to move in the plane of the interface during field reversal. As a

result, there is a completely reversible (no hysteresis) curve with H_{EB} close to the experimentally observed one in Co/CoO systems at low temperatures [45]. As new ideas and experiments continue to emerge in this field, more detailed picture of the underlying physics continues to develop.

2.5 Perpendicular EB in MnIr/CoFeB/MgO systems

Exchange-biased stacks have been framed by a strong technological interest in memory and sensor technology which is related with their properties to improve significantly the retention time of MTJs and to provide a wide sensing field range, respectively. In particular, after a large number of STT switching events, the magnetic states of the MTJs do not either “creep” to some intermediate state or completely reverse. For that reason, IP magnetized exchange-biased stacks were widely utilized in MTJs. Nevertheless, the interest rapidly changed towards the OOP magnetized systems for a plethora of practical reasons. Specifically, in the OOP magnetized systems the density of memory cells on a wafer can be considerably increased, the critical current density which is required to write information by STT switching is substantially smaller, and the retention of the memory is fairly longer. As a result, the realization of OOP magnetized stacks with large EB is of significant practical importance. In most common embodiments, the EB stacks act as a reference for readout of the stored information and are defined as “pinned” layers, e.g., CoFeB/MgO pinned by MnIr [71]. In the following, we will highlight a number of mechanisms of crucial importance which give rise to the establishment of perpendicular EB (PEB) in such stacks.

The first mechanism regards the enhancement of MnIr (111)-fcc texture which directly affects the observation of EB. In particular, it has been reported that the EB effect depends on the existence of the (111) MnIr texture in Ta/CoFe/MnIr/CoFe multilayers [72]. The enhancement of the (111)-fcc MnIr texture provokes an increase of both the averaged T_{B} and K_{AFM} of MnIr and, thus, the size of the effect increases [73].

The second mechanism is related with the competition of the IP and OOP components of anisotropy in the vicinity of the MnIr/CoFeB interface. Specifically, the MnIr/CoFe interface favors an IP magnetization and, therefore, PEB is not favored. In order to overcome this natural limitation Zhang *et al.*

[71] suggested the enhancement of the OOP components of anisotropy via inserting an ultra thin layer, i.e., dusting layer, of CoFe/Ta between MnIr and CoFeB.

The procedure of the enhancement of the OOP components via the introduction of a dusting layer seems to have a universal character since it has also been reported in MnIr/[Co/Pt]_n [74] and MnIr/CoFe/Co/[Pt/Co] [75] systems, where the PEB is drastically enhanced in a proportional way. In a phenomenological approach, these findings could be interpreted using the formula for H_{EB} given by the M-B model [74]

$$H_{EB} = J_{EB} \frac{S_{AFM}^P S_{FM}^P}{\mu_0 \alpha_{AFM}^2 M_{FM} t_{FM}}, \quad (2.21)$$

where $S_{AFM(FM)}^P$ is the net magnetic moment for the AFM (FM) perpendicular to the film. The enhancement of the OOP components would lead to the enhancement of S_{FM}^P resulting in large PEB. Conclusively, the use of buffer layers, such as Pd, Pt, Cu, Ru, together with the introduction of a dusting layer between MnIr and CoFeB contribute significantly to the establishment of PEB in MnIr/CoFeB/MgO based stacks.

Additionally, the EB effect is influenced by the chemical nature, i.e., possible atomic intermixing, as well as the interface roughness. As an example, in the Mn_xPt_{1-x}/Co system [76] the interdiffusion of the highly miscible materials Co and Mn during the annealing procedure [77] leads to the degradation of H_{EB} .

According to Malozemoff model [58–60], the reduction of the overall EB energy is an outcome of the interface roughness which may induce magnetic frustration [76]. The introduction of a non magnetic dusting layer can decrease the magnetic frustration and simultaneously increase the H_{EB} . However, there is a critical thickness of the non magnetic dusting layer above which the AFM and FM become totally decoupled. In the MnIr/CoFeB/MgO based stack examined in this thesis, a number of Ta atoms of the dusting layer probably reach the AF/F interface through the pin holes of the FM, forming a non magnetic layer with analogous impact on the H_{EB} .

2.6 Magnetostatic coupling effects in FM/NM/FM systems

As analyzed previously in the thesis, the FM/NM/FM trilayer system is the backbone of the magnetoresistive devices which are widely used in magnetic field sensor and MRAM applications. Elucidating the role of the magnetostatic interactions between the F layers is critical for the development of advanced magnetoresistive devices. Therefore, huge research efforts have been invested towards the realization of the magnetostatic coupling effects.

The interlayer exchange coupling (IEC) is one of the proposed mechanisms to explain the magnetostatic coupling effects. In a Fe/Cr/Fe trilayer system, the observed oscillatory behaviour of IEC as a function of the NM layer thickness, was related by Mathon, Villeret, and Edwards [78] to the confinement of Fermi surface electrons in the NM. Some years later, M. Stiles [79] and P Bruno [80, 81] extended the model to include the interfacial NM/FM contributions to the spin-dependent electron reflectivity. In a FM/NM/FM trilayer system where NM is an insulating barrier, the IEC was interpreted through the spin-current model [29, 81].

The magnetostatic interactions between the F layers give rise to additional magnetostatic coupling mechanisms. In particular, rough interfaces lead to a surface magnetic charge density and consequently to dipolar coupling. This type of coupling is widely known as “orange peel” coupling and introduced by Néel in 1962 [82] to interpret the magnetostatic coupling in FM/NM/FM IP magnetized systems. In 2004, Moritz *et al.* [83] extended the model in perpendicularly magnetized systems.

2.6.1 IEC: Slonczewski and Bruno models

In 1989, Slonczewski [29] explained the IEC in a trilayer FM/NM/FM system with insulating spacer in the framework of the spin-current model. The tunnel spin current induces a magnetic torque which is exerted by one F layer on the other, leading to exchange coupling effects. According to the model, the IEC strength (J) presents a non-oscillatory exponential decay with increasing the spacer thickness (D) which stems from the exponential decay of the F wave functions into the insulating spacer.

In Bruno's model [81], the core idea is based on the quantum interference of the spin-dependent reflected electron waves, arising from the NM/FM interfaces. The multiple internal reflections in a magnetic layer of finite thickness create the analogous physical picture with the reflection oscillations in an optical Fabry-Perot cavity. In FM/NM/FM systems, the FM/NM interfaces represent the two highly reflecting mirrors of the Fabry-Perot cavity.

Specifically, the J of a FM/NM/FM system under the assumptions of relatively large spacer thickness (D) and finite t_{FM} (L), is described by the equation [81]

$$J = \frac{\hbar^2}{8\pi^2 m} \text{Im} \left[\frac{r_{\infty}^{\downarrow 2}}{2} \exp(2ik_{\text{F}}D) \left[\frac{k_{\text{F}}^2}{D^2} - 2(1 - r_{\infty}^{\downarrow 2}) \left(\frac{D}{k_{\text{F}}} + \frac{L}{k_{\text{F}}^{\downarrow}} \right)^{-2} \exp(2ik_{\text{F}}^{\downarrow}L) \right] \right], \quad (2.22)$$

where r_{∞}^{\downarrow} is the reflection amplitude and $k_{\text{F}}^{\downarrow}$ is the Fermi vector for the minority spin (\downarrow) of the F layer. Considering the presence of the term $\exp[2ik_{\text{F}}D]$ in the Eq. (2.22), we extract the oscillatory behaviour of J with D for metallic spacer (k_{F} real) and the corresponding exponential decay for the case of insulating spacer (k_{F} imaginary). Moreover, the presence of the term $\exp[2ik_{\text{F}}^{\downarrow}L]$ suggests an oscillatory behaviour of J with L having a period of $\pi/k_{\text{F}}^{\downarrow}$.

In addition, Bruno's model predicts the thermal variation of J for the two previously mentioned kinds of spacer given by the equation

$$J(T) = J(0) \frac{2\pi k_{\text{B}} T D m / \hbar^2 k_{\text{F}}}{\sinh(2\pi k_{\text{B}} T D m / \hbar^2 k_{\text{F}})}. \quad (2.23)$$

From Eq. (2.23) a strong decrease (increase) of J is expected for the case of metallic (insulating) spacer with the increase of temperature since k_{F} is real (imaginary) for the metallic (insulating) spacer.

2.6.2 Orange peel coupling in systems with PMA

In 1962, Néel [82] first studied the magnetostatic coupling between two F electrodes IP magnetized in a FM/NM/FM trilayer system. The core idea of "orange peel" coupling is based on the fact that the surface topography, in particular the interface roughness, leads to a surface magnetic charge density and, consequently, to dipolar coupling. Assuming that the buffer magnetic layer has a sinusoidal roughness, the NM spacer will follow that interfacial

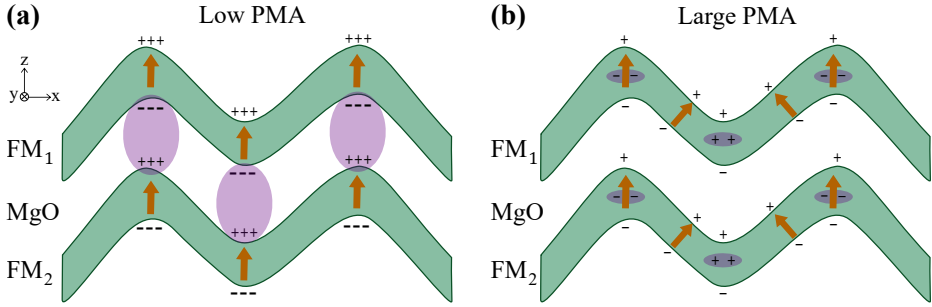


Figure 2.7. Illustration of the magnetization configuration in a $FM_1/NM/FM_2$ trilayer system in films with (a) low and (b) large PMA. For the systems with low (large) PMA the interfacial (volume) charges dictate the F (AF) coupling between the two electrodes.

pattern reproducing an identical roughness to the one of the buffer layer. In turn, the capping F layer will adopt the roughness profile of the NM spacer. As a result, the successive interfaces present the same in-phase waviness and, thus, can be regarded as correlated. The IP magnetization combined with the rough interface will give rise to the creation of dipole charges in both F layers. Additionally, in the parallel (antiparallel) alignment of the F layers, the magnetic dipoles form a closed (open) magnetic pattern suggesting an energetically favorable (unfavorable) state. The coupling energy could be represented by the exponential relation of

$$J = \frac{\mu_0 \pi^2 h^2 M_1 M_2}{\sqrt{2} \lambda} \exp\left(-\frac{2\pi \sqrt{2} D}{\lambda}\right), \quad (2.24)$$

where μ_0 is the permeability of free space, $M_{1(2)}$ is the magnetization of the $F_{1(2)}$ electrodes, h and λ the amplitude and the wavelength of the waviness of the correlated interface of the spacer.

Some years later, Moritz *et al.* [83] suggested that in films with PMA the antiparallel magnetic orientation of dipoles can be also energetically favorable as an interplay of the magnetostatic, exchange, and anisotropy energy. As depicted in Fig. 2.7(a), for films with low PMA the magnetization remains parallel to the z -axis because of the exchange stiffness and the minimization of the surface charges. The surface charge densities are opposite promoting the F coupling. On the contrary, for films with strong PMA the magnetization remains perpendicular to the interface, as depicted in Fig. 2.7(b). Due to

the magnetization's x -components, the creation of volume charges is favored locally, promoting the AF coupling.

2.6.3 Methodology for the determination of magnetostatic coupling

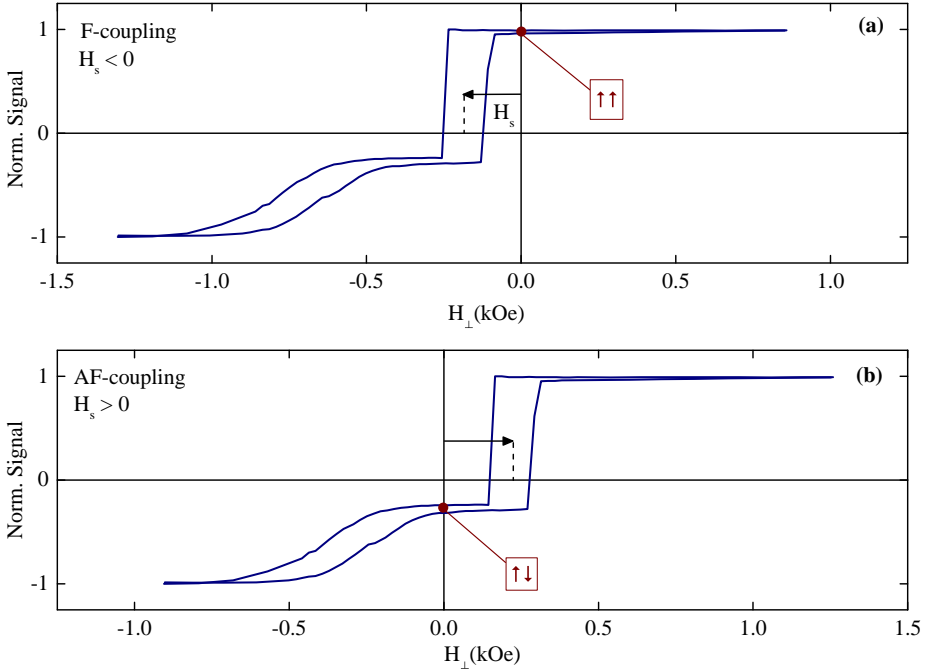


Figure 2.8. Examples of (a) F and (b) AF coupling in p-MTJs with EB.

In order to identify the character (F or AF) and the strength (J) of magnetostatic coupling between both F electrodes, one can examine the shift (H_s) of the hysteresis loop with respect to $H = 0$ which corresponds to the soft magnetic electrode. Figure 2.8 presents hysteresis loops for a p-MTJ with EB, containing a dominant F (cf. Fig. 2.8(a)) and AF (cf. Fig. 2.8(b)) coupling. In Fig. 2.8(a), when H_s is negative ($J < 0$) a parallel orientation between the pinned and the soft electrode is achieved at zero field (red point), suggesting a F coupling. On the contrary, in Fig. 2.8(b) when H_s is positive ($J > 0$) an

antiparallel orientation of both electrodes at zero field is observed, dictating an AF coupling between the electrodes.

The strength of the magnetostatic coupling is given by the equation

$$J = \mu_0 H_s M_s^{\text{SE}} t_{\text{SE}}^{\text{eff}}, \quad (2.25)$$

where M_s^{SE} and $t_{\text{SE}}^{\text{eff}} = t_{\text{FM}} - t_{\text{DL}}$ are the saturation magnetization and the effective F thickness of the soft electrode. The effective F thickness stems from the subtraction of t_{FM} with the dead layer (t_{DL}) thickness. The M_s and t_{DL} can be extracted via a series of measurements of the saturation magnetization per unit area ($M_s t_{\text{FM}}^{\text{eff}}$) as a function of the F thickness. When fitting the experimental data with a linear regression, the M_s and t_{DL} correspond to the slope and the intercept of the linear fit, respectively. The determination of t_{DL} allows us to quantify the effective F volume and, thus, to accurately identify the coupling strength.

2.7 Magnetic memories and sensors

The advent of MTJs concerns the landmark point for magnetoresistive technology. Nowadays, most of the MRAM embodiments exploit MTJs as memory unit cells. Simultaneously, in a plethora of magnetic field sensors MTJs are utilized in order to convert an external magnetic field into a resistance value. In the subsecs. 2.7.1 and 2.7.2 two types of MRAM will be discussed, the field-driven and the STT-MRAM. We will analyze the principles of reading and writing operations, as well as, we will highlight the advantages of the STT-MRAMs over their field-driven counterparts. Additionally, in subsec. 2.7.3 we will present a number of engineering strategies which provide the optimum sensing scheme in an MTJ-based magnetic field sensor.

2.7.1 Field-driven MRAM

The first development of MTJ-based MRAM was the field-driven MRAM, combining a cross point architecture, as illustrated in Fig. 2.9(a). It consists of two arrays of conducting wires running perpendicularly to each other on a chip. At the crossing points, the placed MTJs are connected in series with a selection transistor. The high (low) resistance state of the junctions

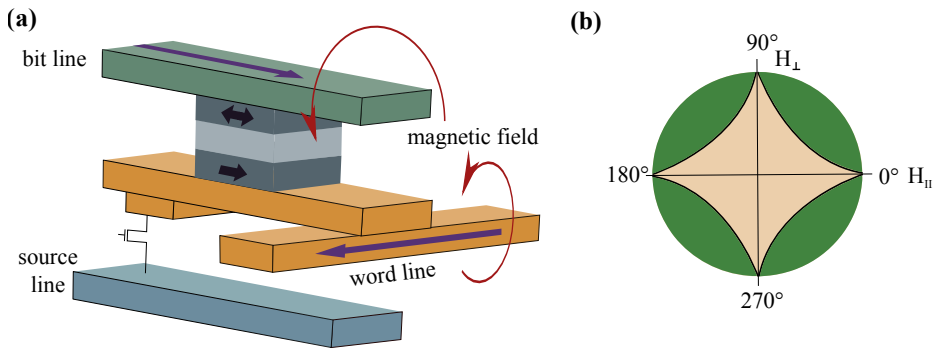


Figure 2.9. (a) Schematics of the writing principle in a Field-driven MRAM. The two driven currents (purple arrows) in the bit and word lines are presented, along with their corresponding magnetic fields (red arrows). (b) The Stoner–Wohlfarth astroid curve. With light brown (green) colour is indicated the region with two (one) minima (minimum) of the free energy. The magnetization switching occurs when the applied magnetic field lies in the green region.

corresponds to logic 1 (0) bit and as a result one bit can be stored. The basic principle to read the information is based on the application of a read current which flows through the MTJ and senses its magnetic state from the value of the cell resistance. In addition, in order to write at a particular addressed cell, two simultaneous pulses of current are sent in the bit and word lines which cross each other at the addressed MTJ cell. These currents create a large enough local magnetic field at the addressed cell to switch its storage layer magnetization. Specifically, Fig. 2.9(b) shows the Stoner-Wohlfarth astroid of a idealized soft layer (single magnetic domains) which undergoes two perpendicular field pulses. With H_{\parallel} (H_{\perp}) is symbolized the switching field parallel (perpendicular) to the easy axis. The Stoner-Wohlfarth astroid is the geometric representation of the Stoner-Wohlfarth model. According to the model, any applied magnetic field can be resolved into two components along the hard and easy directions. When the applied magnetic field vector lies in the light brown coloured region, there are two minima of the free energy one stable and one metastable and, thus, the initial magnetization direction remains unchanged. Whereas, when the total magnetic field vector falls out of the Stoner–Wohlfarth astroid (green regions), a magnetization switching

occurs [84, 85]. Consequently, a sequence of logic bits is selectively created corresponding to stored information [21].

2.7.2 Spin-Transfer Torque Magnetic Random Access Memory (STT-MRAM)

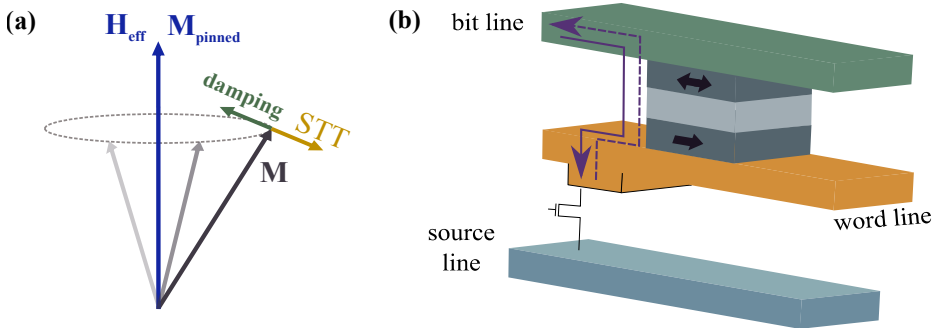


Figure 2.10. (a) Illustration of the magnetization precession according to Landau–Lifshitz–Gilbert–Slonczewski equation. With green and orange arrows are symbolized the damping and spin transfer torques, respectively. (b) Qualitative draw of the writing principle in STT-MRAMs. A current density (purple) is sent through the MTJ leading to a selective flip of the magnetization depending on the current flow direction.

As mentioned in subsec. 2.7.1, the writing process of the information in an MRAM cell necessitates the use of a local magnetic field which stems from a pulse current in the bit and word lines. However, two of the most significant obstacles arising from this process regard the large energy consumption to generate such fields and the independence of the writing current's amplitude on the size of the MTJ. The latter, leads to a drastic limitation of the down-scaling of the MTJs which is a criterion of high technological importance. The exploitation of STT in MRAM [86, 87] was proposed to overcome this limitation establishing a new era in the field of spintronics with the advent of STT-MRAM (see qualitative draw in Fig. 2.10(b)). STT regards the effect in which the magnetization of a F layer in a MTJ/spin valve can be modified using a spin-polarized current. Specifically, in a $FM_1/NM/FM_2$ trilayer system an applied charge current in FM_1 becomes spin polarized with spin polarization along the magnetization orientation of FM_1 . In turn, under the consideration

that the electrons propagate ballistically through the barrier and reach the NM/FM₂ interface, the electrons align their spin orientation with the local magnetization direction of FM₂. In order the spin angular momentum to be conserved, a magnetic torque will be created to the FM₂ which tends to align its magnetization with the magnetization of FM₁. The magnetization orientation of FM₂ can be switched if the magnetic torque is sufficiently large. The magnetization dynamics in STT-MRAM applications are described by the *Landau–Lifshitz–Gilbert–Slonczewski* (LLGS) equation [88]

$$\frac{\partial \mathbf{M}}{\partial t} = -\gamma \mathbf{M} \times (\mu_0 \mathbf{H}_{\text{eff}}) + \frac{\alpha}{M_S} \left[\mathbf{M} \times \frac{\partial \mathbf{M}}{\partial t} \right] + \frac{\gamma}{\mu_0 M_S} \boldsymbol{\tau}, \quad (2.26)$$

which stems from the Landau-Lifshitz-Gilbert (LLG) [89] with the introduction of a STT term ($\boldsymbol{\tau}$) from Slonczewski given by

$$\boldsymbol{\tau} = c \left[\mathbf{M} \times [\mathbf{M} \times \mathbf{n}] \right] + d [\mathbf{M} \times \mathbf{n}], \quad (2.27)$$

where γ is the gyromagnetic ratio, \mathbf{M} is the magnetization of the soft electrode, \mathbf{H}_{eff} stands for the effective magnetic field in which \mathbf{M} is aligned at equilibrium, α is the Gilbert damping constant, c and d are current-dependent functions for the IP and the perpendicular torque, and \mathbf{n} is the normalized vector of the magnetization of the pinned layer.

Figure 2.10(a) depicts the magnetization precession according to LLGS equation. Specifically, the first term of the right hand side of Eq. (2.26) describes the precession of the magnetization of the soft electrode around the \mathbf{H}_{eff} , which is determined by the pinned electrode. The second term predicts the establishment of a stable magnetic state after a certain time, due to the energy dissipation processes and is defined as damping term. The third term refers to the magnetic torque which is imposed to the soft magnetic electrode from the pinned one that is provided via the $\boldsymbol{\tau}$ term.

Figure 2.10(b) illustrates qualitatively the principle of writing in a STT-MRAM. In particular, in this configuration the relative parallel (antiparallel) magnetic configuration between both electrodes is accomplished, since the current flows from the soft (pinned) electrode towards the pinned (soft) one. In both cases, the two F electrodes will exchange torques which can, above a critical current density, lead to a flip of the magnetization of the FM as illustrated in Fig. 2.10(b).

This procedure concerns a powerful tool for the selective writing by simply changing the sign of the current. In STT-MRAM systems considerably smaller writing currents, e.g., $13\ \mu\text{A}$, are calculated (for further details see Ref. [21]) compared to the field-driven MRAM ones, e.g., some mA, leading to much more energetically favorable devices. In addition, the downsize scalability of the elements is favored since the required critical writing current decreases in proportion to the cell area [21]. Moreover, in STT-MRAM a very good write selectivity is accomplished since the STT current flows only through the selected cells. On the contrary, in conventional MRAM the writing current flows in the entire word line with the risk of writing an unselected cell. Apart from the high number of advantages, a potentially serious disadvantage concerns the magnetic disturbances to the MTJ which are induced during read events, as a consequence of the usage of the same path from both the writing and reading currents. As a result, an undesired change of the magnetic state can occur causing a bit reverse. In order to prevent possible parasitic writing events during reading, the reading current must present much lower values compared to the STT critical writing current for switching.

2.7.3 Magnetic sensors

A magnetoresistive device is a solid-state transducer which directly converts an external magnetic field into a resistance value. All these devices have a minimum and a maximum resistance plateau and the path from the one level to the other can be engineered to be linear, allowing them to work as magnetic sensors.

A typical MTJ sensor consists of two F electrodes separated by a NM spacer. The magnetization direction of the one F electrode is fixed through the EB effect (reference layer), while the other electrode is free to rotate in response to a low external field (sensing layer). For an ideal magnetic sensor the magnetoresistance loop of the sensing electrode must be linear and hysteresis free within the intended field operating range and its magnetization to be rotated coherently. Therefore, the sensing and reference layers are set orthogonal to each other and the external magnetic field is applied perpendicular to the sensing electrode and parallel to the reference one.

Several strategies can be followed to achieve this magnetic configuration using different effects [16]. One of the strategies takes advantage of the

self-demagnetizing field of the sensing layer [90]. In such systems, the sensor designing utilizes the shape anisotropy as the sensing electrode is patterned in a rectangular shape, with its longest dimension orthogonal to the reference one. One additional technique exploits superparamagnetic sensing electrodes [91]. Using a thin enough CoFeB layer, a linear hysteresis-free response is achieved with simple designs and low power consumption. In this case, the requirement of pattern elements with large aspect ratios is not necessary. The most widely used technique incorporates the use of weak exchange biased sensing layers [92, 93]. In this sensor structure, an AF layer is not only used in the pinned electrode but also in the sensing one. Also, the H_{EB} in the sensing electrode must be small as it will define the sensor saturation field and, therefore, its sensitivity. In order to achieve the orthogonal magnetization direction of both electrodes, the exchanged coupled interfaces in the pinned and the sensing electrode are chosen with different thermal stabilities. Different blocking temperatures are obtained between both electrodes either by the use of different AF materials or by the use of the same material with different thickness. Last but not least, the achievement of orthogonal orientation between the magnetization directions of the electrodes is additionally accomplished via the use of sensing films with strong PMA. This engineering strategy paves the way for the fabrication of nano-scale magnetic sensors with simple design, high sensitivity, and low power consumption [19].

2.8 p-MTJs vs. i-MTJs for MRAM applications

In Sec. 2.5 some of the advantages of the OOP magnetized systems over their IP counterparts for their use in MTJs were exhibited in broad terms. In this section, these advantages along with some additional features will be analyzed in detail, pointing out the significance of the use of p-MTJs compared to IP magnetized MTJs (i-MTJs) in memory applications.

p-MTJs have the potential of delivering the downsize scaling easier and, thus, increasing the density of the memory cells in a magnetic memory. Since shape anisotropy does not play any role to stabilize the magnetic anisotropy, magnetic cells can be made circular instead of elliptical, increasing significantly the available space for the development of MTJs in an MRAM.

Furthermore, a key characteristic for memory applications is the retention time which quantifies the time for which the system is capable to keep the written information unchanged. However, in MRAM the information may get corrupted by unintended switching of the magnetization of the storage layer due to thermal fluctuations or magnetic STT switching events, as described in Sec. 2.5. Consequently, the fabrication of MRAM storage elements with large retention times necessitates the consideration of thermal effects. p-MTJs are valued for their thermal robustness at small device sizes retaining the magnetic state in the storage layer. In particular, the reduction in size must be compensated by an increase in the anisotropy field (H_K) to maintain a desired thermal stability factor. In the case of p-MTJs, the H_K has an intrinsic character dictated by the large K_{eff} [40, 94]. This implies that the down-scaling of the devices doesn't affect the H_K considerably. On the contrary, the H_K in i-MTJs is strongly dependent on the geometrical characteristics of the devices and, therefore, it is significantly affected by the reduction of the device size.

Additionally, the critical current density (J_{cr}) for the p-MTJs is expected to be smaller. According to LLGS equation [88] the J_{cr} which is necessary for the magnetization switching is given by

$$J_{\text{cr}} = \frac{2ae\mu_0 M_S t_{\text{FM}}}{\hbar P} H_{\text{eff}}. \quad (2.28)$$

The expression of J_{cr} dictates a number of engineering strategies to realize which parameters must be modulated for reducing the power consumption for spin-transfer-induced switching. Highly polarized materials (large P) with a strong tendency to switch their magnetic state under the application of a STT (low a) current are the optimum candidates. Therefore, p-MTJs with large K_{eff} dictating a high polarization are expected to have a positive contribution. Materials which meet the aforementioned criteria are p-MTJs based on CoFeB with MgO barrier. Indicatively, for CoFeB, Co/Pd, and Co/Pt, the damping constant is reported to be equal to $\alpha_{\text{CoFeB}} = 0.01$ [95], $\alpha_{\text{Co/Pd}} = 0.1$ [21], and $\alpha_{\text{Co/Pt}} = 0.2$ [21], respectively, ranging within one order of magnitude. The reason of that pronounced difference is that a depends on the amplitude of the spin-orbit interactions in a proportional way. In particular, in Co/Pt and Co/Pd systems a strong spin-orbit coupling has been reported, stemming from the hybridization of the 3d Co with the 5d Pt or Pd orbitals. Whereas, in CoFeB/MgO systems a weak spin-orbit coupling has been realized due to

the hybridization of the 3d Co and Fe with the 2p O orbitals, with analogous impact on a .

Furthermore, the effective switching field is equal to $H_{\text{eff}} = H_K - 4\pi M_S$ and $H_{\text{eff}} = H_K + 2\pi M_S$ for p-MTJs and i-MTJs, respectively, and via Eq. (2.28) the lowest J_{cr} is expected in the first case. Phenomenologically, in i-MTJs the shape anisotropy term tries to keep the magnetization in the plane, introducing an additional energy barrier to be overcome for switching the magnetization compared to the p-MTJs.

Another interesting feature of p-MTJs regards the reduction of dipole field interactions between neighboring cells in high bit density layouts. The elliptical shape patterned i-MTJs create a dipole field larger in range compared to the circular p-MTJs. Thus, in the i-MTJs it is highly probable for the magnetic state of neighboring cells to feel the magnetic disturbances affecting the stored information.

Sample preparation

In the herein thesis thin film stacks for spintronic applications are investigated. The experimental methods used for their fabrication, analysis, and characterization are introduced in the following sections. The deposition of thin films of the order of several nanometers by magnetron sputtering and the annealing treatment are discussed in Sec. 3.1. The preparation of p-MTJs via electron beam (e-beam) lithography is analyzed in Sec. 3.2. Simultaneously, an introduction to the crystal structure analysis methods is given in Sec. 3.3. The magnetic and chemical analysis of the films are discussed in Secs. 3.4 and 3.5, respectively.

3.1 Thin film fabrication

The layer stacks investigated in this thesis are deposited by RF and DC magnetron sputtering on an SiO_2 substrate, from high purity elemental targets (99.9% or higher) in an ultra high vacuum (UHV) sputtering chamber (base pressure 10^{-9} mbar). In this case the elemental targets are bombarded by an argon (Ar) plasma, with a typical pressure of 2×10^{-3} mbar, having been stemmed from the collisions between the Ar gas atoms and the emitted electrons of the target. The outcome of the aforementioned bombardment of the target is the ejection of surface atoms which in turn are deposited on

the substrate positioned above the source (sputtering) as depicted in Fig. 3.1. In order to increase the sputter yield, a suitable magnetic field is placed under the target material which forces the electrons to cause more ionizing collisions with Ar atoms near the target surface and, thus, higher deposition rates (magnetron sputtering). After the deposition of a multilayer stack a step of thermal annealing is performed under certain vacuum ($< 3 \cdot 10^{-7}$ mbar), temperature/time conditions in the presence of a magnetic field of 7 kOe applied perpendicular to the film plane. This step is necessary to obtain the desired physical properties in the system, i.e., the crystallization of the initially amorphous CoFeB electrodes, the emergence of PMA, and the establishment of EB.

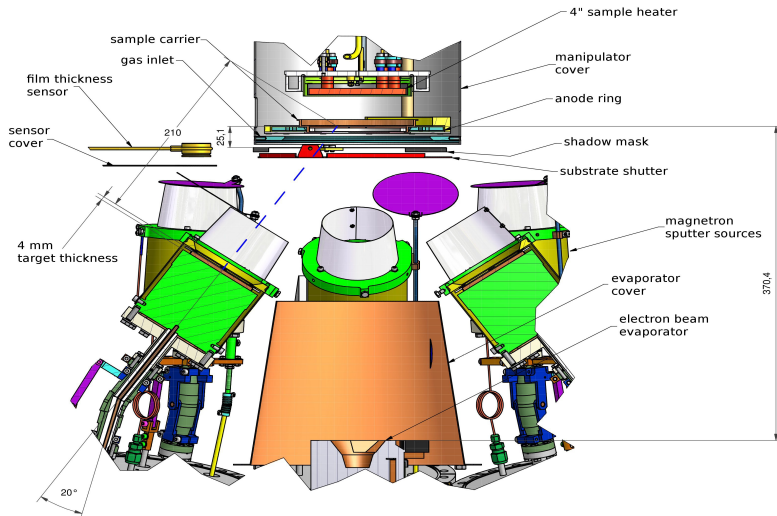


Figure 3.1. Schematic representation of BESTEC Co-sputtering system [96].

3.2 p-MTJ preparation via e-beam lithography

After the deposition and thermal annealing, the sample stacks are patterned via using two e-beam lithography steps. Firstly, the MTJ pillars are developed by e-beam lithography and subsequent Ar ion etching. In these steps, the redundant material between the circular pillars is removed via Ar etching

down to the bottom contact. During the etching process, the secondary ion mass spectroscopy is performed in order to obtain and control precisely the depth profile of the structure. In order to isolate the individual junctions electrically, 120 nm of Ta_2O_5 is sputtered next to the MTJ pillars. In turn, 5 nm of Ta and 60 nm of Au are deposited on the whole sample and patterned into bond pads. The material sequence of the stack is the same in all cases, apart from the capping layer of the soft F electrode as depicted in Fig.3.2. In addition, the individual layer thicknesses of the stack can vary. The numbers in parentheses present the nominal thicknesses in nm.

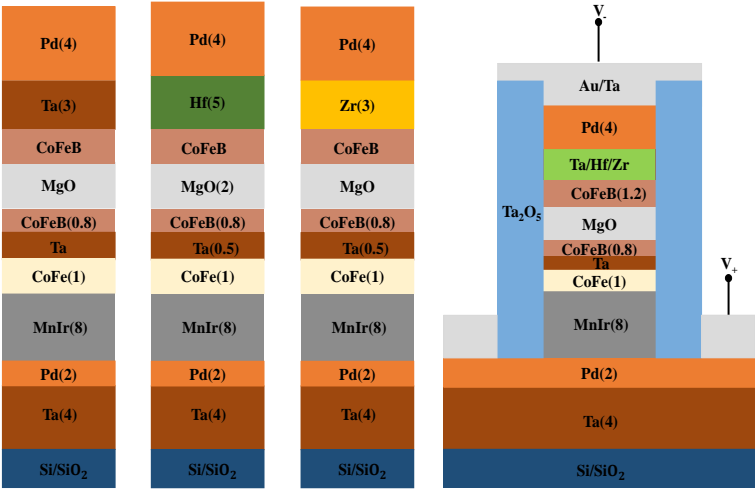


Figure 3.2. Sketches of the p-MTJs with EB stacks using different Ta (red), Hf (green), Zr (yellow) capping layers along with the schematic view of the patterned MTJs.

3.3 Structural analysis

In order to gain insight into the structural properties of our samples and precisely estimate the film crystallinity as well as the layer thickness and roughness, x-ray diffraction (XRD) and x-ray reflectivity (XRR) investigations were conducted. Wilhelm K. Röntgen was the German Physicist who received the first Nobel prize in Physics in 1901 for his discovery of x-rays [97]. Since then, a plethora of x-ray based characterization techniques have been developed as powerful tools to investigate the crystal and electronic structure as

well as the composition, due to the fact that x-rays enable a non-destructive vision into regions buried deep within the probed material. In the following subsections, the techniques used to analyze the structural properties in this work are summarized.

3.3.1 X-ray diffraction

XRD concerns an analytical technique which reveals information about the structural properties of solids such as crystal structure determination, phase identification, texture analysis, crystallite size and micro-strain analysis. When a sample is irradiated with a parallel beam of monochromatic x-rays, the atomic lattice of the sample cause the diffraction of the impinging x-rays to specific angles. In particular, depending on the angle of the incident beam θ with respect to the surface of the sample, the outcoming beam will undergo constructive interference according to the Bragg's law [98]

$$k\lambda = 2d_{\text{hkl}}\sin\theta, \quad (3.1)$$

with k as an integer, λ as the wavelength of the x-rays, d_{hkl} as the distance between two neighbouring lattice planes, and (hkl) as the corresponding Miller indices. Considering a cubic system, the lattice spacing between crystal layers is given by

$$d_{\text{hkl}} = \frac{a}{\sqrt{h^2 + k^2 + l^2}}, \quad (3.2)$$

with a as the out-of-plane lattice parameter. The total intensity of the XRD spectrum I_{hkl} is measured by the detector and presents an analogy to the structural factor $F(hkl)$ such that $I_{\text{hkl}} \propto |F(hkl)|^2$, considering the Laue conditions. The structural factor can be expressed by [98]

$$F(hkl) = \sum_{i=1}^n f_i e^{-i\mathbf{r}\cdot\mathbf{q}}, \quad (3.3)$$

considering the multiplication of the sum of the atomic factors f_i of every atom with a phase factor $e^{-i\mathbf{r}\cdot\mathbf{q}}$, where \mathbf{r} denotes the position vector of each atom and \mathbf{q} concerns the scattering vector. As a next step, the electronic density can be determined via using the Fourier transformation which unveils the distribution of the atoms in the unit, identifying the structure of the crystal.

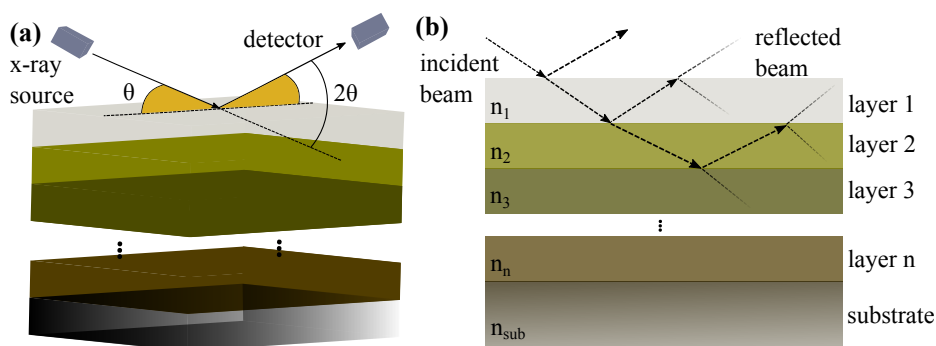


Figure 3.3. (a) Bragg-Brentano configuration utilized for the structural sample analysis. (b) XRR measurement sketch in a multilayer structure. Reflection and transmission of the incident beam at the surface and interfaces in several optically different media with the corresponding refractive indices n .

The XRD experiments in this work have been conducted in a Philips X'Pert Pro MPD diffractometer, in a Bragg-Brentano geometry ($\theta/2\theta$). This geometry necessitates the source-to-sample distance to be constant and equal to the sample-to-detector distance, while the x-ray source and the detector are moved against each other as sketched in Fig. 3.3(a). The x-ray tube generates Cu K_α radiation of $\lambda = 1.5419 \text{ \AA}$ and the detector side is equipped with a graphite monochromator.

3.3.2 X-ray reflectivity

XRR is a well established surface- and interface- sensitive technique, providing a powerful tool for the characterization of single- and multilayer thin films. In particular, the analysis of the XRR pattern of a multilayer film can yield information regarding the thickness, density, surface or interface roughness, and optical parameters of the corresponding layer. In addition, a major advantage of this technique is that it can be applied in amorphous materials, under the restriction that their interfaces are distinct enough. The XRR method is based on the reflection of the incoming x-ray beam by the sample's surface and interfaces (cf. Fig. 3.3(b)). The outgoing x-rays may interfere constructively or destructively with each other, leading to an oscillation pattern presenting the characteristic Kiessig fringes. The analysis of the corresponding

Kiessig fringes can provide information regarding the thin film structural parameters. The layer thickness can be estimated by the formula [99]

$$d = \frac{\lambda(m-l)}{2(\sin(\theta_m) - \sin(\theta_l))}, \quad (3.4)$$

where θ_m and θ_l denote the corresponding angular positions for the oscillation maxima/minima of order m and l , respectively. Moreover, the oscillation amplitudes provide information regarding the roughness of the corresponding layer, e.g., in imperfect surfaces/interfaces diffuse scattering of the x-ray beam decreases the measured intensity. Similarly to the XRD measurements, the XRR scans were collected in the Philips X'Pert Pro MPD diffractometer. In order to acquire the aforementioned information, the XRR scans are numerically fitted with the Parratt algorithm [100]. Since the reflection pattern is simulated by modeling the optical properties of the material, information about the composition is required. During the analysis the layer thickness, roughness, and mass density are fit parameters. As will be discussed later on in this thesis, the performance of functionable p-MTJs necessitates the precise estimation of the layer thickness and roughness. XRR method was employed to extract accurate sputter deposition rates and, thus, adjust the targets powers during the film deposition, by evaluating the XRR scans of several test samples.

The complex refractive index for monochromatic x-rays is given by the formula [98]

$$n = 1 - \sigma + i\beta, \quad (3.5)$$

where β concerns the absorption and σ the reflection coefficient, respectively, connected via the Kramers-Kronig relation. In x-rays, typical values for β and σ are in the range of 10^{-6} and 10^{-5} , respectively [101]. In comparison to XRD, XRR occurs in lower angles ($2\theta < 5^\circ$) in the Bragg-Brentano geometry, since the incoming the x-rays undergo total reflection when the incident angle is smaller than the critical one $\theta_c \approx \sqrt{2\sigma}$ (x-rays do not penetrate into the material). Above θ_c , the x-rays penetrate the sample and the reflectivity exponentially decays. By neglecting absorption ($\beta = 0$), one can extract that θ_c provides information about the density of the corresponding layer, hence being an element-specific parameter.

3.4 Magnetic analysis

To identify the magnetic properties of our samples, two different methods are utilized including direct measurement of the magnetization using the alternating gradient magnetometer (AGM) and other magnetic characteristics, e.g. coercivity, anisotropy field, squareness, etc, via the exploitation of Magneto-optic Kerr effect (MOKE). In the following subsections, we discuss the basic principles of the aforementioned techniques.

3.4.1 Alternating Gradient Magnetometer

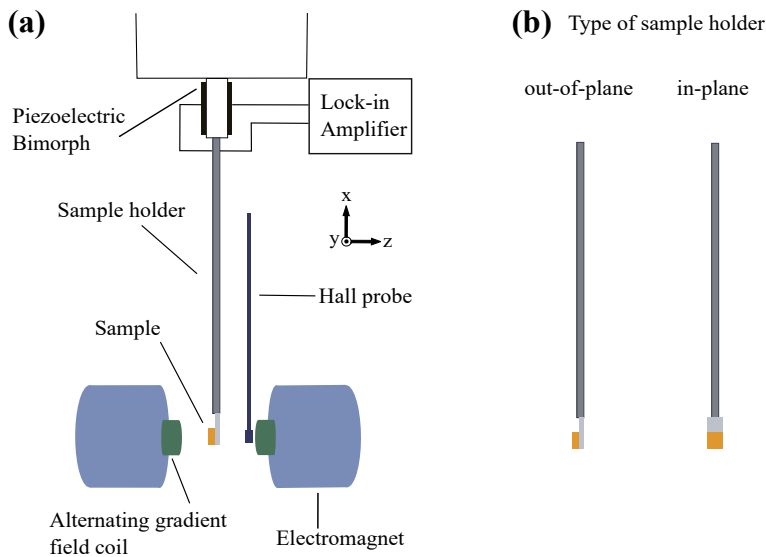


Figure 3.4. (a) Schematic illustration of alternating gradient magnetometer. (b) Type of sample holder used for the determination of magnetic characteristics in the out-of-plane and in-plane configurations.

The alternating gradient magnetometry concerns a fast and reliable method to extract the magnetization of a magnetic thin film. In this work we use a highly-sensitive (down to 10 nemu) and compact magnetic susceptibility measurement system, the Micromag 2900 AGM from Princeton Measurement Corporation. Figure 3.4(a) presents a schematic illustration of the AGM and the corresponding OOP/IP sample holder used to determine the magnetic

properties of the films are shown in Fig. 3.4(b). Initially, the sample is mounted on the end of a cantilever rod which incorporates a piezoelectric element and undergoes a dc magnetic field and a small alternating field gradient (ac field) stemming from the large and gradient electromagnetic coils, respectively. As a result the sample is magnetized and subjected to an alternating force, which is proportional to the magnitude of the field gradient and to the magnetic moment of the sample and is given by the equation

$$F_z = mB_z \frac{\partial b_z}{\partial Z}, \quad (3.6)$$

where m is the total magnetic moment, B_z is the magnetizing field strength, and b_z is the gradient field strength to the z direction. The application of an alternating force causes the cantilever rod with the sample to oscillate. If the frequency of vibration is tuned to a mechanical resonant frequency of the system (sample+cantilever rod), the amplitude of vibration increases by a factor equal to the quality factor Q of the vibrating system, which can be of the order of 100 [102]. The piezoelectric material converts the amplitude of the vibration to an electrical voltage which is proportional to the magnetic moment of the sample. The voltage output of the piezoelectric is detected and amplified by a lock-in amplifier.

3.4.2 Magneto-optic Kerr Effect

The magneto-optic Kerr effect (MOKE) was discovered in 1877 by John Kerr [103] in an attempt to characterize the interaction of light with a magnetic system. In particular, the polarization state of the reflected beam was changed when a plane-polarized incident beam shone on the surface of a horseshoe magnet.

Over the last decades, the utilization of MOKE as a characterization tool for the study of magnetism of thin films and multilayers regards a widely employed form of magnetometry. The high sensitivity of the technique to the magnetization within the skin depth region of metallic materials (10-20 nm), renders the effect a strong candidate for the study of surface magnetism. Furthermore, the technique provides the opportunity of the investigation of magnetic reversal processes in very small regions of materials or even in real micro-devices for applications. Moreover, the domain observation via Kerr

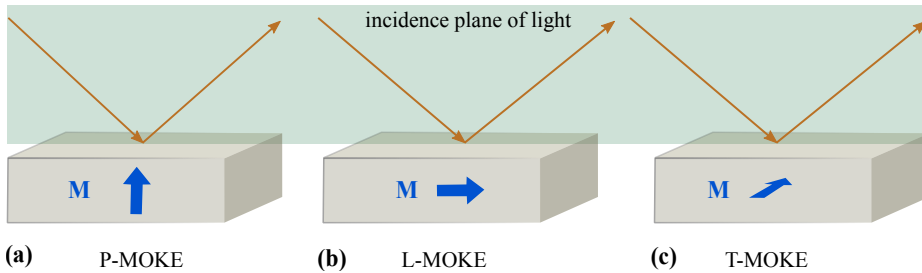


Figure 3.5. Schematic illustration of the three principal geometries of MOKE. Depending on the orientation of the magnetization \mathbf{M} with respect to the incidence plane of light and to the sample surface, we can distinguish between (a) P-MOKE, (b) L-MOKE, and (c) T-MOKE.

microscopes [104] provides a solid basis for the fundamental understanding of magnetization reversal processes on a surface of magnetic material. Apart from that, the working principle of the commercially magneto-optic drivers which are used nowadays is based on the Kerr effect.

In a next step, the MOKE basic principle as well as the setup geometries are analyzed. An incident linearly polarized light is modified after the reflection of a magnetized surface. Specifically, the polarization of the linear polarized light is transformed into elliptic and its polarization axis is rotated from the initial polarization. In a phenomenological approach, the linear polarized light can be treated as the sum of a right- and a left-handed circularly polarized wave of the same phase and amplitude. After their reflection from the magnetic surface in the right- and the left-hand circularly polarized light waves is induced a phase shift and their corresponding wave amplitudes become unequal. As a result, it is obtained a rotated and elliptically polarized wave. The three basic geometries which depend linearly on the respective magnetization components are the polar MOKE (P-MOKE), longitudinal MOKE (L-MOKE), and transversal MOKE (T-MOKE). In these geometries the Kerr effect results from the relative orientation of the magnetization direction with respect to the incidence plane of light and to the sample surface. In the P-MOKE geometry, the magnetization vector is perpendicular to the sample surface and parallel to the plane of incidence of light, as depicted in Fig. 3.5(a). Whereas, in L-MOKE case the magnetization is parallel to both the sample surface and the plane of incidence, as shown in Fig. 3.5(b). T-MOKE occurs when the

magnetization is parallel to the sample surface and perpendicular to the plane of incidence of light, as sketched in Fig. 3.5(c). In this thesis, the P-MOKE and L-MOKE geometries were utilized in order to determine the magnetic quantities such as H_C , H_{EB} , SQR, etc. of the probed stacks.

3.5 Chemical analysis

In order to determine the elements' interdiffusion in our p-MTJs, which can influence significantly the desired physical properties of the system, we performed Auger electron spectroscopy (AES) analysis. AES is a widely applied technique to extract information regarding the chemical composition of surfaces. The Auger effect concerns the core of this method and is schematically illustrated in Fig. 3.6. In particular, the ionization of an electron from an inner core shell due to external excitation (e.g. x-rays) is followed by the recombination process of the emerging hole with a second electron from an outer core shell. The released energy can be either emitted in a form of x-ray photon or transmitted to another electron and excite it from an outer shell. The aforementioned procedures concern two competitive phenomena, the x-ray fluorescence and Auger effect, respectively. X-ray fluorescence dominates in heavier elements whereas lighter elements prefer the emission of Auger electrons [105]. In addition, AES is rather surface sensitive technique and mainly probes the topmost few nm.

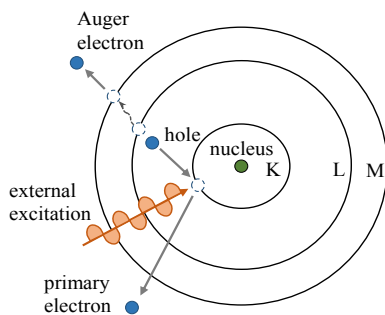


Figure 3.6. Schematic illustration of KLM Auger process in an atom.

The kinetic energy of the Auger electron is denoted by the difference in all three involved energy levels from low to high. Since the distance between

the energy levels is a fingerprint of each element, AES is an element specific method. As an example, considering the XYZ transition where X, Y, and Z denote the involved shells, the kinetic energies of the Auger electrons can be estimated by the formula

$$E_{XYZ} = E_X - E_Y - E_Z - U(YZ), \quad (3.7)$$

with E_X , E_Y , and E_Z as the energy of the X, Y, and Z electron, respectively. Furthermore, a correction term has to be added since the kinetic energy is influenced by the Coulomb interaction $U(YZ)$ of the generated holes. In order to obtain the AES depth profile of a multilayer stack, Ar ions are employed to etch the atomic layers sequentially. Further details regarding the technique can be found in Ref. [106].

Experimental

This chapter addresses results on the correlation of magnetic properties with the TMR ratio in Ta-capped p-MTJs with EB as well as on the influence of different capping layers on a number of magnetic quantities and the TMR ratio. In the first section, we demonstrate the establishment of the large PEB in MnIr-based stacks. We provide a detailed analysis of the magnetic properties of H_{EB} , H_{K} , H_{C} , M_{S} , and t_{DL} , pointing towards their tunable character by modifying the thickness of a CoFe/Ta thin layer between the MnIr and CoFeB films.

In the second section, we discuss the magnetic analysis of several trilayer CoFeB-based systems, capped with different materials (i.e. Ta, Hf, Zr, Mo). We extract the optimum parameters in terms of t_{CoFeB} and T_{ann} for the establishment of PMA in the individual films. Additionally, we make a thorough analysis of the several diffusion mechanisms which may occur in the investigated systems and determine the emergence of PMA.

The third section focuses on the dependence of several magnetic (i.e. H_{EB} , M_{S} , $t_{\text{FM}}^{\text{eff}}$, J) and magnetotransport properties (i.e. TMR ratio) on the F thickness of the soft electrode, T_{ann} , post annealing time, and t_{MgO} in Ta-capped p-MTJs with EB. In addition, the correlation of the TMR ratio with the magnetic properties is discussed.

The fourth section exhibits the influence of the magnetic properties and the TMR ratio from the introduction of several capping layers

with different degree of B absorption in the vicinity of the soft CoFeB electrode. In the fifth section we investigate the role of diffusion effects in two p-MTJs with EB capped with Ta and Hf, via performing Auger measurements. In the last section we probe the efficiency of the voltage-controlled magnetic anisotropy (VCMA) effect in Ta- and Hf-capped p-MTJs with EB via examining the electric field dependence of H_C . Most of the obtained results have been published in Refs. [107, 108].

4.1 Pinned electrode stacks based on MnIr/CoFe bilayers

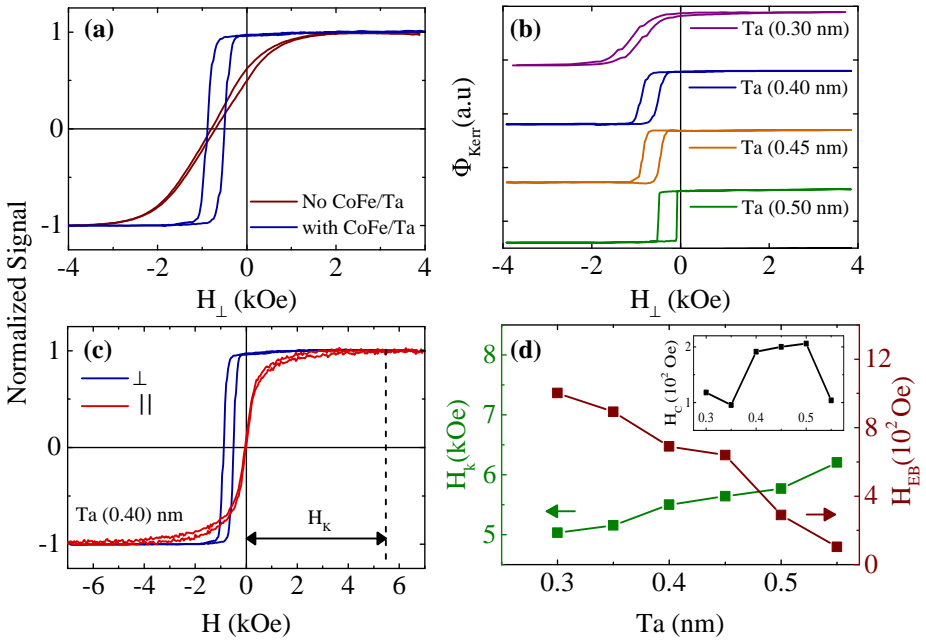


Figure 4.1. (a) OOP hysteresis loops of the samples Ta/Pd/MnIr/CoFe/Ta/CoFeB/MgO (blue) and Ta/Pd/MnIr/CoFeB/MgO (red). (b) OOP hysteresis loops for variable $t_{\text{Ta}}^{\text{int}}$. (c) Hysteresis loops in the OOP (blue) and IP (red) directions for the sample with $t_{\text{Ta}}^{\text{int}} = 0.40$ nm. (d) H_K (left-axis) and H_{EB} (right-axis) as a function of $t_{\text{Ta}}^{\text{int}}$. The inset shows the dependence of H_C on $t_{\text{Ta}}^{\text{int}}$.

Magnetic properties of MnIr-based stacks In Sec. 2.5, the necessity of the EB establishment in MTJs was analytically discussed by virtue of the enhancement of the retention time. From the magnetic standpoint, the fabrication of p-MTJs with EB involves two primary requirements. Firstly, the pinned electrode of the junction must display large EB along with low H_c , establishing a well defined plateau between the magnetic switching of the soft and pinned electrodes. In this way, the simultaneous switching of both electrodes can be prevented. Secondly, the soft and pinned electrode stacks should present high PMA to ensure a parallel (low resistance) or antiparallel (high resistance) relative orientation of the electrodes' magnetization in the perpendicular direction. The bottom part of the junction is preferred for the development of the pinned electrode, since MnIr acts as an additional seed layer that promotes the (111) texture of the subsequent F layer and, therefore, enables the establishment of higher PMA as van Dijken *et al.* reported [74].

In this thesis, the pinned electrode stack displaying large PEB and strong PMA is of the materials sequence Ta/Pd/MnIr/CoFe/Ta/CoFeB/MgO. In this stack, the presence of a CoFe/Ta dusting layer between MnIr and CoFeB plays a significant role in the satisfaction of the previously discussed magnetic criteria. Indicatively, in Fig. 4.1(a) two hysteresis loops in the OOP direction are shown for the stack Ta/Pd/MnIr/CoFe/Ta/CoFeB/MgO (blue) and Ta/Pd/MnIr/CoFeB/MgO (red). An EB field equal to 730 Oe with a reduced PMA at $H = 0$ Oe is visible for the stack without the CoFe/Ta dusting layer. On the contrary, the emergence of PEB with an $H_{EB} = 690$ Oe can be realized sustaining a strong PMA at $H = 0$ Oe for the series of stacks with the presence of CoFe/Ta interlayer.

Moreover, Fig. 4.1(b) depicts four representative hysteresis loops in the OOP direction for $t_{Ta}^{int} = 0.30$ nm (purple), $t_{Ta}^{int} = 0.40$ nm (blue), $t_{Ta}^{int} = 0.45$ nm (orange), $t_{Ta}^{int} = 0.50$ nm (green) where the tunable character of PEB as a function of the t_{Ta}^{int} is visible. Additionally, a substantial change of the hysteresis loop's shape can be extracted unveiling the significant influence of anisotropy while varying the t_{Ta}^{int} .

Figure 4.1(c) presents two hysteresis loops for the stacks with $t_{Ta}^{int} = 0.40$ nm recorded in the IP (red) and the OOP (blue) direction, collected via AGM. The establishment of an OOP easy axis is visible when comparing the relatively higher saturation field and lower remanent magnetization of the IP hysteresis loop compared to the OOP one. The H_K , is defined as the hard-axis saturation

field and measured at the intersection of the IP and OOP hysteresis loops, as indicated by the dashed line. From the OOP (IP) loops the behaviour of $H_{EB}(H_K)$ is extracted and plotted against t_{Ta}^{int} in Fig. 4.1 (d). An inverse relation between H_K and H_{EB} can be realized, presenting a monotonic decrease (increase) of $H_{EB}(H_K)$ from 103 Oe to 1003 Oe (5029 Oe to 6204 Oe), with increasing the t_{Ta}^{int} from 0.30 nm to 0.55 nm. Furthermore, from the OOP loops the H_C is identified for each stack and presented in the inset of Fig. 4.1(d) as a function of t_{Ta}^{int} . The stacks with $t_{Ta}^{int} = 0.40$ nm present a larger $H_C = 191$ Oe compared to $H_C = 118$ Oe for the stacks with $t_{Ta}^{int} = 0.30$ nm.

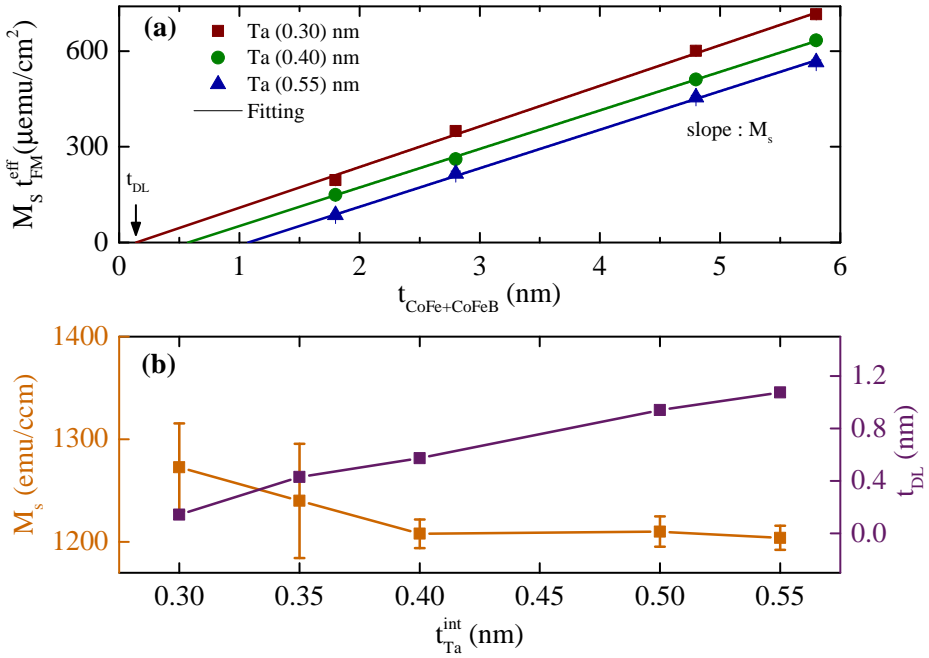


Figure 4.2. (a) $M_s t_{FM}^{eff}$ plotted against the total F thickness for the samples with $t_{Ta}^{int} = 0.30$ nm (red squares), $t_{Ta}^{int} = 0.40$ nm (green circles), $t_{Ta}^{int} = 0.55$ nm (blue triangles). The indicated lines represent the corresponding linear fits in which t_{DL} and M_s are determined by the intercepts and the slopes for each case, respectively. (b) The M_s (left-axis) and t_{DL} (right-axis) as a function of t_{Ta}^{int} .

In order to further elucidate the underlying mechanisms which contribute to the establishment of EB along with PMA, the M_s and t_{DL} have been determined in a series of stacks with variable t_{Ta}^{int} . Figure 4.2(a) illustrates the $M_s t_{FM}^{eff}$ as a

function of the F thickness with the corresponding linear fit for the sample series with $t_{\text{Ta}}^{\text{int}} = 0.30$ nm (red squares), $t_{\text{Ta}}^{\text{int}} = 0.40$ nm (green circles), and $t_{\text{Ta}}^{\text{int}} = 0.55$ nm (blue triangles). The dead layer thickness t_{DL} and the saturation magnetization M_s are estimated by the intercept of the linear fit with $M_s t_{\text{FM}}^{\text{eff}} = 0$ and the slopes of the curves, respectively. In addition, the determination of $t_{\text{FM}}^{\text{eff}}$ was performed via subtracting the t_{FM} with t_{DL} as discussed in subsec. 2.6.3. Figure 4.2(b) depicts the dependence of M_s (left-axis) and t_{DL} (right-axis) on $t_{\text{Ta}}^{\text{int}}$. The M_s shows a slight decrease for increasing $t_{\text{Ta}}^{\text{int}}$ and for $t_{\text{Ta}}^{\text{int}} \geq 0.4$ nm it remains constant displaying a value of 1210 emu/ccm. On the contrary, a monotonic increase of t_{DL} is observed with increasing $t_{\text{Ta}}^{\text{int}}$.

The observed behaviour of M_s could be explained through the existence of two competitive mechanisms in its final determination, as earlier discussed by Sinha *et al.* [109] in Ta/CoFeB/MgO layer systems. On the first hand, the determination of M_s depends on the amount of B located in the CoFeB electrode and, on the other hand, on the t_{DL} . The deficiency of B would enhance the crystallization of CoFeB and, thus, the resulting M_s . Whereas, the formation of t_{DL} would lead to the decrease of the determined M_s as visible from Fig. 4.2(b) for $t_{\text{Ta}}^{\text{int}} \geq 0.4$ nm. The domination of the one mechanism over the other dictates the final result. Consequently, the formation of the dead layer obscures the effect of B absorption for $t_{\text{Ta}}^{\text{int}} \geq 0.4$ nm, resulting in lower M_s values. Whereas, for $t_{\text{Ta}}^{\text{int}} < 0.4$ nm the M_s increases revealing that the mechanism of the dead layer formation is outweighed by the enhancement of B absorption.

Finally, the stacks with $t_{\text{Ta}}^{\text{int}} = 0.30$ nm and $t_{\text{Ta}}^{\text{int}} = 0.40$ nm are chosen to be the most suitable ones for the fabrication of the pinned part of the full p-MTJs. In the case of stacks with $t_{\text{Ta}}^{\text{int}} = 0.30$ nm, the considerably large $H_{\text{EB}} = 1000$ Oe is the characteristic which renders them promising candidate for their implementation in the pinned part. For stacks with $t_{\text{Ta}}^{\text{int}} = 0.40$ nm, although the exhibited H_{EB} equal to 690 Oe is smaller compared to the previous case, the obtained H_K equal to 5500 Oe is significantly larger compared to the previous ones (5000 Oe).

4.2 Soft electrode stacks based on CoFeB

4.2.1 Ta-capped soft electrode

In subsec. 2.3.2 we analyzed the mechanisms for the establishment of PMA in the underlayer/CoFeB/MgO systems concluding that 4d and 5d suitable candidate materials for the underlayer. As a next step, we investigated the T_{ann} and t_{CoFeB} dependencies on the following magnetic properties: squareness (SQR) defined as the ratio between the remanent (M_r) and the saturation magnetization, H_C , and $M_s t_{\text{FM}}^{\text{eff}}$ of the MgO/CoFeB/Ta/Pd layers system. We will thoroughly discuss the physical mechanisms which influence the establishment of PMA and we will extract the T_{ann} and t_{CoFeB} range where the PMA is obtained.

Figure 4.3(a) presents three indicative hysteresis curves collected under the application of OOP magnetic fields for MgO(2)/CoFeB(x)/Ta(3)/Pd(4) stacks, with $x = 1.05$ (blue), 1.20 (black), and 1.35 (red) nm, annealed at $T_{\text{ann}} = 280^\circ\text{C}$. In the sample with $t_{\text{CoFeB}} = 1.20$ nm the PMA is clearly observed and reflected by the large SQR exceeding 90%. On the contrary, the film with $t_{\text{CoFeB}} = 1.35$ nm shows IP anisotropy instead of PMA indicated by the poor SQR value around 10% and large $H_K \approx 4$ kOe. Interestingly, the stack with $t_{\text{CoFeB}} = 1.05$ nm presents a hysteresis free loop with the combination of a small saturation field ($H_\perp \approx 0.4$ kOe), a possible reason for this behaviour is a transition to a superparamagnetic state, i.e. that the magnetization switches thermally activated at a frequency much higher than the measurement time.

In Fig. 4.3(b) the evolution of H_C with the thickness of CoFeB is presented. Specifically, for $t_{\text{CoFeB}} \leq 1.05$ nm the H_C obtains constant values around 2 Oe, while in the thickness range $1.05 \text{ nm} \leq t_{\text{CoFeB}} \leq 1.20$ nm the H_C shows a constant increase with a maximum of 72 Oe. For $t_{\text{CoFeB}} > 1.25$ nm, a progressive decrease of H_C can be identified, bottoming out for $t_{\text{CoFeB}} = 1.50$ nm. Moreover, as illustrated in Fig. 4.3(c), which shows the SQR as a function of the F thickness, the magnetic anisotropy changes from perpendicular to IP for $t_{\text{CoFeB}} \geq 1.35$ nm, due to the increase of magnetostatic energy. In addition, the magnetic character becomes probably superparamagnetic (SM) for $t_{\text{CoFeB}} \leq 1.05$ nm. Thus, the thickness region which provides the establishment of PMA with SQR values around 0.9 is limited between 1.1 nm and 1.3 nm and drops abruptly at the boundary region.

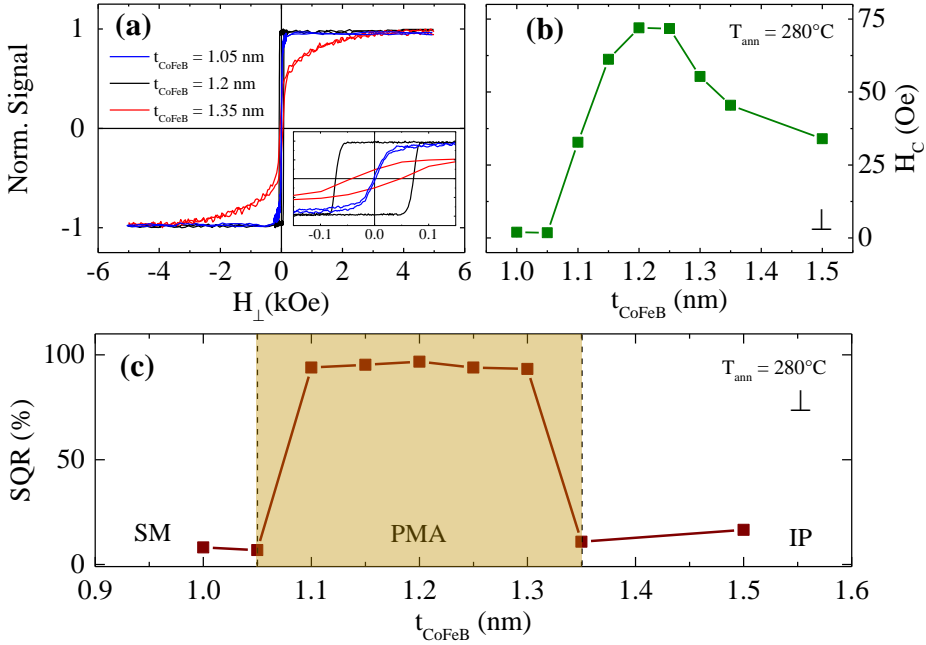


Figure 4.3. (a) OOP hysteresis loops of the MgO(2)/CoFeB(x)/Ta(3)/Pd(4) stacks with $x = 1.05, 1.20, 1.35$ nm annealed at $T_{\text{ann}} = 280^{\circ}\text{C}$ for 60 min. Inset: Close-up of the hysteresis loops around zero field. The magnetic properties of (b) H_C and (c) SQR ($\text{SQR} = \frac{M_r}{M_s}$) measured in the OOP direction are plotted against the CoFeB thickness. With yellow colour is indicated the thickness range of CoFeB in which the PMA is obtained. The superparamagnetic regime region is labelled as SM.

Figure 4.4(a) depicts three indicative hysteresis loops for the MgO(2)/CoFeB (1.2)/Ta(3)/Pd(4) stacks annealed at $T_{\text{ann}} = 280$ (black) $^{\circ}\text{C}$, 340 (red) $^{\circ}\text{C}$, 350 (blue) $^{\circ}\text{C}$. It is clearly observed that the stacks annealed at $T_{\text{ann}} \leq 340^{\circ}\text{C}$ acquire PMA, whereas for the stacks annealed at $T_{\text{ann}} = 350^{\circ}\text{C}$ the PMA disappears. From a series of hysteresis loops at several T_{ann} , we drew Fig. 4.4(b) which presents the dependence of SQR on T_{ann} . For $T_{\text{ann}} \leq 340^{\circ}\text{C}$, the samples exhibit almost constant SQR values around 90%, indicating the existence of PMA at this T_{ann} range. Further increase of T_{ann} ($T_{\text{ann}} \geq 350^{\circ}\text{C}$) causes a significant weakening of PMA which is reflected on the small SQR values of the order of 10%. Previous spectroscopic studies in Ta/CoFeB/MgO [110, 111] have correlated the Ta diffusion into the CoFeB layer with the emergence

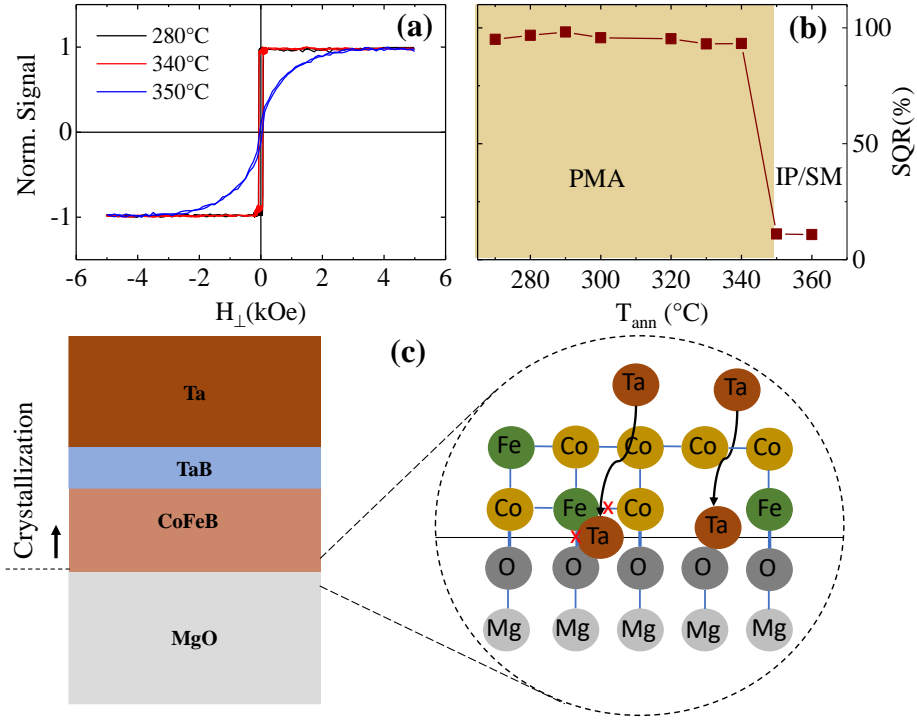


Figure 4.4. (a) OOP hysteresis loops of MgO(2)/CoFeB(1.20)/Ta(3)/Pd(4) stacks annealed at $T_{\text{ann}} = 280^\circ\text{C}$ (black), $T_{\text{ann}} = 340^\circ\text{C}$ (red), and $T_{\text{ann}} = 350^\circ\text{C}$ (blue). (b) The dependence of SQR on the T_{ann} for the MgO(2)/CoFeB(1.20)/Ta(3)/Pd(4) samples. With yellow colour is defined the T_{ann} region where PMA is well established. (c) Schematic illustration of the structure of MgO/CoFeB/Ta after annealing with the zoomed-in region of the CoFeB/MgO interface. The arrow indicates the crystallization orientation.

of PMA. Specifically, during the post-annealing treatment the as-prepared (A.P) amorphous CoFeB layer crystallizes in bcc (001) structure, coherently to the MgO (001) [112]. During this process, Ta acts as an efficient B absorber material, favouring the B out-diffusion and allowing for crystallization to occur. Simultaneously, the B atoms get stacked on the Ta/CoFeB interface creating a layer of TaB with thickness of $t_{\text{TaB}} \approx 0.2\text{ nm}$ [113]. However, the increase of T_{ann} causes the Ta diffusion into the CoFeB layer up to the CoFeB/MgO interface, which deteriorates the CoFeB (001) orientation, de-

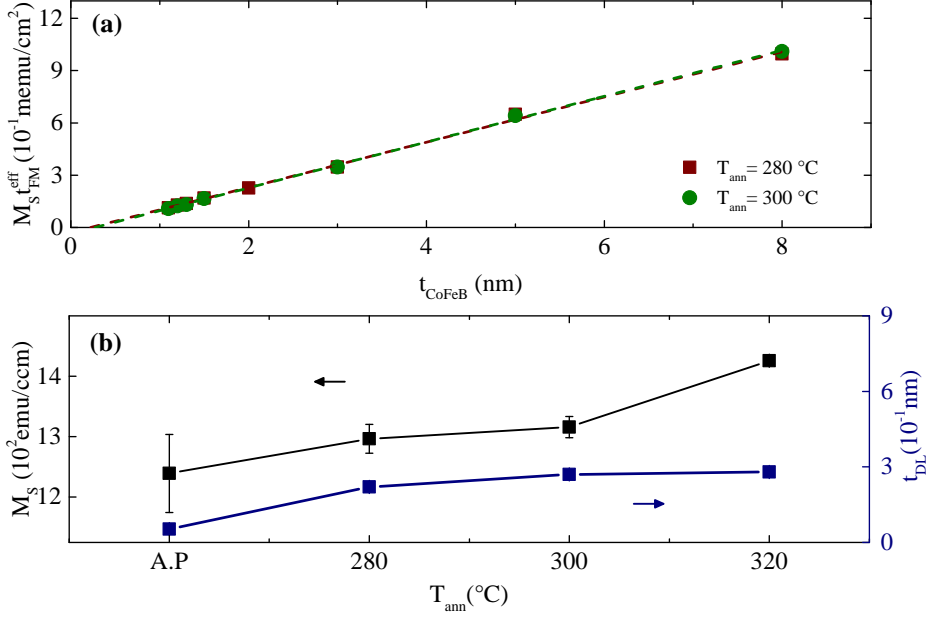


Figure 4.5. (a) Saturation magnetization per unit area plotted against the CoFeB thickness for the samples annealed at $T_{\text{ann}} = 280^\circ\text{C}$ (red) and $T_{\text{ann}} = 300^\circ\text{C}$ (green) along with the corresponding linear fits (dashed lines). (b) The saturation magnetization (left-axis) and magnetic dead layer thickness (right-axis) as a function of T_{ann} .

creases the CoFeB/MgO interface anisotropy, and finally destroys the PMA (cf. Fig. 4.4(c)).

Figure 4.5(a) presents the $M_s t_{\text{FM}}^{\text{eff}}$ plot as a function of t_{CoFeB} with the corresponding linear fits for the stacks MgO(2)/CoFeB(1.2)/Ta(3)/Pd(4) annealed at $T_{\text{ann}} = 280^\circ\text{C}$ (red) and $T_{\text{ann}} = 300^\circ\text{C}$ (green), respectively. From the corresponding slopes and the x-intercepts of the linear fits, we extracted the M_s (left-axis) and t_{DL} (right-axis) of the A.P and the annealed stacks, as shown in Fig. 4.5(b). It can be realized that the creation of a dead layer coincides with the beginning of the annealing process, showing $t_{\text{DL}} \approx 0$ in the A.P state. In the rest T_{ann} region, the dead layer ranges from $t_{\text{DL}} = 0.22$ nm to $t_{\text{DL}} = 0.28$ nm. Since $t_{\text{DL}} \approx t_{\text{TaB}}$, we can possibly attribute the existence of the magnetic dead layer to the formation of the TaB layer. Furthermore, the monotonic increase of M_s with T_{ann} underpins the enhancement of CoFeB

crystallization upon annealing. At this point, it is crucial to mention that the determination of the M_S and t_{DL} in trilayer systems (e.g. MgO/CoFeB/Ta) is of fundamental importance for their utilization as the soft electrodes in p-MTJs. Both parameters are inextricably linked with the determined TMR ratios and the establishment of thermally stable p-MTJs.

4.2.2 Alternative capping layers for the soft electrode

Apart from the use of Ta as a capping layer in the soft electrode, alternative materials could be utilized such as Mo, Hf, and Zr, which promote the establishment of PMA in such stacks and combine additional desirable properties for their implementation in p-MTJs. Particularly, Mo is valued to improve the thermal stability of the perpendicular CoFeB/MgO stacks, as Liu *et al.* [114] reported in their work. In addition, Hf and Zr are stronger B absorber materials compared to Ta and Mo and, thus, it is expected to enhance the TMR ratios in CoFeB/MgO/CoFeB based MTJs, as analyzed in subsec. 2.2.4.

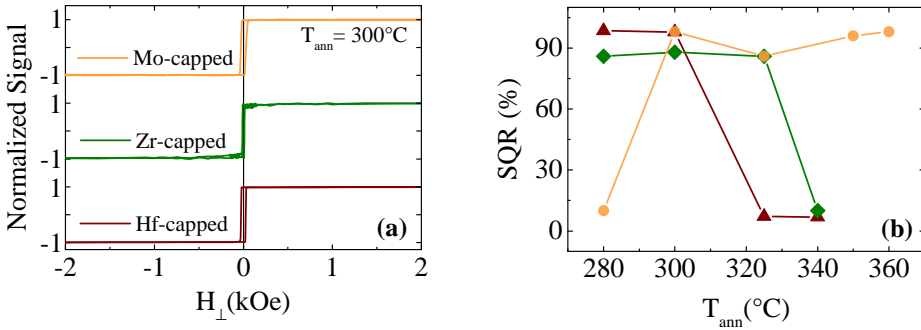


Figure 4.6. (a) OOP hysteresis loops of MgO(2)/CoFeB(1.2)/A/Pd(4), where A = Mo (orange), Zr (green), Hf (red) annealed at $T_{\text{ann}} = 300^\circ\text{C}$. (b) The T_{ann} dependence of SQR for Mo (orange)-, Zr (green)-, and Hf (red)-capped samples.

Figure 4.6(a) presents three hysteresis loops of the stacks MgO(2)/CoFeB(1.2)/A/Pd(4), with A = Mo (orange), Zr (green), Hf (red) annealed at $T_{\text{ann}} = 300^\circ\text{C}$ for 1h. From the hysteresis loops, we extracted the T_{ann} dependence of SQR for all samples with different capping layers, as presented in Fig. 4.6(b). For $T_{\text{ann}} > 325^\circ\text{C}$, the high (low) SQR values around 90% (10%) for the Mo-capped (Hf-, Zr- capped) samples can be pointed out indicating their high (low) thermal stability of PMA. On the contrary, at $T_{\text{ann}} = 280^\circ\text{C}$ the Hf-

and Zr-capped samples present high SQR values above 0.8, compared to the Mo-capped one which is identified around 0.1.

Since the establishment of PMA in trilayer stacks such as MgO/CoFeB/capping layer is determined to a certain extent by the interfacial PMA induced by the Fe–O hybrid orbital, it is necessary to examine the tendency of the capping layer to influence the aforementioned hybridization positively or negatively. In particular, two crucial parameters which are involved to the hybridization of Fe-O orbitals are related to the presence of B and the capping layer atoms in the interface of MgO/CoFeB, as it was previously discussed in subsec. 2.3.2.

Table 4.1. The predicted formation enthalpies in (kJ/mol) [115] of transition metal borides which may be anticipated within a typical half-MTJ structure.

M=	Ta	Mo	Hf	Zr
M ₂ B	-56	-35	-67	-72
MB	-78	-48	-95	-103
MB ₂	-74	-43	-95	-104

In Table 4.1 the formation enthalpies in (kJ/mol) of the transition metal borides M₂B, MB and MB₂ where M=Ta, Mo, Hf, and Zr are presented, as calculated by Niessen *et al.* [115]. The Ta-, Hf-, and Zr-capped samples exhibit significantly larger negative formation enthalpies compared to the Mo-capped ones, indicating the ability of the first ones to act as B absorber materials. As a result, we expect the establishment of PMA to take place at lower T_{ann} for the stronger B absorber materials compared to the weaker ones. As the T_{ann} increases, the interdiffusion of the elements is enhanced and, resultantly, the atoms of the capping layer reach the MgO/CoFeB interface weakening the hybridization of 3d Fe with 2p O orbitals, as previously indicated for the Ta-capped samples case.

However, this general mechanism seems to be more enhanced in the case of Ta-, Hf-, and Zr-capped samples compared to the Mo-capped ones, which can be identified by the observation of PMA at elevated T_{ann} for the latter case. This behaviour could be attributed to the lower interdiffusion of Mo compared to Ta, Hf, and Zr which can be realized by the significantly smaller negative formation enthalpies of the relevant oxides. Indicatively, the pre-

Table 4.2. Formation enthalpies in (kJ/mol) of Hf, Zr, Ta, and Mo oxides which may be anticipated in MgO/CoFeB interface.

A=	Hf	Zr	Mo	Ta
AO ₂	-1144.7	-1100.6	-588.9	-
AO ₃	-	-	-745.1	-
AO ₅	-	-	-	-2046.0

dicted formation enthalpies of Ta, Hf, Zr, and Mo oxides [116] that may be anticipated in the interface of MgO/CoFeB are summarized in Table 4.2. This underpins that Mo is much less diffusive material among the four, favouring the hybridization of Fe-O orbitals and, thus, promoting the thermal stability of PMA.

Since one core topic of this thesis focuses on the dependence of TMR ratio on the introduction of strong B absorber materials as capping layers in CoFeB-based p-MTJs, we will analyze the T_{ann} dependence of $M_S t_{\text{FM}}^{\text{eff}}$, M_S , and t_{DL} , for the Hf- and Zr-capped samples. Figure 4.7(a) illustrates the $M_S t_{\text{FM}}^{\text{eff}}$ as a function of the t_{CoFeB} for the Hf (red squares)- and Zr (green circles)-capped samples annealed at $T_{\text{ann}} = 280^\circ\text{C}$. Moreover, Figs. 4.7(b) and 4.7(c) depict the M_S and t_{DL} for the Hf-, Zr-, and Ta-capped samples, respectively. From Fig. 4.7(b), a trend of higher M_S values for stronger B absorber materials can be identified. Particularly, the stacks with the strongest B absorber material as a capping layer, i.e. Zr, present the highest M_S values for the entire T_{ann} range compared to their Hf- and Ta-capped counterparts. In a phenomenological approach, the stronger B absorption leads to the enhancement of the CoFeB crystallization, as previously analyzed, with a positive impact on the determined M_S values.

In addition, as shown in Fig. 4.7(c) the t_{DL} values of the Ta and Hf-capped stacks are comparable around 0.25 nm, whereas the t_{DL} values of the Zr ones are almost 0.12 nm. From the previously described physical picture for the creation of t_{DL} in MgO/CoFeB/Ta stacks, one should expect that Zr, as the strongest B absorber material, would form the thickest t_{DL} among the three series of stacks. However, it must be underlined that the origin of t_{DL} in such stacks does not only depend on the nature of the capping layer material,

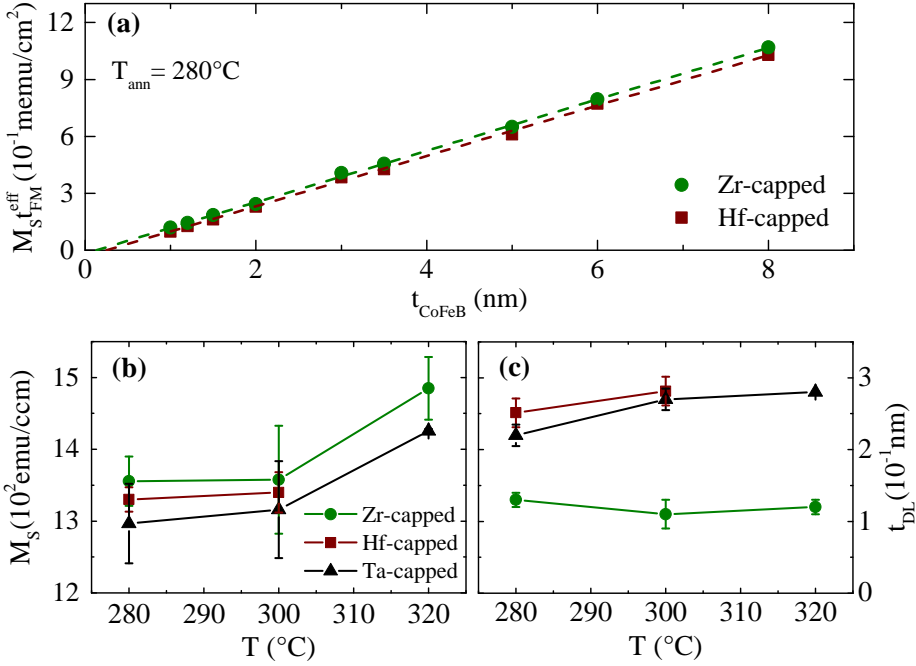


Figure 4.7. (a) $M_S t_{\text{FM}}^{\text{eff}}$ plotted against t_{CoFeB} for the stacks MgO(2)/CoFeB(x)/A(3)/Pd(4) where A = Zr (green), Hf (red) annealed at $T_{\text{ann}} = 280^\circ\text{C}$. The T_{ann} dependence of (b) M_S and (c) t_{DL} for the Zr (green circles)-, Hf (red squares)-, and Ta (black triangles)-capped samples.

but also on the precise control of the sputtering conditions [117], stack order, and base layer structure [118]. Consequently, the thinner t_{DL} observed in the Zr-capped stacks could be an outcome of possible changes in the sputtering conditions (e.g. Ar pressure), which would lead to smoother interfaces and, thus, smaller t_{DL} . For example, in literature a large variation of t_{DL} is reported for Ta/CoFeB/MgO stacks, ranging from 0 nm [114, 119] to 0.6 nm [109, 120].

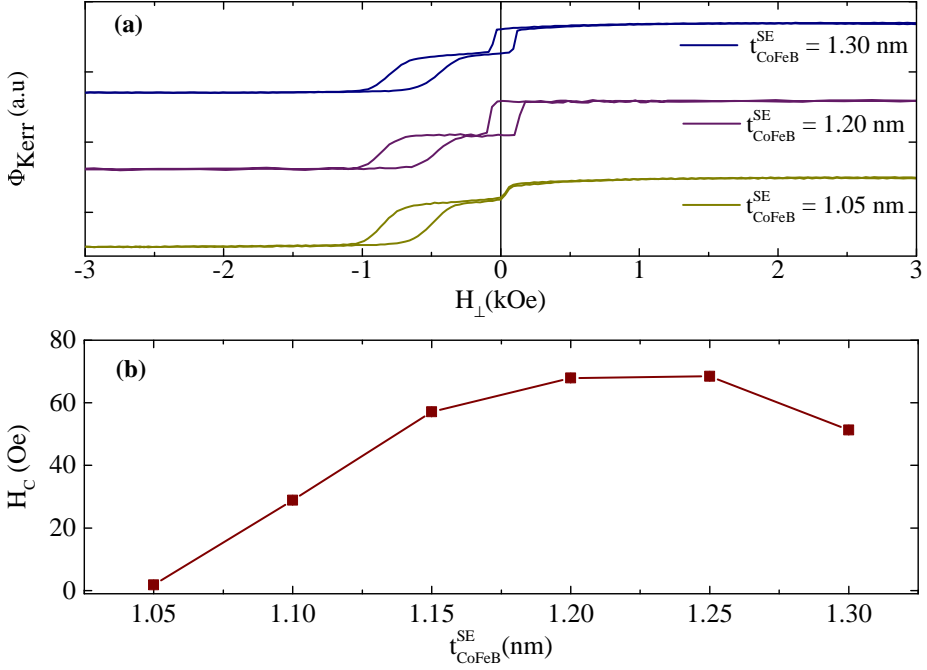


Figure 4.8. (a) Major hysteresis loops of sub/Ta(0.4)/CoFeB(0.8)/MgO(2)/CoFeB(x)/cap annealed at $T_{\text{ann}} = 280^\circ\text{C}$ for 60 min. (b) Coercivity measured in the OOP direction as a function of $t_{\text{CoFeB}}^{\text{SE}}$, acquired via MOKE.

4.3 Ta-capped p-MTJs with exchange bias

4.3.1 Magnetic properties

Figure 4.8 (a) illustrates three major hysteresis loops for the stacks sub/Ta(0.4)/CoFeB(0.8)/MgO(2)/CoFeB(x)/cap, with $t_{\text{CoFeB}}^{\text{SE}} = 1.05$ (yellow), 1.20 (purple), 1.30 (blue) nm. The layer stacks Ta(4)/Pd(2)/Mn₈₃Ir₁₇(8)/Co₅₀Fe₅₀(1) and Ta(3)/Pd(3) will be symbolized as “sub” and “cap”, respectively. The two distinct magnetic steps are clearly observed arising from the corresponding soft and pinned electrodes. However, no apparent hysteresis of the soft electrode for $t_{\text{CoFeB}}^{\text{SE}} = 1.05$ nm is observed while a hysteretic behaviour is evident for the rest samples with $t_{\text{CoFeB}}^{\text{SE}} = 1.20$ nm and $t_{\text{CoFeB}}^{\text{SE}} = 1.30$ nm. Figure 4.8(b) presents the H_C of the soft electrode as a function of $t_{\text{CoFeB}}^{\text{SE}}$, extracted from the minor loops (not shown). As visible, the H_C varies in

a range of (1.2 – 67.8) Oe reaching its maximum for $t_{\text{CoFeB}}^{\text{SE}} = 1.25$ nm and bottoming out for $t_{\text{CoFeB}}^{\text{SE}} = 1.05$ nm. Consequently, it can be pointed out that for $t_{\text{CoFeB}}^{\text{SE}} = 1.05$ nm the magnetic properties of the soft electrode illustrate the characteristics of superparamagnetism [121].

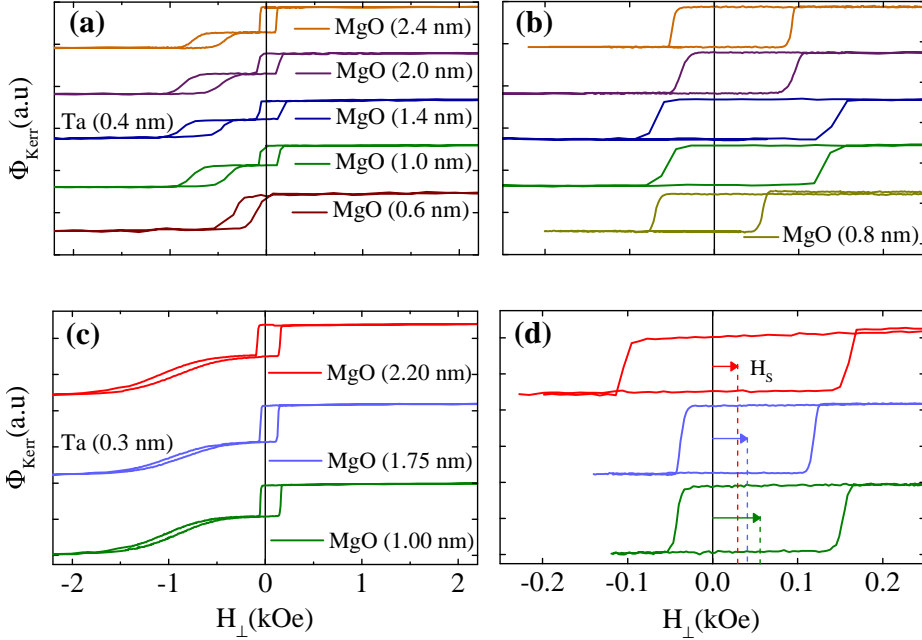


Figure 4.9. (a), (c) Major and (b), (d) minor loops of (a), (b) sub/Ta(0.4)/CoFeB(0.8)/MgO(x)/CoFeB(1.2)/cap and (c), (d) sub/Ta(0.3)/CoFeB(0.8)/MgO(x)/CoFeB(1.2)/cap stacks, after annealing at $T_{\text{ann}} = 280$ °C for 60 min, collected via MOKE.

Figure 4.9 shows a number of representative perpendicular major/minor hysteresis loops for the stacks sub/Ta(0.4)/CoFeB(0.8)/MgO(x)/CoFeB(1.2)/cap (cf. Figs. 4.9(a) and 4.9(b)) and sub/Ta(0.3)/CoFeB(0.8)/MgO(x)/CoFeB(1.2)/cap (cf. Figs. 4.9(c) and 4.9(d)), for $t_{\text{MgO}} = (0.6 - 2.4)$ nm. A noticeable difference between both series of stacks is the enhancement of H_{EB} from 640 Oe to 1000 Oe, as $t_{\text{Ta}}^{\text{int}}$ decreases. A possible explanation for the observed behaviour is that the decrease of $t_{\text{Ta}}^{\text{int}}$ from 0.4 nm to 0.3 nm causes a reduction in the number of Ta interlayer atoms which are deposited on MnIr through the pinholes of CoFe sublayer, leading to the increase of H_{EB} [71]. Alternatively,

the decrease of $t_{\text{Ta}}^{\text{int}}$ could lead to the enhancement of the direct coupling from the CoFeB to the CoFe and, thus, the increase of H_{EB} . Furthermore, as illustrated in Fig. 4.9(a), the two clear magnetic steps come closer to each other with decreasing t_{MgO} , while for $t_{\text{MgO}} = 0.6$ nm there is the formation of one magnetic step from the two initial.

Moreover, the magnetostatic character and strength are extracted following the methodology which is discussed in subsec. 2.6.3. As depicted in Figs. 4.9(b) and 4.9(d), the magnetostatic character is AF except for the stack with $t_{\text{MgO}} = 0.8$ nm (cf. Fig. 4.9(b)) where a change in the character of coupling takes place, due to the F nature of the direct coupling between the two electrodes [122]. Moritz *et al.* [83] suggested that in the case of films with strong PMA, the AF coupling can also be energetically favorable as an interplay of the magnetostatic, exchange, and anisotropy energy. In addition, the AF state between the electrodes denotes that we are in the beginning of the hole-formation in the MgO barrier. The contribution of the magnetic surface charges which is responsible for the F coupling may reduce, whereas the contribution of the magnetic volume charges promoting the AF coupling is enhanced. As a result, the finally determined coupling presents an AF nature. Additionally, in Figs. 4.9(b) and 4.9(d) a change of H_{C} is observed with the variation of t_{MgO} . This behaviour can be possibly attributed to the different roughness between the examined stacks induced by the change of t_{MgO} .

From the minor loops of the two series of stacks with $t_{\text{Ta}}^{\text{int}} = 0.4$ nm and $t_{\text{Ta}}^{\text{int}} = 0.3$ nm, J is acquired using Eq. (2.25). The calculated M_{s}^{SE} as well as t_{DL} for both samples are determined from a series of films where the thickness of CoFeB in the soft electrode varies.

Figure 4.10(a) depicts one indicative $M_{\text{s}} t_{\text{FM}}^{\text{eff}}$ loop acquired in the OOP direction for a stack with $t_{\text{Ta}}^{\text{int}} = 0.4$ nm, $t_{\text{MgO}} = 2.0$ nm, and $t_{\text{CoFeB}}^{\text{SE}} = 1.25$ nm, where the contributions of the soft and pinned electrodes in the $M_{\text{s}} t_{\text{FM}}^{\text{eff}}$ are indicated with double arrows. Figures 4.10(b) and 4.10(c) show the $M_{\text{s}} t_{\text{FM}}^{\text{eff}}$ as a function of t_{FM} for the stacks with $t_{\text{Ta}}^{\text{int}} = 0.4$ nm and $t_{\text{Ta}}^{\text{int}} = 0.3$ nm. The M_{s}^{SE} and t_{DL} for the sample with $t_{\text{Ta}}^{\text{int}} = 0.4$ nm ($t_{\text{Ta}}^{\text{int}} = 0.3$ nm) is extracted to be equal to $M_{\text{s}}^{\text{SE}} = (1166 \pm 45)$ emu/ccm ($M_{\text{s}}^{\text{SE}} = (1161 \pm 77)$ emu/ccm) and $t_{\text{DL}} = (0.53 \pm 0.05)$ nm ($t_{\text{DL}} = (0.53 \pm 0.05)$ nm).

The dependence of J on t_{MgO} for both stack series is illustrated in Fig. 4.10(d). As displayed in the graph, there is a strong dependence of J on the barrier thickness, with an AF (F) character for $t_{\text{MgO}} > 0.8$ nm ($t_{\text{MgO}} < 0.8$ nm),

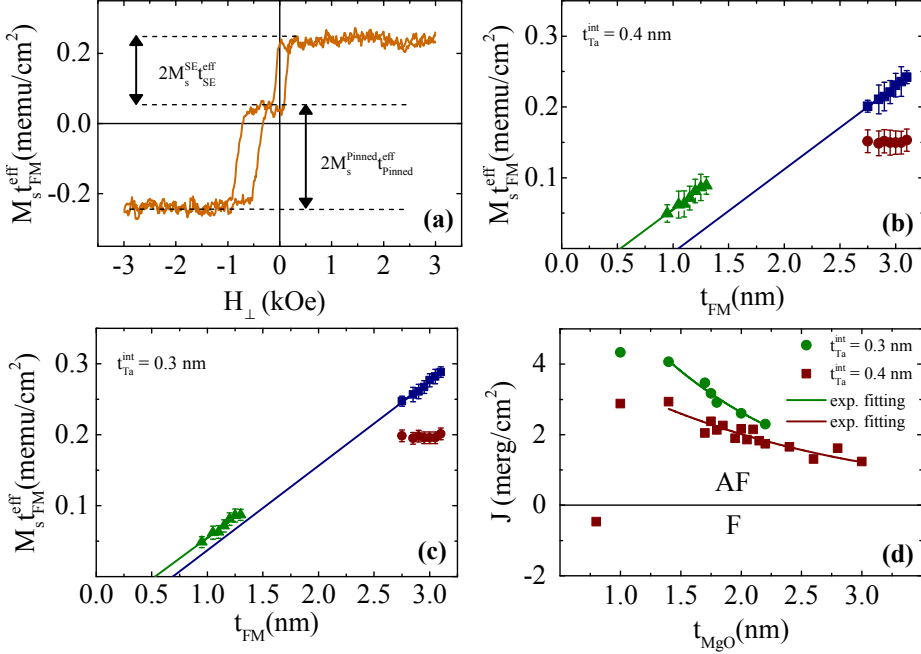


Figure 4.10. (a) The OOP $M_s t_{FM}^{eff}$ hysteresis loop of a stack with $t_{Ta}^{int} = 0.4$ nm, $t_{MgO} = 2.0$ nm, and $t_{CoFeB}^{SE} = 1.25$ nm. (b) ((c)) the $M_s t_{FM}^{eff}$ plotted against the total FM thickness for a stack with $t_{Ta}^{int} = 0.4$ nm ($t_{Ta}^{int} = 0.3$ nm). The points with blue, green, and red colour depict the $M_s t_{FM}^{eff}$, $M_s t_{SE}^{eff}$, and $M_s t_{Pinned}^{eff}$ along with the corresponding linear fits. (d) The dependence of J on t_{MgO} with $t_{Ta}^{int} = 0.4$ nm (red squares) and $t_{Ta}^{int} = 0.3$ nm (green circles) in the EB part. The green and red lines represent the corresponding linear fit arising from Néel model.

which is combined with an additional dependence on t_{Ta}^{int} . Specifically, the stacks with $t_{Ta}^{int} = 0.4$ nm show smaller values for J compared to the stacks with $t_{Ta}^{int} = 0.3$ nm. The higher J values of the stacks with $t_{Ta}^{int} = 0.3$ nm compared to the stacks with $t_{Ta}^{int} = 0.4$ nm, could be possibly attributed to their higher roughness [123]. According to Néel, the coupling strength could be represented by the exponential relation

$$J \propto \frac{\mu_0 M_s^2 h^2}{\lambda} \exp\left(-\frac{2\pi d}{\lambda}\right) = p \exp(-ad), \quad (4.1)$$

where d is the thickness of the spacer, h and λ is the amplitude and the wavelength of the correlated interface waviness of the insulating layer, respectively.

Consequently, $\frac{p}{a} \propto h^2$ which is a measure of roughness. In Fig. 4.10(d) the fitting functions for the stacks with $t_{\text{Ta}}^{\text{int}} = 0.3$ nm and $t_{\text{Ta}}^{\text{int}} = 0.4$ nm are indicated with green and red colour, respectively. From the ratio of the extracted parameters $\frac{p_{\text{Ta}(0.3)}}{a_{\text{Ta}(0.3)}} = \frac{12.75}{0.79} = 16.14 \text{ mA}^2 \text{ nm}^2$ and $\frac{p_{\text{Ta}(0.4)}}{a_{\text{Ta}(0.4)}} = \frac{4.76}{0.44} = 10.81 \text{ mA}^2 \text{ nm}^2$, we conclude that the samples with $t_{\text{Ta}}^{\text{int}} = 0.3$ nm acquire larger roughness values compared to the samples with $t_{\text{Ta}}^{\text{int}} = 0.4$ nm and, thus, present larger J values.

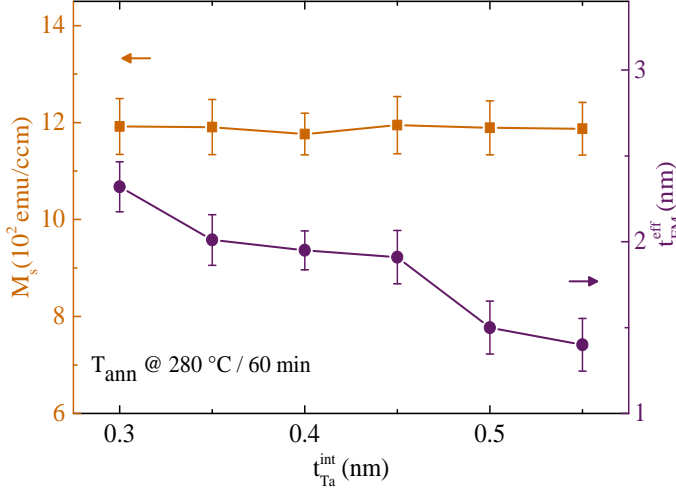


Figure 4.11. The dependence of M_s (left-axis) and $t_{\text{FM}}^{\text{eff}}$ (right-axis) on $t_{\text{Ta}}^{\text{int}}$.

Figure 4.11 depicts the dependence of M_s (left-axis), and $t_{\text{FM}}^{\text{eff}}$ (right-axis) of the total stack on $t_{\text{Ta}}^{\text{int}}$. The M_s and $t_{\text{FM}}^{\text{eff}}$ are obtained from a series of stacks with variable CoFeB thickness. An example of the estimation of M_s and t_{DL} for the sample with $t_{\text{Ta}}^{\text{int}} = 0.4$ nm annealed at $T_{\text{ann}} = 280^\circ\text{C}$ can be found in Fig. 4.13(a). As visible in Fig. 4.11 the M_s plot against $t_{\text{Ta}}^{\text{int}}$ presents a constant behaviour with increasing $t_{\text{Ta}}^{\text{int}}$, while the $t_{\text{FM}}^{\text{eff}}$ and $M_s t_{\text{FM}}^{\text{eff}}$ (not shown) decrease.

Figures 4.12(a) and 4.12(b) show a number of representative normalized major and minor loops for $t_{\text{MgO}} = 2$ nm and $t_{\text{Ta}}^{\text{int}} = 0.4$ nm at several T_{ann} , respectively. In particular, Fig. 4.12(a) demonstrates the loss of EB in the pinned part at $T_{\text{ann}} = 330^\circ\text{C}$. Figure 4.12(b) unveils the gradual reduction of H_s of the free layer with increasing T_{ann} . In both cases, the observed behaviour can be correlated with the increased interlayer diffusion effects during post-

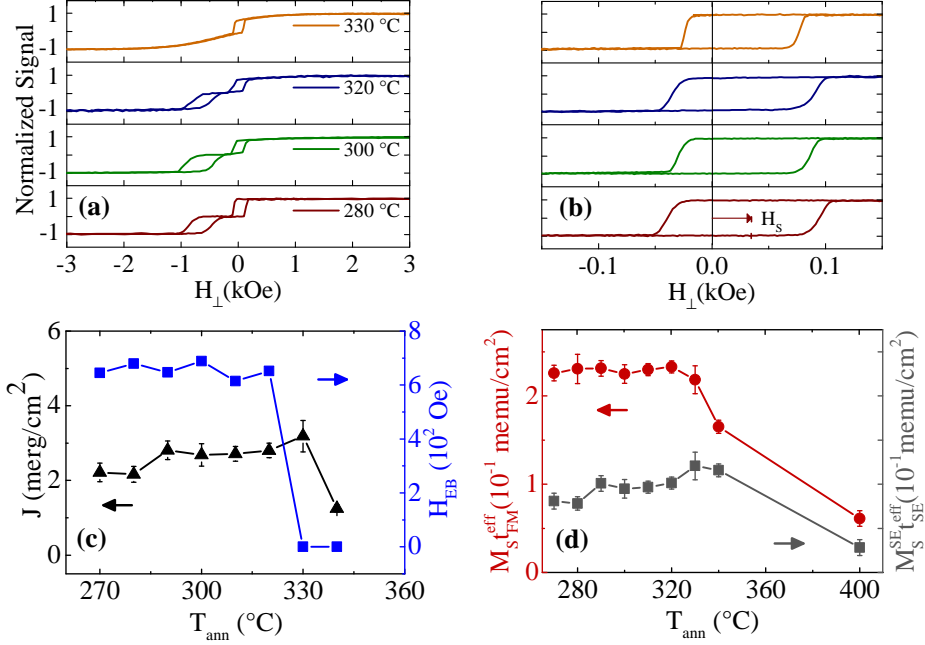


Figure 4.12. (a) Major and (b) minor normalized magnetic loops of stacks with $t_{\text{MgO}} = 2$ nm, $t_{\text{Ta}}^{\text{int}} = 0.4$ nm, and $t_{\text{CoFe+CoFeB}} = 3$ nm, for $T_{\text{ann}} = 280$ (red), 300 (green), 320 (blue), 330 (orange) °C. (c) The dependence of J (left-axis) and H_{EB} (right-axis) on T_{ann} . (d) The T_{ann} evolution of $M_s t_{\text{FM}}^{\text{eff}}$ and $M_s^{\text{SE}} t_{\text{SE}}^{\text{eff}}$ for a stack with $t_{\text{MgO}} = 2$ nm, $t_{\text{Ta}}^{\text{int}} = 0.4$ nm.

annealing, in line with previous reports for Ta/CoFeB/MgO layer systems [24, 111, 124, 125] and MnIr-based CoFeB/MgO/CoFeB MTJs [126].

Figures 4.12(c) and 4.12(d) illustrate the dependence of J , H_{EB} , $M_s t_{\text{FM}}^{\text{eff}}$, and $M_s^{\text{SE}} t_{\text{SE}}^{\text{eff}}$ on T_{ann} . From the minor and major loops, acquired via MOKE measurements at several T_{ann} , J and H_{EB} are calculated and presented as a function of T_{ann} in Fig. 4.12(c). As visible from the graph, the high T_{ann} causes a significant degradation of J (left-axis) and H_{EB} (right-axis) bottoming out at $T_{\text{ann}} = 340$ °C and $T_{\text{ann}} = 330$ °C, respectively. Similar temperature dependent behaviour of the coupling energy density was reported by Yakushiji *et al.* [127], in perpendicularly magnetized synthetic antiferromagnetically coupled reference structures.

Additionally, in Fig. 4.12(d) the $M_s t_{\text{FM}}^{\text{eff}}$ (left-axis) presents stable values for

$270^\circ\text{C} \leq T_{\text{ann}} \leq 330^\circ\text{C}$ noting a strong decrease for $T_{\text{ann}} \geq 340^\circ\text{C}$, reaching a low value at $T_{\text{ann}} = 400^\circ\text{C}$. Moreover, the $M_s^{\text{SE}} t_{\text{SE}}^{\text{eff}}$ (right-axis) illustrates a slight increase for $270^\circ\text{C} \leq T_{\text{ann}} \leq 340^\circ\text{C}$ noting a strong decrease for $T_{\text{ann}} = 400^\circ\text{C}$.

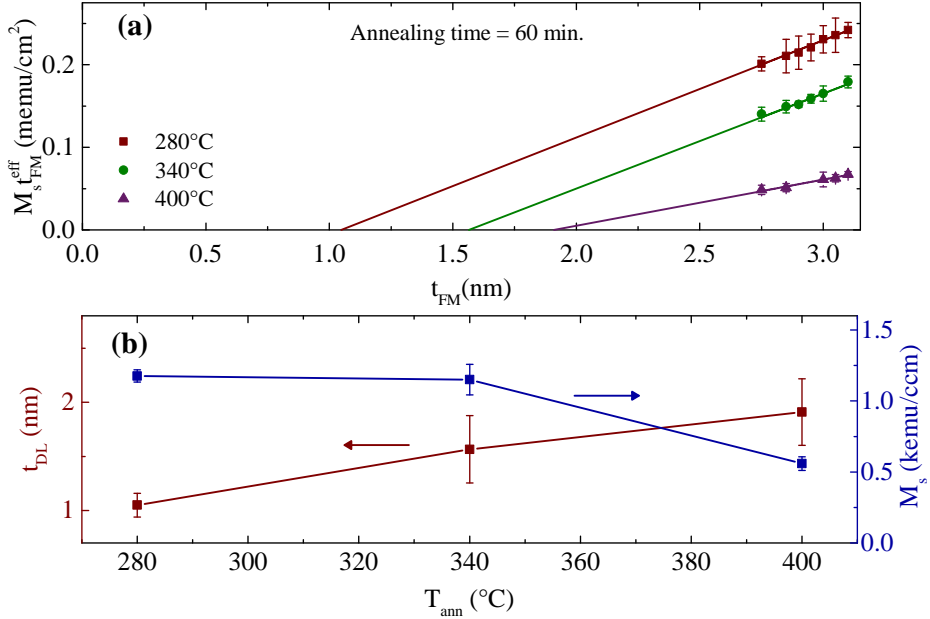


Figure 4.13. (a) Saturation magnetization per unit area $M_s t_{\text{FM}}^{\text{eff}}$ plotted against t_{FM} . (b) Magnetic dead layer thickness t_{DL} (left-axis) and saturation magnetization M_s (right-axis) as a function of the annealing temperature T_{ann} .

In order to further investigate the influence of diffusion effects on the magnetic properties of the stack, magnetic measurements are performed in a series of films with variable thickness of the top CoFeB, at various T_{ann} . Figure 4.13(a) illustrates the saturation magnetization per unit area $M_s t_{\text{FM}}^{\text{eff}}$ as a function of the F thickness with the corresponding linear fit for post-annealing temperatures equal to $T_{\text{ann}} = 280, 340, 400^\circ\text{C}$ for the sample series with $t_{\text{Ta}}^{\text{int}} = 0.4$ nm. In Fig. 4.13(b) the t_{DL} (left-axis) and M_s (right-axis) are presented for $T_{\text{ann}} = 280, 340, 400^\circ\text{C}$. Specifically, the M_s values are found to be equal to $M_s = (1176 \pm 43)$ emu/ccm for $T_{\text{ann}} = 280^\circ\text{C}$, $M_s = (1150 \pm 108)$ emu/ccm for $T_{\text{ann}} = 340^\circ\text{C}$, and $M_s = (559 \pm 48)$ emu/ccm for $T_{\text{ann}} = 400^\circ\text{C}$. Furthermore, the t_{DL} are extracted to be equal to $t_{\text{DL}} = (1.05 \pm 0.11)$ nm for $T_{\text{ann}} = 280^\circ\text{C}$,

$t_{\text{DL}} = (1.56 \pm 0.31) \text{ nm}$ for $T_{\text{ann}} = 340^\circ\text{C}$, and $t_{\text{DL}} = (1.91 \pm 0.30) \text{ nm}$ for $T_{\text{ann}} = 400^\circ\text{C}$. It is worth noting that the extracted values of t_{DL} correspond to the total F volume of the pinned and soft electrodes. These results are in line with previous publications [128], where M_s and t_{DL} present similar dependency on T_{ann} . Nonetheless, Jang *et al.* [129] reported an increase of M_s with increasing T_{ann} as a consequence of the enhanced crystallization of the CoFeB layer. As it was earlier analyzed in Sec. 4.1, in the determination of the parameter M_s two competitive mechanisms (i.e. B absorption, formation of dead layer) participate, which may lead to different results. Therefore, the observed behaviour of M_s with increasing T_{ann} could be an outcome of the dead layer formation which obscures the effect of B absorption, resulting in lower M_s values, as Sinha *et al.* [109] have reported in their work.

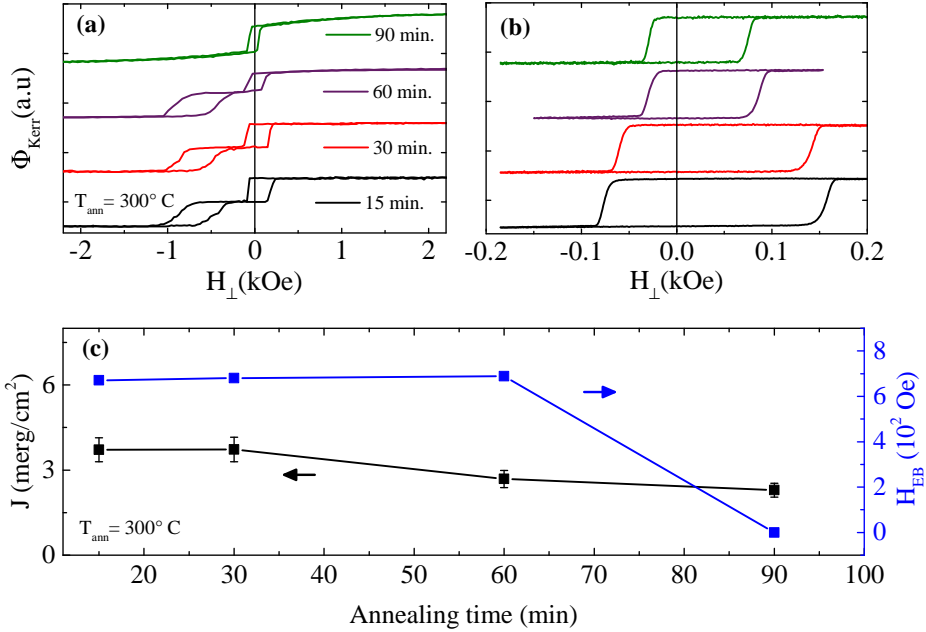


Figure 4.14. (a) Major and (b) minor normalized hysteresis loops of stacks with $t_{\text{MgO}} = 2 \text{ nm}$, $t_{\text{Ta}}^{\text{int}} = 0.4 \text{ nm}$, and $t_{\text{CoFe}+\text{CoFeB}} = 3 \text{ nm}$, for $T_{\text{ann}} = 300^\circ\text{C}$ and annealing time = 15 (black), 30 (red), 60 (purple), 90 (green) min. (c) The dependence of J (left-axis) and H_{EB} (right-axis) on annealing time for $T_{\text{ann}} = 300^\circ\text{C}$.

Furthermore, Figs. 4.14(a) and 4.14(b) show a number of representative normalized major and minor hysteresis loops for $t_{\text{MgO}} = 2 \text{ nm}$ and $t_{\text{Ta}}^{\text{int}} = 0.4 \text{ nm}$

at $T_{\text{ann}} = 300^\circ\text{C}$ and for several annealing times equal to 15 (black), 30 (red), 60 (purple), 90 (green) min, respectively. Specifically, from Fig. 4.14(a) the loss of EB in the pinned part can be extracted for the annealing time equal to 90 min. In addition, Fig. 4.14(b) illustrates the progressive reduction of H_s of the free layer with increasing the annealing time. Figure 4.14(c) shows the dependence of J (left-axis) and H_{EB} (right-axis) on the annealing time, extracted from the minor and major loops. As visible, the increase in annealing time causes a progressive degradation of J . On the contrary, the H_{EB} presents stable values for the annealing time range (15-60) min and disappears for annealing time equal to 90 min.

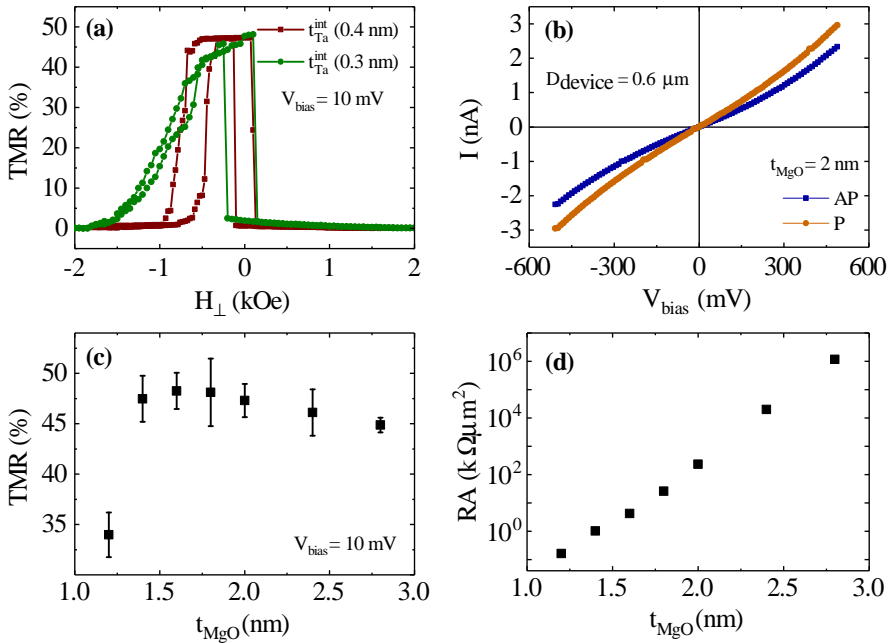


Figure 4.15. (a) Major TMR loops for the stacks with $t_{\text{MgO}}=1.8$ nm, $t_{\text{Ta}}^{\text{int}}=0.4$ nm (red), and $t_{\text{Ta}}^{\text{int}}=0.3$ nm (green) in the EB part. (b) I-V characteristics for the parallel (P-orange) and antiparallel (AP-blue) states of the stack with $t_{\text{MgO}}=2$ nm, $t_{\text{Ta}}^{\text{int}}=0.4$ nm, and $D_{\text{device}}=0.6$ μm . (c) TMR ratio values collected at RT with $V_{\text{bias}}=10$ mV plotted against t_{MgO} . (d) The resistance area product (RA) plotted against the MgO barrier thickness for samples with $t_{\text{Ta}}^{\text{int}}=0.4$ nm.

4.3.2 TMR properties

Figure 4.15(a) depicts two representative major TMR loops for a series of stacks with $t_{\text{Ta}}^{\text{int}} = 0.3$ nm (green) and $t_{\text{Ta}}^{\text{int}} = 0.4$ nm (red), for $t_{\text{MgO}} = 2$ nm at $V_{\text{bias}} = 10$ mV with $D_{\text{device}} = 0.6 \mu\text{m}$. In Fig. 4.15(b), the I-V curves of the stack with $t_{\text{MgO}} = 2$ nm and $t_{\text{Ta}}^{\text{int}} = 0.4$ nm are illustrated for the parallel (orange) and the antiparallel (blue) magnetic alignment of both electrodes. From a series of I-V curves for stacks with $t_{\text{MgO}} = (1.2 - 2.8)$ nm, the TMR ratio equal to $\text{TMR} = \frac{I_{\text{P}} - I_{\text{AP}}}{I_{\text{AP}}}$ can be extracted, where I_{P} (I_{AP}) is the current in the parallel (antiparallel) state. Figure 4.15(c) displays the averaged TMR ratio extracted from 8 devices at $V_{\text{bias}} = 10$ mV, acquired from the I-V curves, plotted against t_{MgO} with $D_{\text{device}} = 0.6 \mu\text{m}$. The TMR ratio increases with the t_{MgO} , reaching a saturation for $t_{\text{MgO}} \geq 1.4$ nm with a slight decrease for large t_{MgO} . In a phenomenological approach, the TMR ratio increase with t_{MgO} can be attributed to the increase of the tunnel probability for electrons with an off-normal incidence, which results in an increase of the effective polarization of the tunnel current and, therefore, the measured TMR ratio [8]. Nevertheless, for large t_{MgO} a decrease of TMR ratio has been reported [130] due to the significant contributions of the inelastic hopping and variable range hopping conductance mechanisms due to an increased number of defects in the barrier. Figure 4.15(d) presents the dependence of the resistance area product (RA) on the t_{MgO} for the samples with $t_{\text{Ta}}^{\text{int}} = 0.4$ nm.

Figure 4.16 illustrates the dependence of TMR ratio on the T_{ann} for annealing time equal to 60 min, annealing time for $T_{\text{ann}} = 300^\circ\text{C}$, and $t_{\text{CoFeB}}^{\text{SE}}$ extracted from the I-V characteristics, for the stacks with $t_{\text{MgO}} = 1.8$ nm, $t_{\text{Ta}}^{\text{int}} = 0.3$ nm (circles) and $t_{\text{MgO}} = 2$ nm, $t_{\text{Ta}}^{\text{int}} = 0.4$ nm (squares). Specifically, in Fig. 4.16(a) the TMR ratio initially increases with increasing the T_{ann} reaching a maximum of $(65.5 \pm 3.2)\%$ ($(65.5 \pm 0.5)\%$) at $T_{\text{ann}} = 300^\circ\text{C}$ for the sample series with $t_{\text{Ta}}^{\text{int}} = 0.3$ nm ($t_{\text{Ta}}^{\text{int}} = 0.4$ nm), presenting $H_{\text{EB}} = 1000$ Oe ($H_{\text{EB}} = 640$ Oe). At $T_{\text{ann}} = 320^\circ\text{C}$ there is a gradual decrease of TMR ratio to 60% possibly attributed to the presence of Mn atoms in the MgO barrier [126]. For $T_{\text{ann}} \geq 330^\circ$ a steep reduction of the TMR ratio can be observed. Moreover, a similar trend is presented in Fig. 4.16(b) with increasing TMR ratio for increasing the annealing time, peaking at 60 min and strongly decreasing at 90 min. The observed behaviours of increasing TMR ratio with increasing the T_{ann} and annealing time result from the crystallization of the amorphous CoFeB

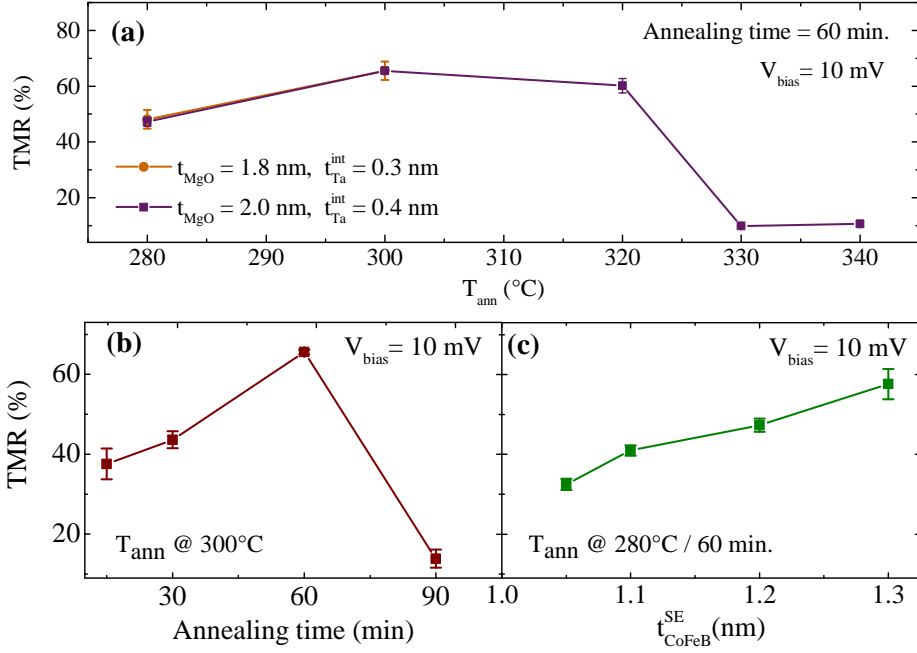


Figure 4.16. TMR ratio dependence on (a) T_{ann} , (b) annealing time, (c) $t_{\text{CoFeB}}^{\text{SE}}$ for the stacks having $D_{\text{device}} = 0.6 \mu\text{m}$ with $t_{\text{MgO}} = 1.8 \text{ nm}$, $t_{\text{Ta}}^{\text{int}} = 0.3 \text{ nm}$ (circles) and $t_{\text{MgO}} = 2 \text{ nm}$, $t_{\text{Ta}}^{\text{int}} = 0.4 \text{ nm}$ (squares).

electrodes and the improvement of crystalline structure of MgO (001) barrier [131].

Taking into account the T_{ann} and annealing time dependence of J , EB, TMR, and $M_s t_{\text{FM}}^{\text{eff}}$ (only T_{ann} dependence), the steep reduction of TMR ratio at $T_{\text{ann}} = 330^\circ\text{C}$ for 60 min and $T_{\text{ann}} = 300^\circ\text{C}$ for 90 min annealing time, coincides with the EB loss at these specific conditions. Therefore, among these three magnetic parameters the EB appears to have the most important influence on TMR. The EB loss leads to the lack of antiparallel configuration between the electrodes, which is necessary for the establishment of two well-defined resistance states. The aforementioned behaviour is also reported by Gan *et al.* [132] in CoFeB-based p-MTJs, where the lack of antiparallel configuration originates from the different temperature dependence of the H_c of the individual electrodes.

In Fig. 4.16(c) the monotonic increase of TMR ratio with increasing the

$t_{\text{CoFeB}}^{\text{SE}}$ can be extracted. Specifically, the TMR ratio is equal to $(32.5 \pm 1.4)\%$ for $t_{\text{CoFeB}}^{\text{SE}} = 1.05$ nm taking its highest value of $(57.6 \pm 3.8)\%$ for $t_{\text{CoFeB}}^{\text{SE}} = 1.30$ nm. The enhancement of the TMR ratio with increasing the $t_{\text{CoFeB}}^{\text{SE}}$ could be interpreted as an outcome of the enhanced spin polarization of the d[001] states as Yang *et al.* reported in their work [133]. As an example, in Fig. 4.8(a) for $t_{\text{CoFeB}}^{\text{SE}} = 1.05$ nm the soft electrode follows a superparamagnetic behaviour which results in a significant weakening of the effective spin polarization leading to small TMR ratio values.

4.4 Zr- and Hf-capped p-MTJs with exchange bias

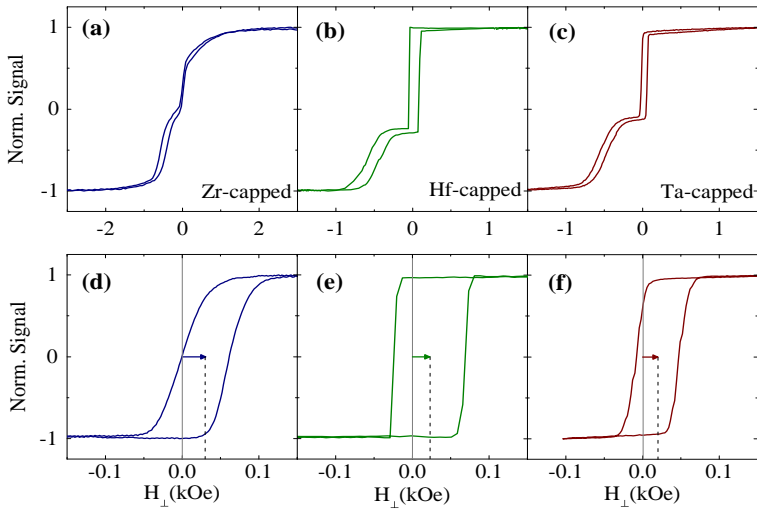


Figure 4.17. Normalized (a), (b), (c) major, (d), (e), (f) minor perpendicular (\perp) hysteresis loops of Zr (blue)-, Hf (red)-, and Ta (green)-capped films, respectively (MOKE at RT).

4.4.1 Magnetic properties

Figure 4.17 shows the OOP hysteresis loops of the stacks Ta/Pd/MnIr/CoFe/Ta/CoFeB/MgO/CoFeB/A/Pd where A=Zr (blue), Hf (red), and Ta (green), respectively, with the Ta interlayer thickness of 0.5 nm. The major loops are

presented in Figs. 4.17(a)-(c) while Figs. 4.17(d)-(f) illustrate the corresponding minor ones. In Figs. 4.17(a)-(c) two distinct magnetic steps are observable which correspond to the soft and the pinned electrode. The induced H_{EB} are smaller compared to the examined structures in Sec. 4.3 around -500 Oe, as a result of the slightly thicker $t_{Ta}^{int} = 0.50$ nm. Additionally, the direction of the H_{EB} is opposite to the applied field during annealing like in the previous case. Moreover, from the shift of the minor loops with respect to zero magnetic field, which are indicated in Figs. 4.17(d)-(f), we can extract the magnetostatic coupling strength and character (F or AF) by Eq. (2.25).

The calculated M_s as well as t_{DL} for all the samples are determined from a series of films where the thickness of CoFeB in the soft electrode varies. The M_s values for the soft electrodes of Zr-, Hf-, and Ta-capped samples are determined to be equal to $M_s = (1166 \pm 13)$ emu/ccm, $M_s = (1140 \pm 13)$ emu/ccm, and $M_s = (1121 \pm 13)$ emu/ccm, respectively, and presented in Fig. 4.18(a). The corresponding t_{DL} in the soft electrodes of Zr-, Hf-, and Ta-capped samples are extracted to be equal to $t_{DL} = 0.39$ nm, $t_{DL} = 0.56$ nm, and $t_{DL} = 0.52$ nm, respectively. The obtained values for the M_s are in good agreement with previous reports [134]. In addition, the magnetic shift for the Zr-, Hf-, and Ta-capped samples is identified to be equal $H_s = 30.5$ Oe, $H_s = 22$ Oe, and $H_s = 20$ Oe, respectively, and consequently J is extracted to be equal to $J = (2.87 \pm 0.10)$ merg/cm², $J = (1.60 \pm 0.10)$ merg/cm², and $J = (1.48 \pm 0.11)$ merg/cm², respectively as visible in Fig. 4.18(b). The positive value of J for all the samples reflects the AF character of coupling of both electrodes.

As analytically discussed in subsec. 2.6.2, the alignment of the magnetizations of two F layers separated by a non-magnetic spacer prefers such type of AF coupling when the PMA in the system is relatively large, which promotes the magnetic volume charges (MVC) to have a dominant contribution to the coupling between the two F layers.

A further characteristic to be pointed out is the difference between the PMA of the soft electrodes of all the samples. Figs. 4.18(c) and 4.18(d) show the anisotropy fields H_K and the uniaxial magnetic anisotropy energy density K_u , respectively. H_K corresponds to the minimum field strength applied perpendicular to the easy axis that is able to force the magnetization to become perpendicular to the easy axis. The K_u is calculated from Eq. (2.11) where

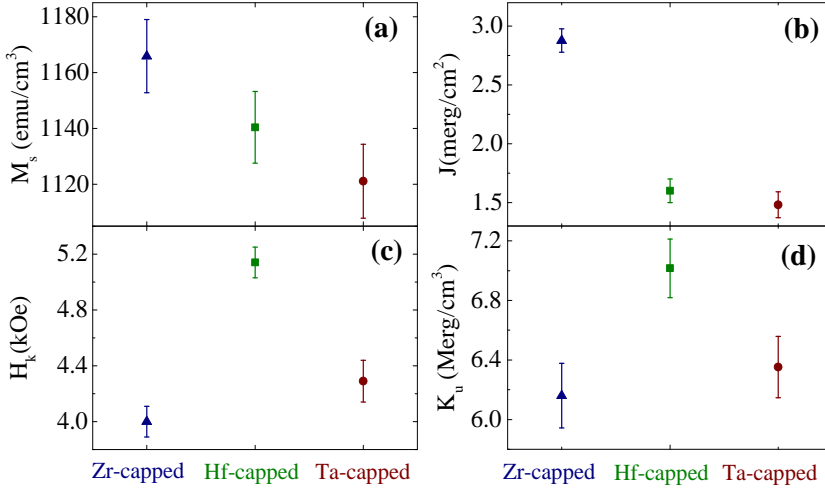


Figure 4.18. (a) Saturation magnetization (M_s), (b) coupling constant (J), (c) anisotropy field (H_K), and (d) uniaxial magnetic anisotropy energy K_u at RT, for the Zr (blue)-, Hf (red)-, and Ta (green)-capped films.

the term $\frac{K_s}{t_{\text{CoFeB}}}$ corresponds to the K_u for each sample and K_b is extracted to be negligible.

As depicted in Fig. 4.18(d), the Hf-capped samples present the largest values for K_u and H_K reflecting the significantly larger PMA of the soft electrode compared to the corresponding Zr- and Ta- capped ones. In turn, the Ta-capped samples present the second larger K_u and H_K values which are significantly higher than the corresponding Zr-capped ones. One would expect that since the largest B absorption among all the investigated capped samples is identified in the Zr-capped ones, this would lead to higher K_s values and, therefore, to higher H_K and K_u . However, the K_s term contains the sum of two contributions. The first one is K_{s_1} arising from the interface of CoFeB/A (where A=Hf, Ta, Zr) and the second one K_{s_2} results from the MgO/CoFeB interface. Therefore, the observed behaviour could be attributed to possible smaller K_{s_1} values for Zr-capped samples compared to the rest.

4.4.2 TMR properties

Figure 4.19 summarize the results of the TMR at RT for the Zr-, Hf-, Ta-capped samples, respectively. In Figs. 4.19(a)-(c) three representative major

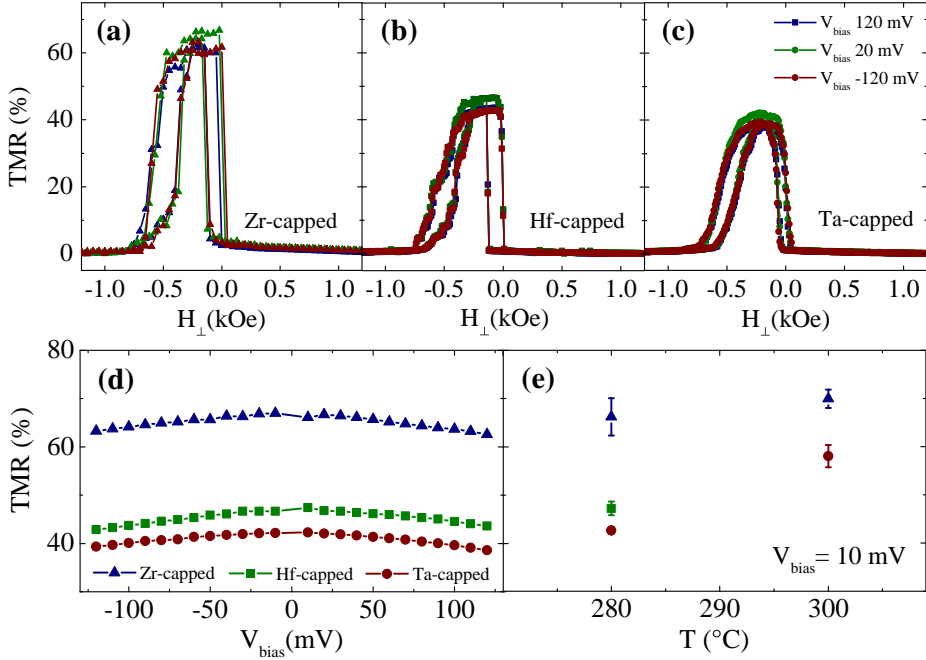


Figure 4.19. (a), (b), (c) Representative major TMR loops of the Zr (upper left)-, Hf (upper middle)-, and Ta (upper right)-capped samples for $V_{\text{bias}} = -120$ (red), 20 (green), 120 (blue) mV. (d) Bias dependence of TMR for Zr (blue)-, Hf (red)-, and Ta (green)-capped films. (e) Averaged TMR ratios of six contacts acquired at $V_{\text{bias}} = 10$ mV for Zr (blue)-, Hf (red)-, and Ta (green)-capped films.

TMR loops are displayed as a function of the perpendicular magnetic field for the Zr-, Hf-, and Ta-capped samples, respectively, acquired in different bias voltages ($V_{\text{bias}} = -120$ (red), 20 (green), 120 (blue) mV). From the I-V curves of six MTJs with $D_{\text{device}} = 0.6 \mu\text{m}$ and annealed at $T_{\text{ann}} = 280^\circ\text{C}$, we calculated the TMR ratios as illustrated in Fig. 4.19(d). It is clearly observed that the Zr-capped sample (blue triangles) possesses the highest TMR ratio compared to Hf-capped sample (green squares) and the Ta-capped one (red circles). Moreover, the averaged TMR ratios are presented in Fig. 4.19(e) for $V_{\text{bias}} = 10$ mV, for all samples at $T_{\text{ann}} = 280^\circ\text{C}$ and $T_{\text{ann}} = 300^\circ\text{C}$ (except from the Hf-capped). In particular, at $T_{\text{ann}} = 280^\circ\text{C}$ the TMR ratio are extracted to be equal to $(66.2 \pm 3.8)\%$, $(47.2 \pm 1.4)\%$, $(42.6 \pm 0.7)\%$ for the Zr-, Hf-, Ta-capped samples, respectively. In addition, at $T_{\text{ann}} = 300^\circ\text{C}$ the TMR ratio

are identified to be equal to $(69.9 \pm 1.9)\%$ and $(58.8 \pm 2.3)\%$ for the Zr- and Ta-capped sample, respectively. This is consistent with the claim of J. D. Burton *et al.* [33] that the presence of B at the CoFeB/MgO interface, suppresses the coherent tunneling in the Δ_1 band, leading to the reduction of TMR. Thus, preventing the presence of B at the interface should enhance the TMR in these junctions. Moreover, this is in agreement with the fact that Zr is the strongest B absorber material compared to Hf and Ta, which can be extracted by the formation enthalpies values as summarized in Table 4.1.

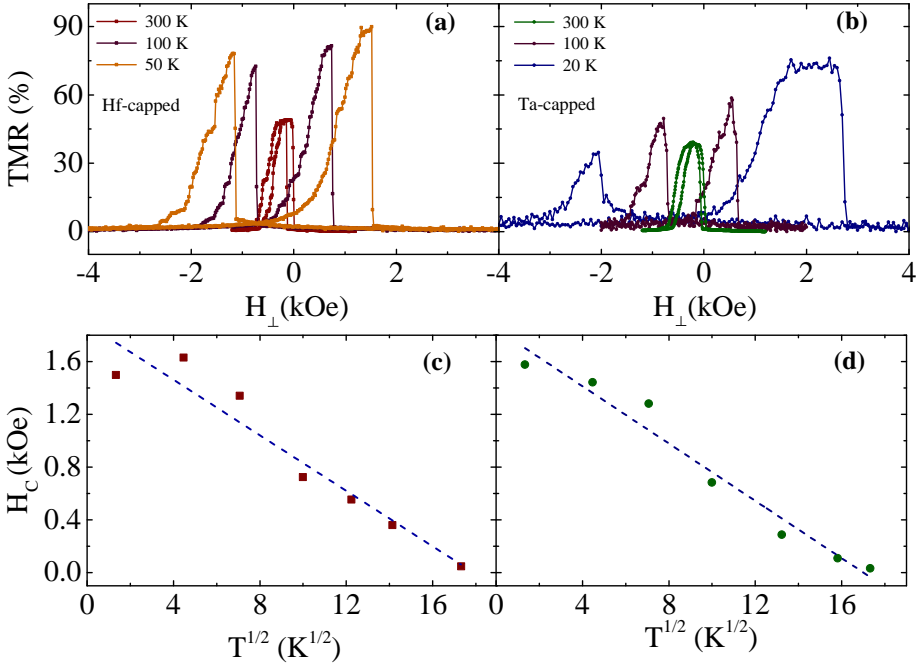


Figure 4.20. (a),(b) Major TMR loops of the Hf (upper left)- and (Ta) (upper right)-capped samples for $V_{\text{bias}} = 20$ (60) mV at $T = 50$ (20), 100 (100), 300 (300) K, respectively. (c), (d) H_c of the soft electrode versus $T^{1/2}$ (squares: experimental values, dashed line: model following Eq. (4.2) for the Hf (red)- and Ta (green)-capped films, respectively).

Figure 4.20(a) (Fig. 4.20(b)) presents the OOP TMR loops for Hf (Ta)-capped samples at different temperatures $T = 50$ (20), 100 (100), 300 (300) K for $V_{\text{bias}} = 20$ (60) mV, respectively. In Figs. 4.20(c) and 4.20(d) the H_c of the soft electrodes of the Hf- and Ta-capped samples, which were extracted from

the corresponding minor TMR loops (not shown), are plotted as a function of $T^{1/2}$. The temperature dependent behaviour of H_c for both samples can be described by Stoner-Wohlfarth model [50] under thermal fluctuations. In this model the temperature dependence of H_c is given by [135]

$$H_c = H_{c_0} \left[1 - \left(\frac{T}{T_B} \right)^{1/2} \right], \quad (4.2)$$

where T_B is the blocking temperature and H_{c_0} is the coercivity at 0 K. The extracted fitting parameters for the Hf (Ta)-capped sample is: $H_{c_0} = (1.88 \pm 0.14)$ kOe ($H_{c_0} = (1.84 \pm 0.10)$ kOe) and $T_B = 318.4$ K ($T_B = 289.2$ K). For both samples, the experimentally observed values for H_c are in reasonable agreement with the values predicted by Eq. (4.2). However, some slight deviations are observed especially at low temperatures. One reason could be the interaction of the soft electrode with the reference system that is also temperature dependent and prefers the antiparallel state, thereby adding an extra torque to the soft layers' magnetization. Another option is a magnetization reversal via domain wall nucleation and movement, that could induce an exponential dependence of H_c on T.

4.5 Auger measurements

As analyzed in Sec. 3.5, a versatile method to deliver a precise information regarding the diffusion mechanisms which take place in multilayer systems is AES. Thus, a possible stronger B absorption in the Hf-capped compared to the Ta-capped stacks which leads to the higher TMR ratios (see analysis subsec. 2.2.4), could be substantiated by AES measurements.

Figure 4.21 depicts the acquired AES sputter depth profile of the Hf- (upper) and Ta-capped (bottom) samples before (right) and after (left) annealing at 280°C. The Pd element is symbolized with red and B with black colour. The points of interest in both stacks are the soft electrodes (left parts of each figure), since these are the only parts which differ between both stacks and could be exclusively responsible for any changes in the determined TMR ratios. Particularly, a reduction of the B signal in the CoFeB/MgO interface is expected for the Hf-capped case compared to the Ta-capped one.

Moreover, the slight difference of Hf and Ta thicknesses (5 nm and 3 nm, respectively) could potentially result in an easier diffusion of Pd towards

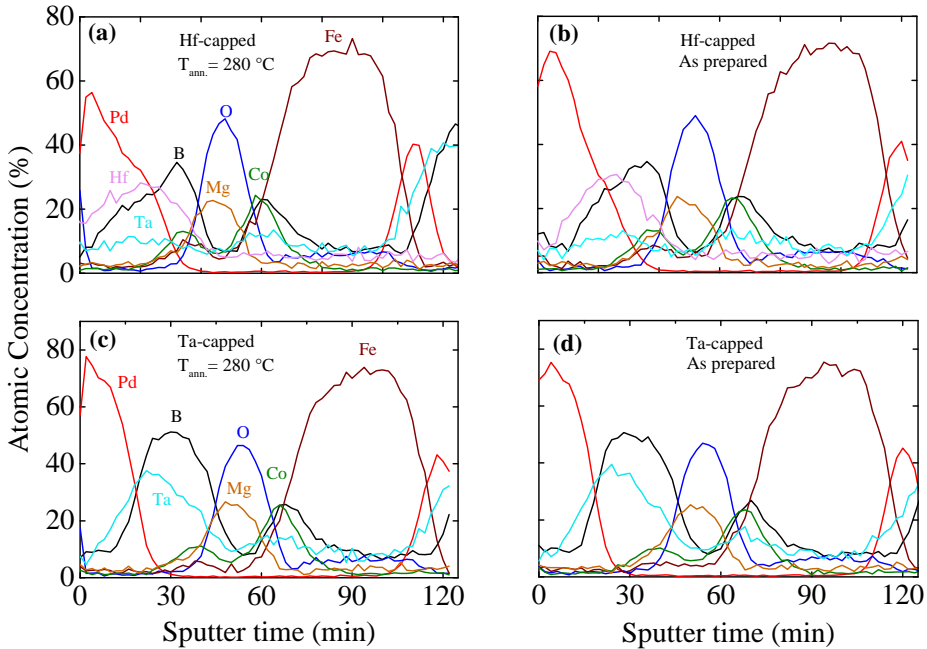


Figure 4.21. AES profiles of (a), (b) Hf- and (c), (d) Ta-capped samples. (a), (c) After post annealing at 280 °C. (b), (d) A.P samples.

the CoFeB/MgO interface in the Ta-capped case, which in turn would be observable with an enhancement of Pd signal. Comparing the AES depth profiles before and after annealing for both stacks, we find no evidence of diffusion of Pd in the stack which was created by the annealing procedure. Consequently, the TMR ratios are not influenced by the thickness difference of Hf- and Ta-capping layers. In a first glance, comparing the B signal in Hf-capped (cf. Fig. 4.21(a)) and Ta-capped stacks (cf. Fig. 4.21(c)) the concentration of B near the CoFeB/MgO interface seems to be higher in the latter case. However, this conclusion would be erroneous due to the physical limitation to distinguish between B and Ta atoms, since the kinetic energies of their Auger electrons are similar. Thus, a number of Ta electrons could parasitically contribute to the B signal.

4.6 Voltage Control Magnetic Anisotropy measurements

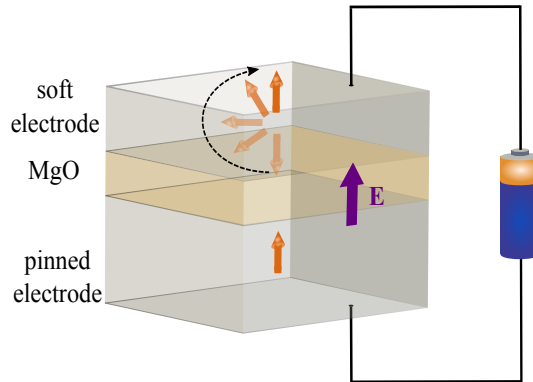


Figure 4.22. Schematic representation of electric-field assisted switching in a p-MTJ.

The VCMA effect plays a significant role in the field of voltage-controlled spintronic devices, since it provides the opportunity to modify the magnetic anisotropy of a MTJ via the application of an electric field [136]. In particular, in a p-MTJ structure as presented in Fig. 4.22 the application of an electric field can markedly alter the interfacial magnetic anisotropy to the extent that a voltage-induced resistance switching can be achieved. Phenomenologically, the most possible explanation of the VCMA effect mechanism is that the electric field modulates the charge distribution at the interface [137].

First principles studies have attributed the modification of magnetic anisotropy by an electric field to the change of the 3d-orbitals occupancies via spin-orbit interaction [138, 139]. From the applications aspect, the utilization of the VCMA effect offers a more energy-efficient route to manipulate the magnetization in MTJs, compared with the STT effect route [140]. Alzende *et al.*, reported one order of magnitude smaller switching energies from AP to P in CoFeB-based MTJs using the VCMA effect compared to the STT-based devices [136].

In our work, we performed a quantitative comparison of the VCMA effect magnitude in the stacks with material sequence Ta/Pd/MnIr/CoFe/Ta/CoFeB/MgO/CoFeB/X/Pd where X=Hf and Ta, via examining the electric field

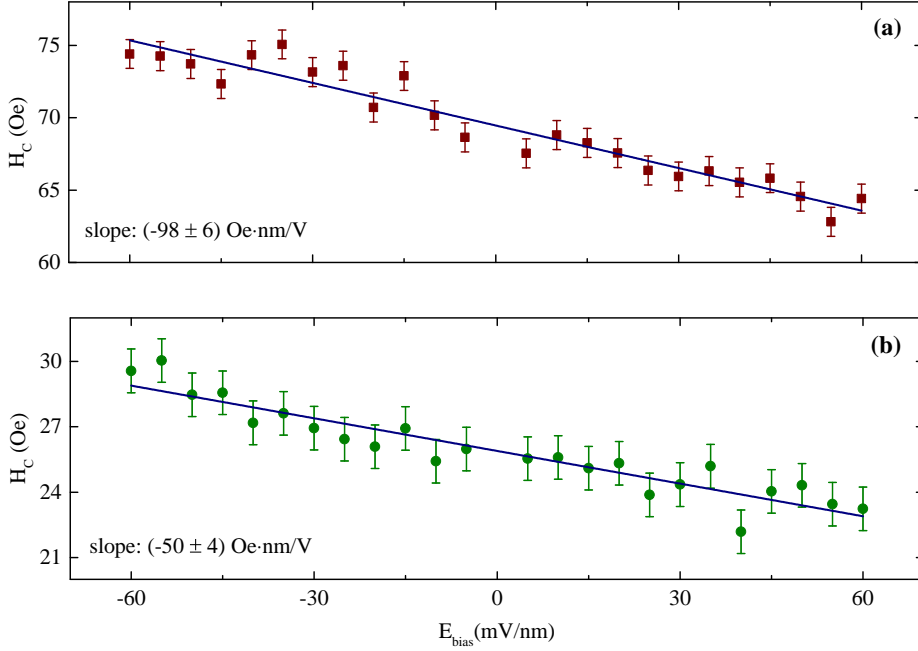


Figure 4.23. (a) Electric field dependence of the H_c of soft electrodes for (a) Hf- and (b) Ta-capped samples.

dependence of H_c , as illustrated in Fig. 4.23. The H_c is determined from the corresponding average TMR minor loops of 5 contacts collected under various electric fields. As shown, the application of a positive (negative) bias decreases (increases) the H_c of the soft electrode for both samples. A linear electric field dependence of H_c can be pointed out with a slope of (98 ± 6) Oe-nm/V ((50 ± 4) Oe-nm/V) for the Hf (Ta)-capped sample. It is worth mentioning that for the Hf-capped sample the slope is larger compared to the Ta-capped one, indicating a higher efficiency of the VCMA effect. Therefore, the Hf-capped p-MTJs which are investigated in this thesis might be of potential interest for VCMA-p-MTJ-based MRAM applications.

Summary & Outlook

MTJs are the key devices in modern spintronics with an exceptional place in the MRAM and sensor technology. In recent years, the p-MTJs have attracted major scientific interest as compared with their in-plane counterparts for a plethora of technological reasons. In this thesis we focused on the preparation and investigation of p-MTJs with EB utilizing a natural antiferromagnet (i.e. MnIr) on the pinned electrode for their potential implementation in MRAM and magnetic sensor devices. The applicability of these structures in both cases is inextricably connected with the magnitude of the TMR ratio and the underlying mechanisms which give rise to it. Consequently, a systematic investigation of the occurring physical mechanisms which influence the TMR ratio and its possible correlation with the magnetic properties in such systems, might offer valuable insight.

In a first step, we fabricated and investigated separately two sub-stacks for the soft and pinned electrodes, respectively, which composed the full p-MTJ stack. The soft electrode consisted of MgO/CoFeB/A/Pd films, where A=Ta, Hf, Zr, Mo are materials with different degree of B absorption, in which we varied the T_{ann} and the CoFeB thickness (only for Ta-capped). For the Ta-capped soft electrode the establishment of PMA was achieved for films with $1.1 \text{ nm} \leq t_{\text{CoFeB}} \leq 1.3 \text{ nm}$ and dropped abruptly at the boundary region. In addition, the magnetic properties showed the characteristics of superparamagnetism for $t_{\text{CoFeB}} \leq 1.05 \text{ nm}$. Moreover, a well established PMA was realized for the films with $270 \text{ }^\circ\text{C} \leq T_{\text{ann}} < 340 \text{ }^\circ\text{C}$. Further increase of T_{ann}

($T_{\text{ann}} \geq 350^\circ\text{C}$) caused significant weakening of PMA which was attributed to the migration of Ta atoms to the MgO/CoFeB interface.

Additionally, we studied the T_{ann} -behaviour of PMA for the Hf-, Zr-, and Mo-capped electrodes. For the case of Hf and Zr, the establishment of PMA showed a similar T_{ann} -behaviour (strong for low T_{ann} and weak for high T_{ann}) compared to the samples with Ta-capped electrode. Whereas, the PMA in samples with Mo presented the opposite behaviour (weak for low T_{ann} and strong for high T_{ann}). Thus, we extracted that the strong B absorption mechanism, which is dictated by Ta, Hf, Zr, compared to Mo, might be responsible for the establishment of PMA at low T_{ann} . For high T_{ann} , less diffusive capping materials (Mo) promoted the establishment of PMA.

The pinned electrode was composed of Ta/Pd/IrMn/CoFe/Ta/CoFeB/MgO materials stack in which we observed the modulation of the H_{EB} and the H_{K} with varying the $t_{\text{Ta}}^{\text{int}}$. We reported the establishment of large PEB and anisotropy field with values of $H_{\text{EB}} = 1000\text{ Oe}$, $H_{\text{K}} = 5000\text{ Oe}$ for $t_{\text{Ta}}^{\text{int}} = 0.3\text{ nm}$ and $H_{\text{EB}} = 690\text{ Oe}$, $H_{\text{K}} = 5500\text{ Oe}$ for $t_{\text{Ta}}^{\text{int}} = 0.4\text{ nm}$. In turn, we fabricated a series of p-MTJs with EB of materials sequence Ta/Pd/IrMn/CoFe/Ta/CoFeB/MgO/CoFeB/Ta/Pd where we systematically studied the correlation of magnetic properties with the measured TMR ratio. We observed the modulation of J , $M_s t_{\text{FM}}^{\text{eff}}$, H_{EB} from the parameters T_{ann} , annealing time, $t_{\text{Ta}}^{\text{int}}$ in the pinned electrode. In particular, after the variation of T_{ann} and annealing time we realized a TMR ratio in the range of (10 – 65.5)% noting its steep reduction at $T_{\text{ann}} = 330^\circ\text{C}$ for annealing time of 60 min and $T_{\text{ann}} = 300^\circ\text{C}$ for annealing time of 90 min. Comparing the T_{ann} and annealing time dependence of J , EB, TMR, and $M_s t_{\text{FM}}^{\text{eff}}$ (only T_{ann} dependence), we concluded that the loss of EB is the major factor for the large decrease of TMR ratio in the examined stacks. Controlling the TMR ratio by changing the magnetic properties in such stacks is of great interest for the magnetic field sensor industry.

Furthermore, we investigated the influence of B concentration in the MgO/CoFeB interface of the soft electrode on the magnetic and magneto-transport (TMR) properties. In particular, we fabricated and investigated three series of p-MTJs with EB stacks of materials sequence: Ta/Pd/IrMn/CoFe/Ta/CoFeB/MgO/CoFeB/Zr/Pd (stack 1), Ta/Pd/IrMn/CoFe/Ta/CoFeB/MgO/CoFeB/Hf/Pd (stack 2), Ta/Pd/IrMn/CoFe/Ta/CoFeB/MgO/CoFeB/Ta/Pd (stack 3). At $T_{\text{ann}} = 280^\circ\text{C}$ the TMR ratios were extracted to be equal to $(66.2 \pm 3.8)\%$, $(47.2 \pm 1.4)\%$ and $(42.6 \pm 0.7)\%$ for stack 1, stack 2, and stack

3, respectively. In addition, at $T_{\text{ann}} = 300^\circ\text{C}$ the TMR ratios were identified to be equal to $(69.9 \pm 1.9)\%$ and $(58.8 \pm 2.3)\%$ for stack 1 and stack 3, respectively. Thus, we concluded that the larger TMR values obtained for the Zr-capped compared to the Hf- and Ta-capped samples were attributed to the enhanced B absorption of Zr. The introduction of high B absorber materials in the soft electrode leads to the enhancement of TMR via preventing the suppression of conductance through the Δ_1 band.

In a next step, we probed the temperature dependence of the H_c of the soft electrodes for stacks 2 and 3 within the Stoner-Wolfram model. We observed a slight deviation from the model for both samples which was interpreted qualitatively by an additional torque from the interactions occurring between the AFM/FM double layer and the soft electrode. In turn, we investigated the efficiency of VCMA effect in stacks 2 and 3, via examining the electric field dependence of H_c of the soft electrodes. A linear electric field dependence of H_c was extracted with slopes of (98 ± 6) Oe·nm/V and (50 ± 4) Oe·nm/V for stack 2 and 3, respectively. Thus, a higher VCMA effect efficiency for the Hf-capped samples was identified compared to the Ta-capped ones. This result could render the proposed stacks as a candidate material for the realization of VCMA-based MRAMs.

Since one potential future deployment of the proposed p-MTJs could be in MRAM and sensor applications in which processing temperatures of 350°C or higher are required, the enhancement of thermal stability of the proposed stacks is of crucial importance. The limited thermal stability of the examined stacks is probably attributed to the diffusion of Ta interlayer and/or the Mn atoms in the pinned electrode. As a continuation of this thesis, a replacement of Ta interlayer with a series of different materials which provide strong PMA, low interdiffusion, and strong B absorption [141] or the replacement of MnIr with MnN/CoFe bilayers [142, 143], could potentially increase the thermal stability of the stack, maintaining sufficiently large EB.

So far, the thermally assisted MRAM has been realized for in-plane magnetized systems [144]. In such stacks, EB-films consisted of different AFMs are utilized for the pinned and soft electrodes, exhibiting sufficiently different blocking temperatures and EB fields [145]. One equally challenging issue of this work concerns the potential implementation of the proposed stacks for the realization of thermally-assisted MRAM in perpendicularly magnetized

systems. More specifically, the combination of the proposed MnIr-based stacks and Co/Pt synthetic AFM, could be highly desired.

Last but not least, a potential applicability of the proposed p-MTJ stacks could be focused on the field of magnetic sensor devices. However, it would be necessary to eliminate the role of the generated stray fields. Several techniques could be used to tackle that issue, either via trying to reduce the offset field directly from the reference electrode or via trying to introduce layers that counteract the fields emanating from the reference electrode.

Bibliography

- [1] J. W. Forrester, "Digital Information Storage in Three Dimensions Using Magnetic Cores", *J. Appl. Phys.* **22**, 44 (1951).
- [2] S. Tehrani, J. M. Slaughter, E. Chen, M. Durlam, J. Shi, and M. De-Herren, "Progress and outlook for MRAM technology", *IEEE Trans. Magn.* **35**, 2814 (1999).
- [3] M. Julliere, "Tunneling between ferromagnetic films", *Phys. Lett.* **54A**, 225 (1975).
- [4] W. H. Butler, X.-G. Zhang, T. C. Schulthess, and J. M. MacLaren, "Spin-dependent tunneling conductance of Fe|MgO|Fe sandwiches", *Phys. Rev. B* **63**, 054416 (2001).
- [5] J. Mathon and A. Umerski, "Theory of tunneling magnetoresistance of an epitaxial Fe/MgO/Fe(001) junction", *Phys. Rev. B* **63**, 220403 (2001).
- [6] X.-G. Zhang and W. H. Butler, "Large magnetoresistance in bcc Co/MgO/Co and FeCo/MgO/FeCo tunnel junctions", *Phys. Rev. B* **70**, 172407 (2004).
- [7] S. S. P. Parkin, C. Kaiser, A. Panchula, P. M. Rice, B. Hughes, M. Samant, and S.-H. Yang, "Giant tunnelling magnetoresistance at room temperature with MgO (100) tunnel barriers", *Nat. Mater.* **3**, 862 (2004).
- [8] S. Yuasa, T. Nagahama, A. Fukushima, Y. Suzuki, and K. Ando, "Giant room-temperature magnetoresistance in single-crystal Fe/MgO/Fe magnetic tunnel junctions", *Nat. Mater.* **3**, 868 (2004).

- [9] M. N. Baibich, J. M. Broto, A. Fert, F. N. Van Dau, F. Petroff, P. Etienne, G. Creuzet, A. Friederich, and J. Chazelas, “Giant Magnetoresistance of (001)Fe/(001)Cr Magnetic Superlattices”, *Phys. Rev. Lett.* **61**, 2472 (1988).
- [10] G. Binasch, P. Grünberg, F. Saurenbach, and W. Zinn, “Enhanced magnetoresistance in layered magnetic structures with antiferromagnetic interlayer exchange”, *Phys. Rev. B* **39**, 4828 (1989).
- [11] S. Mangin, D. Ravelosona, J. A. Katine, M. J. Carey, B. D. Terris, and E. E. Fullerton, “Current-induced magnetization reversal in nanopillars with perpendicular anisotropy”, *Nat. Mater.* **5** (2006).
- [12] T. Kishi, H. Yoda, T. Kai, T. Nagase, E. Kitagawa, M. Yoshikawa, K. Nishiyama, T. Daibou, M. Nagamine, M. Amano, S. Takahashi, M. Nakayama, N. Shimomura, H. Aikawa, S. Ikegawa, S. Yuasa, K. Y. ji, H. Kubota, A. Fukushima, M. Oogane, T. Miyazaki, and K. Ando, “Lower-current and fast switching of a perpendicular TMR for high speed and high density spin-transfer-torque MRAM”, *IEDM Tech. Dig.* **309-312** (2008).
- [13] O. G. Heinonen and D. V. Dimitrov, “Switching-current reduction in perpendicular-anisotropy spin torque magnetic tunnel junctions”, *J. Appl. Phys.* **108**, 014305 (2010).
- [14] S. S. P. Parkin, K. P. Roche, M. G. Samant, P. M. Rice, R. B. Beyers, R. E. Scheuerlein, E. J. O’Sullivan, S. L. Brown, J. Bucchigano, D. W. Abraham, Y. Lu, M. Rooks, P. L. Trouilloud, R. A. Wanner, and W. J. Gallagher, “Exchange-biased magnetic tunnel junctions and application to nonvolatile magnetic random access memory (invited)”, *J. Appl. Phys.* **85**, 5828 (1999).
- [15] K. N. Vyas, D. M. Love, A. Ionescu, J. Llandro, P. Kollu, T. Mitrelias, S. Holmes, and C. H. W. Barnes, “The Scanning TMR Microscope for Biosensor Applications”, *Biosensors* **5**, 172 (2015).
- [16] A. V. Silva, D. C. Leitao, J. Valadeiro, J. Amaral, P. P. Freitas, and S. Cardoso, “Linearization strategies for high sensitivity magnetoresistive sensors”, *Eur. Phys. J. Appl. Phys.* **72**, 10601 (2015).

-
- [17] Z. M. Zeng, P. Khalili Amiri, J. A. Katine, J. Langer, K. L. Wang, and H. W. Jiang, "Nanoscale magnetic tunnel junction sensors with perpendicular anisotropy sensing layer", *Appl. Phys. Lett.* **101**, 062412 (2012).
- [18] Y. Ding, J. H. Judy, and J.-P. Wang, "Magnetoresistive sensors with perpendicular magnetic anisotropy", *J. Appl. Phys.* **97**, 10N704 (2005).
- [19] S. van Dijken and J. M. D. Coey, "Magnetoresistance sensor with an out-of-plane magnetized sensing layer", *Appl. Phys. Lett.* **87**, 022504 (2005).
- [20] Y. Jang, C. Nam, J. Y. Kim, B. K. Cho, Y. J. Cho, and T. W. Kim, "Magnetic field sensing scheme using CoFeB/MgO/CoFeB tunneling junction with superparamagnetic CoFeB layer", *Appl. Phys. Lett.* **89**, 163119 (2006).
- [21] B. Dieny, R. Goldfarb, and K.-J. Lee, *Introduction to magnetic random-access memory* (IEEE press, WILEY, 2016).
- [22] T. Miyazaki and N. Tezuka, "Giant magnetic tunneling effect in Fe/Al₂O₃/Fe junction", *J. Magn. Magn. Mater.* **139**, L231 (1995).
- [23] J. S. Moodera, L. R. Kinder, T. M. Wong, and R. Meservey, "Large Magnetoresistance at Room Temperature in Ferromagnetic Thin Film Tunnel Junctions", *Phys. Rev. Lett.* **74**, 3273 (1995).
- [24] S. Ikeda, J. Hayakawa, Y. Ashizawa, Y. M. Lee, K. Miura, H. Hasegawa, M. Tsunoda, F. Matsukura, and H. Ohno, "Tunnel magnetoresistance of 604% at 300K by suppression of Ta diffusion in CoFeB/MgO/CoFeB pseudo-spin-valves annealed at high temperature", *Appl. Phys. Lett.* **93**, 082508 (2008).
- [25] H.-x. Liu, Y. Honda, T. Taira, K.-i. Matsuda, M. Arita, T. Uemura, and M. Yamamoto, "Giant tunneling magnetoresistance in epitaxial Co₂MnSi/MgO/Co₂MnSi magnetic tunnel junctions by half-metallicity of Co₂MnSi and coherent tunneling", *Appl. Phys. Lett.* **101**, 132418 (2012).

- [26] N. Tezuka, S. Oikawa, I. Abe, M. Matsuura, S. Sugimoto, K. Nishimura, and T. Seino, “Perpendicular Magnetic Tunnel Junctions With Low Resistance-Area Product: High Output Voltage and Bias Dependence of Magnetoresistance”, *IEEE Magn. Lett.* **7**, 1 (2016).
- [27] W. Skowronski, M. Czapkiewicz, S. Zietek, J. Chęcinski, M. Frankowski, P. Rzeszut, and J. Wrona, “Understanding stability diagram of perpendicular magnetic tunnel junctions”, *Sci. Rep.* **7**, 10172 (2017).
- [28] M. Wang, W. Cai, K. Cao, J. Zhou, J. Wrona, S. Peng, H. Yang, J. Wei, W. Kang, Y. Zhang, J. Langer, B. Ocker, A. Fert, and W. Zhao, “Current-induced magnetization switching in atom-thick tungsten engineered perpendicular magnetic tunnel junctions with large tunnel magnetoresistance”, *Nat. Commun.* **9**, 671 (2018).
- [29] J. C. Slonczewski, “Conductance and exchange coupling of two ferromagnets separated by a tunneling barrier”, *Phys. Rev. B* **39**, 6995 (1989).
- [30] S. Parkin, X. Jiang, C. Kaiser, A. Panchula, K. Roche, and M. Samant, “Magnetically engineered spintronic sensors and memory”, *Proc. IEEE* **91**, 661 (2003).
- [31] R. Meservey and P. Tedrow, “Spin-polarized electron tunneling”, *Phys. Rep.* **238**, 173 (1994).
- [32] X.-G. Zhang, W. H. Butler, and A. Bandyopadhyay, “Effects of the iron-oxide layer in Fe-FeO-MgO-Fe tunneling junctions”, *Phys. Rev. B* **68**, 092402 (2003).
- [33] J. D. Burton, S. S. Jaswal, E. Y. Tsybal, O. N. Mryasov, and O. G. Heinonen, “Atomic and electronic structure of the CoFeB/MgO interface from first principles”, *Appl. Phys. Lett.* **89**, 142507 (2006).
- [34] Néel, “Anisotropie magnétique superficielle et surstructures d’orientation”, *J. Phys. Radium* **15**, 225 (1954).
- [35] G.H.O. Daalderop, *Magnetic anisotropy from first principles*, in "*Ultra-thin Magnetic Structures I*, Springer Verlag, J.A.C. Bland and B.Heinrich Eds, Berlin, New York (1994).

- [36] H. X. Yang, M. Chshiev, B. Dieny, J. H. Lee, A. Manchon, and K. H. Shin, "First-principles investigation of the very large perpendicular magnetic anisotropy at Fe|MgO and Co|MgO interfaces", *Phys. Rev. B* **84**, 054401 (2011).
- [37] A. Manchon, C. Ducruet, L. Lombard, S. Auffret, B. Rodmacq, B. Dieny, S. Pizzini, J. Vogel, V. Uhlíř, M. Hochstrasser, and G. Panaccione, "Analysis of oxygen induced anisotropy crossover in Pt/Co/MO_x trilayers", *J. Appl. Phys.* **104**, 043914 (2008).
- [38] B. Rodmacq, A. Manchon, C. Ducruet, S. Auffret, and B. Dieny, "Influence of thermal annealing on the perpendicular magnetic anisotropy of Pt/Co/AlO_x trilayers", *Phys. Rev. B* **79**, 024423 (2009).
- [39] L. E. Nistor, B. Rodmacq, S. Auffret, and B. Dieny, "Pt/Co/oxide and oxide/Co/Pt electrodes for perpendicular magnetic tunnel junctions", *Appl. Phys. Lett.* **94**, 012512 (2009).
- [40] S. Ikeda, K. Miura, H. Yamamoto, K. Mizunuma, H. D. Gan, M. Endo, S. Kanai, J. Hayakawa, F. Matsukura, and H. Ohno, "A perpendicular anisotropy CoFeB-MgO magnetic tunnel junction", *Nat. Mater.* **9**, 721 (2010).
- [41] S. Monso, B. Rodmacq, S. Auffret, G. Casali, F. Fettar, B. Gilles, B. Dieny, and P. Boyer, "Crossover from in-plane to perpendicular anisotropy in Pt/CoFe/AlO_x sandwiches as a function of Al oxidation: A very accurate control of the oxidation of tunnel barriers", *Appl. Phys. Lett.* **80**, 4157 (2002).
- [42] B. Rodmacq, S. Auffret, B. Dieny, S. Monso, and P. Boyer, "Crossovers from in-plane to perpendicular anisotropy in magnetic tunnel junctions as a function of the barrier degree of oxidation", *J. Appl. Phys.* **93**, 7513 (2003).
- [43] F. J. A. den Broeder, D. Kuiper, H. C. Donkersloot, and W. Hoving, "A comparison of the magnetic anisotropy of [001] and [111] oriented Co/Pd Multilayers", *Appl. Phys. A* **49**, 507 (1989).
- [44] P. J. Chen, Y. L. Iunin, S. F. Cheng, and R. D. Shull, "Underlayer Effect on Perpendicular Magnetic Anisotropy in Co₂₀Fe₆₀B₂₀/MgO Films", *IEEE Transactions on Magnetics* **52**, 1 (2016).

- [45] W. H. Meiklejohn and C. P. Bean, “New magnetic anisotropy”, *Phys. Rev.* **105**, 904 (1957).
- [46] Néel, “Étude théorique du couplage ferro-antiferromagnétique dans les couches minces”, *Annales de Physique* **2**, 61 (1967).
- [47] D. Mauri, H. C. Siegmann, P. S. Bagus, and E. Kay, “Simple model for thin ferromagnetic films exchange coupled to an antiferromagnetic substrate”, *J. Appl. Phys.* **62**, 3047 (1987).
- [48] J. Nogués and I. K. Schuller, “Exchange bias”, *J. Magn. Magn. Mater.* **192**, 203 (1999).
- [49] E. C. Stoner and E. P. Wohlfarth, “Interpretation of high coercivity in ferromagnetic materials”, *Nature*, 160:650 (1947).
- [50] E. C. Stoner and E. P. Wohlfarth, “A mechanism of magnetic hysteresis in heterogeneous alloys”, *Philos. Trans. Royal Soc. A* **240**, 599 (1948).
- [51] W. H. Meiklejohn, “Exchange anisotropy—a review”, *J. Appl. Phys.* **33**, 1328 (1962).
- [52] C. Leighton, J. Nogués, H. Suhl, and I. K. Schuller, “Competing interfacial exchange and Zeeman energies in exchange biased bilayers”, *Phys. Rev. B* **60**, 12837 (1999).
- [53] I. V. Roshchin, O. Petravic, R. Morales, Z.-P. Li, X. Batlle, and I. K. Schuller, “Lateral length scales in exchange bias”, *EPL* **71**, 297 (2005).
- [54] J. Nogués, D. Lederman, T. J. Moran, and I. K. Schuller, “Positive Exchange Bias in FeF₂-Fe Bilayers”, *Phys. Rev. Lett.* **76**, 4624 (1996).
- [55] M. Kiwi, “Exchange bias theory”, *J. Magn. Magn. Mater.* **234**, 584 (2001).
- [56] J. Geshev, L. G. Pereira, and J. E. Schmidt, “Angular dependence of the exchange bias obtained from magnetization and ferromagnetic resonance measurements in exchange-coupled bilayers”, *Phys. Rev. B* **64**, 184411 (2001).
- [57] J.-V. Kim and R. L. Stamps, “Hysteresis from antiferromagnet domain-wall processes in exchange-biased systems: Magnetic defects and thermal effects”, *Phys. Rev. B* **71**, 094405 (2005).

-
- [58] A. P. Malozemoff, "Random-field model of exchange anisotropy at rough ferromagnetic-antiferromagnetic interfaces", *Phys. Rev. B* **35**, 3679 (1987).
- [59] A. P. Malozemoff, "Mechanisms of exchange anisotropy (invited)", *J. Appl. Phys.* **63**, 3874 (1988).
- [60] A. P. Malozemoff, "Heisenberg-to-Ising crossover in a random-field model with uniaxial anisotropy", *Phys. Rev. B* **37**, 7673 (1988).
- [61] J. Kouvel, "A Ferromagnetic-Antiferromagnetic Model for Copper-Manganese and related alloys", *J. Phys. Chem. Sol.* **24**, 795 (1963).
- [62] E. Fulcomer and S. H. Charap, "Thermal fluctuation aftereffect model for some systems with ferromagnetic-antiferromagnetic coupling", *J. Appl. Phys.* **43**, 4190 (1972).
- [63] M. D. Stiles and R. D. McMichael, "Model for exchange bias in polycrystalline ferromagnet-antiferromagnet bilayers", *Phys. Rev. B* **59**, 3722 (1999).
- [64] Nogués, J. and Sort, J. and Langlais, V. and Skumryev, V. and Suriñach, S. and Muñoz, J. S. and Baró, M. D., "Exchange bias in nanostructures", *Phys. Rep.* **422**, 65 (2005).
- [65] U. Nowak, A. Misra, and K. D. Usadel, "Domain state model for exchange bias", *J. Appl. Phys.* **89**, 7269 (2001).
- [66] A. Misra, U. Nowak, and K. D. Usadel, "Structure of domains in an exchange-bias model", *J. Appl. Phys.* **95**, 1357 (2004).
- [67] C. Mitsumata, A. Sakuma, and K. Fukamichi, "Mechanism of the exchange-bias field in ferromagnetic and antiferromagnetic bilayers", *Phys. Rev. B* **68**, 014437 (2003).
- [68] N. C. Koon, "Calculations of Exchange Bias in Thin Films with Ferromagnetic/Antiferromagnetic Interfaces", *Phys. Rev. Lett.* **78**, 4865 (1997).
- [69] D. Suess, M. Kirschner, T. Schrefl, J. Fidler, R. L. Stamps, and J.-V. Kim, "Exchange bias of polycrystalline antiferromagnets with perfectly compensated interfaces", *Phys. Rev. B* **67**, 054419 (2003).

- [70] X. Illa, E. Vives, and A. Planes, “Metastable random-field Ising model with exchange enhancement: A simple model for exchange bias”, *Phys. Rev. B* **66**, 224422 (2002).
- [71] X. Zhang, Y. Zhang, and J. W. Cai, “Large Perpendicular Exchange Bias in CoFeB/MgO Systems Pinned by a Bottom IrMn Layer via an Interfacial CoFe/Ta Composite Layer”, *IEEE Trans. Magn.* **51**, 4800604 (2015).
- [72] H. Tong, C. Qian, L. Miloslavsky, S. Funada, X. Shi, F. Liu, and S. Dey, “Studies on antiferromagnetic/ferromagnetic interfaces”, *J. Magn. Magn. Mater.* **209**, 56 (2000).
- [73] N. P. Aley, G. Vallejo-Fernandez, R. Kroeger, B. Lafferty, J. Agnew, Y. Lu, and K. O’Grady, “Texture Effects in IrMn/CoFe Exchange Bias Systems”, *IEEE Trans. Magn.* **44**, 2820 (2008).
- [74] S. van Dijken, J. Moritz, and J. M. D. Coey, “Correlation between perpendicular exchange bias and magnetic anisotropy in IrMn[Co/Pt]_n and [Pt/Co]_n/IrMn multilayers”, *J. Appl. Phys.* **97**, 063907 (2005).
- [75] Q. Ying and L. Yifan, “Tuning perpendicular exchange bias in IrMn/[Co/Pt] and IrMn/CoFe/Co/[Pt/Co] systems with ultra thin Pt layers”, *AIP Adv.* **8**, 025314 (2018).
- [76] E. H. Morales, Y. Wang, D. Lederman, A. J. Kellock, and M. J. Carey, “Interdiffusion and exchange bias in the Mn_xPt_{1-x}/Co system”, *J. Appl. Phys.* **93**, 4729 (2003).
- [77] K. Tsioplakis and Y. Gödecke, *Z. Metallkde.* **62**, 680 (1971).
- [78] J. Mathon, M. Villeret, and D. M. Edwards, “Exchange coupling in magnetic multilayers: effect of partial confinement of carriers”, *J. Phys. Cond. Matt.* **4**, 9873 (1992).
- [79] M. D. Stiles, “Exchange coupling in magnetic heterostructures”, *Phys. Rev. B* **48**, 7238 (1993).
- [80] P. Bruno, “Oscillations of Interlayer Exchange Coupling vs. Ferromagnetic Layers Thickness”, *Europhys. Lett.* **23**, 615 (1993).
- [81] P. Bruno, “Theory of interlayer magnetic coupling”, *Phys. Rev. B* **52**, 411 (1995).

- [82] L. Néel, “Magnetisme-sur un nouveau mode de couplage entre les animantations de deux couches minces ferromagnetiques”, *Cr. Hebd. Acad. Sci.* **255**, 1676 (1962).
- [83] J. Moritz, F. Garcia, J. C. Toussaint, B. Dieny, and J. P. Nozières, “Orange peel coupling in multilayers with perpendicular magnetic anisotropy: Application to (Co/Pt) -based exchange-biased spin-valves”, *Europhys. Lett.* **65**, 123 (2004).
- [84] A. Anguelouch, B. D. Schrag, G. Xiao, Y. Lu, P. L. Trouilloud, R. A. Wanner, W. J. Gallagher, and S. S. P. Parkin, “Two-dimensional magnetic switching of micron-size films in magnetic tunnel junctions”, *Appl. Phys. Lett.* **76**, 622 (2000).
- [85] G. Reiss and D. Meyners, “Logic based on magnetic tunnel junctions”, *J. Phys. Condens. Matter* **19**, 165220 (2007).
- [86] J. Slonczewski, “Current-driven excitation of magnetic multilayers”, *J. Magn. Magn. Mater.* **159**, L1 (1996).
- [87] Z. Diao, M. Pakala, A. Panchula, Y. Ding, D. Apalkov, L.-C. Wang, E. Chen, and Y. Huai, “Spin-transfer switching in MgO-based magnetic tunnel junctions (invited)”, *J. Appl. Phys.* **99**, 08G510 (2006).
- [88] S. Zhang, P. M. Levy, and A. Fert, “Mechanisms of Spin-Polarized Current-Driven Magnetization Switching”, *Phys. Rev. Lett.* **88**, 236601 (2002).
- [89] D. Ralph and M. Stiles, “Spin transfer torques”, *J. Magn. Magn. Mater.* **320**, 1190 (2008).
- [90] P. P. Freitas, R. Ferreira, S. Cardoso, and F. Cardoso, “Magnetoresistive sensors”, *J. Phys.: Condens. Matter* **19**, 165221 (2007).
- [91] W. Skowronski, P. Wisniowski, T. Stobiecki, S. Cardoso, P. P. Freitas, and S. van Dijken, “Magnetic field sensor with voltage-tunable sensing properties”, *Appl. Phys. Lett.* **101**, 192401 (2012).
- [92] B. Negulescu, D. Lacour, F. Montaigne, A. Gerken, J. Paul, V. Spetter, J. Marien, C. Duret, and M. Hehn, “Wide range and tunable linear magnetic tunnel junction sensor using two exchange pinned electrodes”, *Appl. Phys. Lett.* **95**, 112502 (2009).

- [93] J. Y. Chen, J. F. Feng, and J. M. D. Coey, "Tunable linear magnetoresistance in MgO magnetic tunnel junction sensors using two pinned CoFeB electrodes", *Appl. Phys. Lett.* **100**, 142407 (2012).
- [94] M. Nakayama, T. Kai, N. Shimomura, M. Amano, E. Kitagawa, T. Nagase, M. Yoshikawa, T. Kishi, S. Ikegawa, and H. Yoda, "Spin transfer switching in TbCoFe/CoFeB/MgO/CoFeB/TbCoFe magnetic tunnel junctions with perpendicular magnetic anisotropy", *J. Appl. Phys.* **103**, 07A710 (2008).
- [95] T. Devolder, P.-H. Ducrot, J.-P. Adam, I. Barisic, N. Vernier, J.-V. Kim, B. Ockert, and D. Ravelosona, "Damping of $\text{Co}_x\text{Fe}_{80-x}\text{B}_{20}$ ultrathin films with perpendicular magnetic anisotropy", *Appl. Phys. Lett.* **102**, 022407 (2013).
- [96] BESTEC, BERLIN.
- [97] W. C. Röntgen, *Ueber eine neue Art von Strahlen*, Sonderabdruck aus den Sitzungsberichten der Würzburger Physik.-medic. Gesellschaft 1895, Vorläufige Mittheilung (1896).
- [98] P. A. Varotsos and K. D. Alexopoulos, *Solid State Physics* (Savvala, Athens, Greece, 1995).
- [99] T. N. Blanton and C. R. Hoople, "X-ray diffraction analysis of ultrathin platinum silicide films deposited on (100) silicon", *Powder Diffr.* **17**, 7 (2002).
- [100] L. G. Parratt, "Surface Studies of Solids by Total Reflection of X-Rays", *Phys. Rev.* **95**, 359 (1954).
- [101] M. Tolan, *X-Ray Scattering from Soft-Matter Thin Films* (Springer-Verlag Berlin Heidelberg, 1999).
- [102] B. D. Culity and C. D. Graham, *Introduction to Magnetic Materials* (Wiley-Interscience, 2009).
- [103] K. J. LL.D., "XLIII. On rotation of the plane of polarization by reflection from the pole of a magnet", *Philos. Mag.* **3**, 321 (1877).
- [104] *Magneto-Optical Kerr Microscope and Magnetometer*, <http://www.evico-magnetics.de/microscope.html>, Accessed: 2018-11-11.

- [105] L. Mino, G. Agostini, E. Borfecchia, D. Gianolio, A. Piovano, E. Gallo, and C. Lamberti, “Low-dimensional systems investigated by x-ray absorption spectroscopy: a selection of 2D, 1D and 0D cases”, *J. Phys. D* **46**, 423001 (2013).
- [106] P. Palmberg and P. E. Industries, *Handbook of Auger Electron Spectroscopy: A Reference Book of Standard Data for Identification and Interpretation of Auger Electron Spectroscopy Data* (Physical Electronics Industries, 1972).
- [107] O. Manos, A. Böhnke, P. Bougiatioti, R. Klett, K. Rott, A. Niesen, J.-M. Schmalhorst, and G. Reiss, “Tunneling magnetoresistance of perpendicular CoFeB-based junctions with exchange bias”, *J. Appl. Phys.* **122**, 103904 (2017).
- [108] O. Manos, P. Bougiatioti, D. Dyck, T. Huebner, K. Rott, J.-M. Schmalhorst, and G. Reiss, “Correlation of tunnel magnetoresistance with the magnetic properties in perpendicular CoFeB-based junctions with exchange bias”, *J. Appl. Phys.* **125**, 023905 (2019).
- [109] J. Sinha, M. Gruber, M. Kodzuka, T. Ohkubo, S. Mitani, K. Hono, and M. Hayashi, “Influence of boron diffusion on the perpendicular magnetic anisotropy in ta|cofeb|mgo ultrathin films”, *J. Appl. Phys.* **117**, 043913 (2015).
- [110] T. Zhu, Y. Yang, R. C. Yu, H. Ambaye, V. Lauter, and J. Q. Xiao, “The study of perpendicular magnetic anisotropy in cofeb sandwiched by mgo and tantalum layers using polarized neutron reflectometry”, *Appl. Phys. Lett.* **100**, 202406 (2012).
- [111] N. Miyakawa, D. C. Worledge, and K. Kita, “Impact of ta diffusion on the perpendicular magnetic anisotropy of ta/cofeb/mgo”, *IEEE Magn. Lett.* **4**, 1000104 (2013).
- [112] S. Yuasa and D. D. Djayaprawira, “Giant tunnel magnetoresistance in magnetic tunnel junctions with a crystalline mgo(001) barrier”, *J. Phys. D* **40**, R337 (2007).
- [113] A. A. Greer, A. X. Gray, S. Kanai, A. M. Kaiser, S. Ueda, Y. Yamashita, C. Bordel, G. Palsson, N. Maejima, S.-H. Yang, G. Conti, K. Kobayashi, S. Ikeda, F. Matsukura, H. Ohno, C. M. Schneider, J. B. Kortright,

- F. Hellman, and C. S. Fadley, "Observation of boron diffusion in an annealed ta/cofeb/mgo magnetic tunnel junction with standing-wave hard x-ray photoemission", *Appl. Phys. Lett.* **101**, 202402 (2012).
- [114] T. Liu, Y. Zhang, J. W. Cai, and H. Y. Pan, "Thermally robust Mo/CoFeB/MgO trilayers with strong perpendicular magnetic anisotropy", *Sci. Rep.* **4**, 5895 (2014).
- [115] A. Niessen and F. D. Boer, "The enthalpy of formation of solid borides, carbides, nitrides, silicides and phosphides of transition and noble metals", *J. Less-Common Met.* **82**, 75 (1981).
- [116] D. R. Lide, *CRC Handbook of Chemistry and Physics 81st* (CRC press, 2000).
- [117] S. Cardoso, P. P. Freitas, Z. G. Zhang, P. Wei, N. Barradas, and J. C. Soares, "Electrode roughness and interfacial mixing effects on the tunnel junction thermal stability", *J. Appl. Phys.* **89**, 6650 (2001).
- [118] P. G. Gowtham, G. M. Stiehl, D. C. Ralph, and R. A. Buhrman, "Thickness-dependent magnetoelasticity and its effects on perpendicular magnetic anisotropy in Ta/CoFeB/MgO thin films", *Phys. Rev. B* **93**, 024404 (2016).
- [119] T. Liu, J. W. Cai, and L. Sun, "Large enhanced perpendicular magnetic anisotropy in CoFeB/MgO system with the typical Ta buffer replaced by an Hf layer", *AIP Adv.* **2**, 032151 (2012).
- [120] V. Sokalski, M. T. Moneck, E. Yang, and J.-G. Zhu, "Optimization of Ta thickness for perpendicular magnetic tunnel junction applications in the MgO-FeCoB-Ta system", *Appl. Phys. Lett.* **101**, 072411 (2012).
- [121] C. P. Bean and J. D. Livingston, "Superparamagnetism", *J. Appl. Phys.* **30**, S120 (1959).
- [122] J. Faure-Vincent, C. Tiusan, C. Bellouard, E. Popova, M. Hehn, F. Montaigne, and A. Schuhl, "Interlayer Magnetic Coupling Interactions of Two Ferromagnetic Layers by Spin Polarized Tunneling", *Phys. Rev. Lett.* **89**, 107206 (2002).
- [123] L. E. Nistor, "PhD thesis", Université de Grenoble (2011).

- [124] M. Yamanouchi, R. Koizumi, S. Ikeda, H. Sato, K. Mizunuma, K. Miura, H. D. Gan, F. Matsukura, and H. Ohno, "Dependence of magnetic anisotropy on MgO thickness and buffer layer in $\text{Co}_{20}\text{Fe}_{60}\text{B}_{20}$ -MgO structure", *J. Appl. Phys.* **109**, 07C712 (2011).
- [125] D. C. Worledge, G. Hu, D. W. Abraham, J. Z. Sun, P. L. Trouilloud, J. Nowak, S. Brown, M. C. Gaidis, E. J. O'Sullivan, and R. P. Rober-tazzi, "Spin torque switching of perpendicular Ta/CoFeB/MgO-based magnetic tunnel junction", *Appl. Phys. Lett.* **98**, 022501 (2011).
- [126] J. Hayakawa, S. Ikeda, Y. M. Lee, F. Matsukura, and H. Ohno, "Effect of high annealing temperature on giant tunnel magnetoresistance ratio of CoFeB/MgO/CoFeB magnetic tunnel junctions", *Appl. Phys. Lett.* **89**, 232510 (2006).
- [127] K. Yakushiji, H. Kubota, A. Fukushima, and S. Yuasa, "Perpendicular magnetic tunnel junctions with strong antiferromagnetic interlayer exchange coupling at first oscillation peak", *Appl. Phys. Lett.* **8**, 083003 (2015).
- [128] A. Kaidatzis, C. Bran, V. Psycharis, M. Vázquez, J. M. García-Martín, and D. Niarchos, "Tailoring the magnetic anisotropy of CoFeB/MgO stacks onto W with a Ta buffer layer", *Appl. Phys. Lett.* **106**, 262401 (2015).
- [129] S. Y. Jang, C.-Y. You, S. H. Lim, and S. R. Lee, "Annealing effects on the magnetic dead layer and saturation magnetization in unit structures relevant to a synthetic ferrimagnetic free structure", *J. Appl. Phys.* **109**, 013901 (2011).
- [130] A. A. Khan, J. Schmalhorst, G. Reiss, G. Eilers, M. Münzenberg, H. Schuhmann, and M. Seibt, "Elastic and inelastic conductance in Co-Fe-B/MgO/Co-Fe-B magnetic tunnel junctions", *Phys. Rev. B* **82**, 064416 (2010).
- [131] H. Almasi, C. L. Sun, X. Li, T. Newhouse-Illige, C. Bi, K. C. Price, S. Nahar, C. Grezes, Q. Hu, P. Khalili Amiri, K. L. Wang, P. M. Voyles, and W. G. Wang, "Perpendicular magnetic tunnel junction with W seed and capping layers", *J. Appl. Phys.* **121**, 153902 (2017).

- [132] H. D. Gan, H. Sato, M. Yamanouchi, S. Ikeda, K. Miura, R. Koizumi, F. Matsukura, and H. Ohno, "Origin of the collapse of tunnel magnetoresistance at high annealing temperature in CoFeB/MgO perpendicular magnetic tunnel junctions", *Appl. Phys. Lett.* **99**, 252507 (2011).
- [133] C.-Y. Yang, S.-J. Chang, M.-H. Lee, K.-H. Shen, S.-Y. Yang, H.-J. Lin, and Y.-C. Tseng, "Competing Anisotropy-Tunneling Correlation of the CoFeB/MgO Perpendicular Magnetic Tunnel Junction: An Electronic Approach", *Sci. Rep.* **5**, 17169 (2015).
- [134] C. C. Tsai, C.-W. Cheng, Y.-C. Weng, and G. Chern, "The dipolar interaction in CoFeB/MgO/CoFeB perpendicular magnetic tunnel junction", *J. Appl. Phys.* **115**, 17C720 (2014).
- [135] W. C. Nunes, W. S. D. Folly, J. P. Sinnecker, and M. A. Novak, "Temperature dependence of the coercive field in single-domain particle systems", *Phys. Rev. B* **70**, 014419 (2004).
- [136] J. G. Alzate, P. K. Amiri, P. Upadhyaya, S. S. Cherepov, J. Zhu, M. Lewis, R. Dorrance, J. A. Katine, J. Langer, K. Galatsis, D. Markovic, I. Krivorotov, and K. L. Wang, "Voltage-induced switching of nanoscale magnetic tunnel junctions", in *Iedm*, Vol. San Francisco, CA, USA (2012), pp. 29.5.1–29.5.4.
- [137] J. Deng, G. Liang, and G. Gupta, "Ultrafast and low-energy switching in voltage-controlled elliptical pMTJ", *Sci. Rep.* **7**, 16562 (2017).
- [138] K. H. He, J. S. Chen, and Y. P. Feng, "First principles study of the electric field effect on magnetization and magnetic anisotropy of FeCo/MgO(001) thin film", *Appl. Phys. Lett.* **99**, 072503 (2011).
- [139] J. Zhang, P. V. Lukashev, S. S. Jaswal, and E. Y. Tsymlal, "Model of orbital populations for voltage-controlled magnetic anisotropy in transition-metal thin films", *Phys. Rev. B* **96**, 014435 (2017).
- [140] W.-G. Wang, M. Li, S. Hageman, and C. L. Chien, "Electric-field-assisted switching in magnetic tunnel junctions", *Nat. Mater.* **11**, 64 (2011).
- [141] A. T. Hindmarch, V. Harnchana, A. S. Walton, A. P. Brown, R. M. D. Brydson, and C. H. Marrows, "Zirconium as a Boron Sink in Crystalline CoFeB/MgO/CoFeB Magnetic Tunnel Junctions", *Appl. Phys. Express* **4**, 013002 (2011).

- [142] M. Meinert, B. Büker, D. Graulich, and M. Dunz, “Large exchange bias in polycrystalline MnN/CoFe bilayers at room temperature”, *Phys. Rev. B* **92**, 144408 (2015).
- [143] M. Dunz, J. Schmalhorst, and M. Meinert, “Enhanced exchange bias in MnN/CoFe bilayers after high-temperature annealing”, *AIP Adv.* **8**, 056304 (2018).
- [144] I. L. Prejbeanu, M. Kerekes, R. C. Sousa, H. Sibuet, O. Redon, B. Dieny, and J. P. Nozières, “Thermally assisted MRAM”, *J. Phys. Condens. Matter* **19**, 165218 (2007).
- [145] I. L. Prejbeanu, W. Kula, K. Ounadjela, R. C. Sousa, O. Redon, B. Dieny, and J. P. Nozières, “Thermally assisted switching in exchange-biased storage layer magnetic tunnel junctions”, *IEEE Trans. Magn.* **40**, 2625 (2004).

Publications

1. **Orestis Manos**, Panagiota Bougiatioti, Denis Dyck, Torsten Hübner, Jan-Michael Schmalhorst and Günter Reiss, “Correlation of tunnel magnetoresistance with the magnetic properties in perpendicular CoFeB-based junctions with exchange bias”, *J. Appl. Phys.*, **125**, 023905 (2019)
2. Panagiota Bougiatioti, **Orestis Manos**, Olga Kuschel, Joachim Wollschläger, Martin Tolkiehn, Sonia Francoual and Timo Kuschel, “Impact of magnetic moment and anisotropy of $\text{Co}_{1-x}\text{Fe}_x$ thin films on the magnetic proximity effect of Pt”, *Phys. Rev. Lett.*, under review, arXiv:1807.09032, (2018)
3. Panagiota Bougiatioti, Christoph Klewe, Daniel Meier, **Orestis Manos**, Olga Kuschel, Joachim Wollschläger, Laurence Bouchenoire, Simon D. Brown, Jan-Michael Schmalhorst, Günter Reiss and Timo Kuschel, “Quantitative Disentanglement of the Spin Seebeck, Proximity-Induced, and Ferromagnetic-Induced Anomalous Nernst Effect in Normal-Metal-Ferromagnet Bilayers”, *Phys. Rev. Lett.*, **119**, 227205, (2017)
4. Panagiota Bougiatioti, **Orestis Manos**, Christoph Klewe, Daniel Meier, Niclas Teichert Jan-Michael Schmalhorst, Timo Kuschel and Günter Reiss, “Electrical transport and optical band gap of NiFe_2O_x thin films”, *J. Appl. Phys.*, **122**, 225101, (2017)

5. **Orestis Manos**, Alexander Böhnke, Panagiota Bougiatioti, Robin Klett, Karsten Rott, Alessia Niesen, Jan-Michael Schmalhorst and Günter Reiss, “Tunneling magnetoresistance of perpendicular CoFeB-based junctions with exchange bias”, *J. Appl. Phys.*, **122**, 103904, (2017)

Conferences

- 03/2017 Talk at the **81st Deutsche Physikalische Gesellschaft Frühjahrstagung**, Dresden, Germany
- 02/2017 Poster at the **Spinmechanics 4**, Lake Louise, Canada
- 03/2016 Poster at the **80th Deutsche Physikalische Gesellschaft Frühjahrstagung**, Regensburg, Germany
- 03/2015 Poster at the **79th Deutsche Physikalische Gesellschaft Frühjahrstagung**, Berlin, Germany

Acknowledgements

In the final sentences of this thesis, I would like to express my sincere gratitude to everyone who contributed to successfully complete this Ph.D. work.

First, I wish to express my gratefulness to my doctoral supervisor, Prof. Dr. Günter Reiss, for being a great mentor and providing me with numerous fruitful ideas. The scientific discussions, advises and his support in any step of my research was always an invaluable source of inspiration.

I would also like to thank my direct supervisor, Dr. Jan Schmalhorst, who contributed significantly to the success of this work via his direct response to my questions and queries, as well as his scientific advises during my studies.

I am also grateful to Dr. Karsten Rott for his tireless assistance to any technical problem that I was confronted with during the experiments as well as for the preparation of high-quality spintronic devices which was one of the pillars of these investigations. In addition, I would like to thank Aggi Windmann for her professionalism to help me at any time with the administrative issues.

I would be remiss not to acknowledge Prof. Dr. Andreas Hütten, Dr. Panagiota Bougiatioti, Dr. Torsten Hübner, Dr. Alexander Böhnke, Dr. Alessia Niesen, Dr. Robin Klett, Dr. Manuel Glas, Dr. Niclas Teichert, Robin Silber, Anastasiia Moskaltsova, Niklas Dohmeier, Dr. Christoph Klewe and Dr. Timo Kuschel for their direct and indirect contribution to the fulfillment of this work. In addition, I wish to thank the rest members of D2 for the very pleasant and joyful working collaboration.

I am greatly indebted to the Deutsche Forschungsgemeinschaft (DFG) and the HARFIR Research & innovation project funded by the European Commission under the 7th Framework Programme, for the financial support. In

addition, many thanks go to all the members of my dissertation committee for rating my work and attending my defence.

There are not enough words for me to express my appreciation to Prof. Dr. Georgios Gatzounis and Prof. Dr. Ioannis Tsolakis from the General University Hospital of Patras for their dedication to the special mission of a doctor and for being there in my time of need. I will never forget you.

Finally, I would like to offer my special thanks to my friends and family for the moral support throughout this wonderful experience. Thank you all.